MASTER'S THESIS

CPFD simulation in Barracuda VR® of a novel dual fluidized bed cold flow model

ausgeführt zum Zwecke der Erlangung des akademischen Grades eines

Diplom Ingenieurs

unter der Leitung von

Univ. Prof. Dipl.-Ing. Dr. techn. Hermann Hofbauer

E166 – Institut für Verfahrenstechnik,

Umwelttechnik und Technische Biowissenschaften

unter der Betreuung von:

Dipl.-Ing. Dipl.-Ing. Dr.techn. Stephan Kraft

eingereicht an der Technischen Universität Wien,

Fakultät für Maschinenwesen und Betriebswissenschaften

von

Andreas Lunzer

Matrikelnummer 01325351

Neulerchenfelder Straße 13/5

1160 Wien

Wien, Day. Oktober 2018   Andreas Lunzer

Affidavit

I declare in lieu of oath that I wrote this thesis and performed the associated research myself, using only literature cited in this volume.

<div style="text-align: right">

_____

Signature

</div>

Danksagung

An dieser Stelle möchte ich meinen beiden Diplomarbeitsbetreuern danken. Prof. Hermann Hofbauer hat mich bereits vor seiner ersten Vorlesung für die TU Wien begeistert, in jeder folgenden das Interesse in die Verfahrenstechnik verstärkt und mir ermöglicht unter anderem diese Diplomarbeit zu schreiben.

Stephan Kraft hat mich vom ersten bis zum letzten Tag in dieser Arbeit unterstützt und motiviert. Seine lebensfrohe Art hat auch bei Rückschlägen stets abgefärbt und zum Weitermachen animiert. Die Freiluftmeetings werde ich nie vergessen.

Großer Dank gebührt vor allem meiner Freundin Stephanie, die mir eine große Stütze ist, mich bei jedem Schritt ermutigt und immer wieder aufgefangen hat.

Meiner Familie danke ich, dass sie die Weichen gestellt haben; meinem Bruder, der mir früh Rechnen beibrachte, meiner Schwester, die mich für eine HTL begeisterte und meinen Eltern, die mir immer ermöglicht haben meine Träume zu verfolgen.

Zu guter Letzt danke ich meinen Studienkollegen, die den Weg mit mir gegangen sind und mit denen ich Höhen und Tiefen teilen konnte, insbesondere Nina Wolf, die als Sitznachbarin in der Schule und im Studium immer ein offenes Ohr für mich hatte.

Dem Ingeniör ist nichts zu schwör

Dipl.-Ing. D. Düsentrieb

source:pixabay.com

Abstract

The target of this master's thesis is to simulate a cold flow model of a novel biomass gasification plant. The fluid dynamical behavior depends heavily on the fluid's and particle's properties and in real reactors a particle size distribution (PSD) is present. An Eulerian-Eulerian approach is only capable to simulate large applications at the expense of high computational costs if the actual PSD is considered. An Eulerian-Lagrangian approach is capable of simulating a PSD and in particular the multi-phase particle in cell (MP-PIC) method is designed for simulations with a high number of particles. Therefore, Barracuda VR®, a software-tool with an implemented MP-PIC method specifically designed for CPFD (computational particle fluid dynamics) simulations, was the software of choice.

The discussed cold flow model in this thesis is located at TU Wien and several experiments have already been conducted. Those experiments were used to verify the simulation results. The solid used is composed of bronze particles with a Sauter diameter of $81.7 \mu m$ and a given PSD.

The simulations and adjustments were rated on the one hand qualitatively by visual observation of the particle volume fraction and distribution of the particles in the reactor and on the other hand quantified by comparing the measured and simulated data of the particle circulation rate and the pressure at designated locations.

The simulations were conducted using different drag laws since they have a great influence on the simulation results. An energy-minimization multi-scale (EMMS) approach, a blended Wen-Yu and Ergun (WYE) drag law, and a drag law of Ganser were used. Furthermore, a focus was set onto the normal particle stress, which plays a significant role in close-packed regions. The constant P_S to calculate the particle stress was modified, leading to a higher normal stress near close-pack and subsequently reducing the particle volume fraction. Another aspect was raising the fluidization rate in the loop seals to increase the particle circulation rate, since it was underestimated depending on the settings (e.g. P_S constant).

By optimizing the settings, the simulation became stable and flooding behavior, experienced at the start, did not occur anymore. The Ganser drag law was found to be

the best suited drag law for the simulation. The WYE drag law overpredicted the mass flow leading to an unstable system and the EMMS's predicted particle flow rate was unrealistically small while calculating partly good fits for the pressure profile in the fuel reactor's column. The Ganser drag law combined with an adjusted P_S value with ($P_S = 30Pa$) or without ($P_S = 50Pa$) increased loop seal fluidization rates was providing the best performance.

Contents

1 Introduction

CFD simulation is a diverse tool for a broad spectrum in research and industrial applications. It is used in fields like aerospace and chemical engineering and even implemented in other areas e.g. civil and biomedical engineering [1]. The application of CFD in gas-solid multi-phase systems does face new challenges compared to traditional simulations solely focusing on fluids. The introduction of CFD into the field of fluidized beds made the development of new models and approaches essential. In this thesis the simulation of a cold flow model used for the up-scaling and dimensioning of a biomass gasification plant is the object of interest.

Cold flow models are an important tool for scaling up small plants and studying their fluid dynamical behavior. A $100kW$ biomass gasification plant with a dual fluidized bed at TU Wien [2], a pilot plant for further projects, was designed with the help of the mentioned cold flow model. The goal of this thesis is to create a working model in Barracuda which predicts the behavior of a real cold flow model as accurate as possible and gain a deeper understanding of simulations with fluidized beds.

Cold flow models offer the possibility to optimize and test the design of a plant on a small scale and CFD simulations can reflect trends and predict the process in a plant with a certain degree of accuracy.

CFD methods can help to investigate and therefore optimize fluidized bed processes.

A CFD model with optimized settings leads to better predicted results and can be verified with a real cold flow model. Subsequently the verified model allows fast testing of different modifications of the cold flow model itself.

The testing of different set-ups without the need of an actual physical modification accelerates the planning phase, while saving time and money. Instead of elaborated manufacturing only adjustments on a CAD model are necessary and the simulation results will be, depending on the complexity, available in a few days or even hours.

Furthermore, a computational simulation allows deeper insight into the plant itself and is not limited by sight or measuring points. Therefore, fluid dynamical behavior can be investigated at any desired location.

1.1 Approach in this work

In the first step the CAD model of the cold flow model will be created based on technical drawings and if necessary simplified or altered if applicable. The simulation of a dual fluidized bed with a variety of different properties (e.g. velocity and particle volume fraction) in the system itself will be approached by adjusting and testing different settings (e.g. drag law and particle normal stress parameters) with information of a literature review.

The scope of this thesis covers following research questions:

How do the different settings in the CPFD software influence the particle behavior?
What measures lead to the best performance compared to the real cold flow model at a specific operating point?
Do the optimal settings predict reliable results at different operating points in the same system?

As a first step the target is to simulate only a distinct operating point of the real model for validation. The performance of the system will be rated qualitatively by visual observation and quantitatively by defining mass flow and pressure parameters but also by comparing the resulting graphs. New information gathered in new simulations will be used to improve the model of the simulation even further. After finding the optimal settings the model is applied to different operating points and compared to the real cold flow model again.

2 Theory

2.1 Fundamentals of fluidization

2.1.1 Characterization of particles

Particles can be defined by certain properties which will be used for characterization and calculation in this work. The essential settings for the simulation will be explained briefly.

2.1.1.1 Particle density

The particle density, ρ_p, is the mass, m_p, per volume, V_p, of a single particle and in this thesis, it is assumed to be the same as the density of its material.

$$\rho_p = \frac{m_p}{V_p} \tag{2.1}$$

2.1.1.2 Particle size distribution

If the particles have different sizes, those are described by the particle size distribution (PSD). The PSD used in this thesis in pictured in Figure 3.5.

2.1.1.3 Particle diameter

In this thesis the Sauter diameter, d_{sv}, was used. The Sauter diameter is the diameter, assuming identical spheres, adding up to the actual total volume ($\sum V_p$) and surface area ($\sum A_p$).

$$d_{sv} = 6 * \frac{\sum V_p}{\sum A_p} \tag{2.2}$$

The Sauter diameter can also be described as the area weighted mean size [3] and can be calculated from the volume specific surface area, S_V, of the particles.

$$S_V = \frac{\sum A_p}{\sum V_p} \tag{2.3}$$

Assuming particles with spheres of the same size and diameter d_{sv}, Eq. 2.3 simplifies to Eq. 2.4 and is described as the ratio of the surface area of the particle to its volume.

$$S_V = \frac{A_p}{V_p} = \frac{d_{sv}^2 * \pi}{\frac{d_{sv}^3}{6} * \pi} = \frac{6}{d_{sv}} \tag{2.4}$$

S_V can be determined out of the measured particle size distribution using the "-1st" momentum, $M_{-1,3}$, from the volume distribution density $q_3(x_p)$ [3].

$$M_{-1,3} = \int_{x_{p,min}}^{x_{p,max}} x_p^{-1} q_3(x_p) \, dx_p = \sum_{i=1}^{m} \frac{1}{\bar{x}_{p,i}} \bar{q}_{3,i} \Delta x_{p,i} \tag{2.5}$$

where:

$$\bar{q}_{3,i} = \frac{\Delta Q_{3,i}}{x_{p,i} - x_{p,i-1}}$$

$$\bar{x}_{p,i} = \frac{x_{p,i} + x_{p,i-1}}{2}$$

$$Q_3(x_{p,i}) = \int_{x_{p,min}}^{x_{p,i}} q_3(x_p) \, dx_p$$

$$S_V = 6 * M_{-1,3} \tag{2.6}$$

$$d_{sv} = \frac{6}{S_V} = \frac{1}{M_{-1,3}} \tag{2.7}$$

x_p = particle size

2.1.1.4 Sphericity

The sphericity, ϕ_p, of a particle is defined by the ratio of a sphere's surface and the surface of the particle itself [4].

$$\phi_p = \left(\frac{\text{surface of sphere}}{\text{surface of particle}} \right)_{\text{of same volume}} \tag{2.8}$$

If the particles are perfect spheres, as assumed in this thesis, the ϕ_p equals to 1.

2.1.1.5 Bulk density and volume fraction

For particles in bulk also the bulk density (ρ_{bulk}), the density of the gas and particle mixture, and porosity are important. The porosity is the volume fraction of the fluid phase. The volume fraction of the fluid or particle phase is described by the ratio of fluid volume (V_f) or particle volume (V_p) of the total volume ($V_f + V_p$) (see Eq. 2.9).

$$\varepsilon_p = \frac{V_p}{V_p + V_f} \quad \text{and} \quad \varepsilon_f = \frac{V_f}{V_p + V_f} \tag{2.9}$$

The bulk density, ρ_{bulk}, is important to determine the close-pack particle volume fraction, ε_{cp}.

$$\varepsilon_{cp} = \frac{\rho_{bulk}}{\rho_p} \tag{2.10}$$

2.1.2 Drag law

The drag laws in Barracuda are calculating a force, the drag force $\boldsymbol{F}_d$ depending on a drag function D, acting on the particles and is calculated by Eq. 2.11 [5].

$$\boldsymbol{F}_d = m_p * D * (\boldsymbol{u}_f - \boldsymbol{u}_p) \tag{2.11}$$

The WYE's (in the Wen-Yu regime) and Ganser's drag function is related to the drag coefficient C_d as in Eq. 2.12 while the EMMS's and WYE's (in the Ergun regime) drag function is calculated differently as described by Eq. 2.14 and Eq. 2.27. The drag functions of the respective drag laws are defined in the following sections.

$$D = \frac{3}{8} * C_d * \frac{\rho_f * |\boldsymbol{u}_f - \boldsymbol{u}_p|}{\rho_p * r_p} \tag{2.12}$$

$\boldsymbol{u}_f$ = fluid velocity
$\boldsymbol{u}_p$ = particle velocity

2.1.2.1 EMMS

This drag law is based on an energy-minimization multi-scale approach (EMMS) and will be subsequently abbreviated with "EMMS". The drag coefficient is calculated from structure parameters of the gas solid interactions. For further information and details the reader is referred to Yang et al. [6].

$$\boldsymbol{F}_d = m_p * D * (\boldsymbol{u}_f - \boldsymbol{u}_p) \tag{2.13}$$

$$D = \frac{9}{2} \frac{\mu_f}{\rho_p r_p^2} f_e \tag{2.14}$$

$$f_e = \begin{cases} \frac{1}{18\varepsilon_f}\left(c_0\frac{\varepsilon_p}{\varepsilon_f} + c_1 Re\right) & \varepsilon_f < 0.74 \\ (c_2 + c_3 Re^{n_0})\,\omega & \varepsilon_f \geq 0.74 \text{ and } Re < 1000 \\ c_4 \frac{Re}{24}\omega & \varepsilon_f \geq 0.74 \text{ and } Re \geq 1000 \end{cases} \tag{2.15}$$

$$\omega = \begin{cases} c_5 + \frac{c_6}{4(\varepsilon_f+c_7)^2+c_8} & 0.74 \leq \varepsilon_f < 0.82 \\ c_9 + \frac{c_{10}}{4(\varepsilon_f+c_{11})^2+c_{12}} & 0.82 < \varepsilon_f \leq 0.97 \\ c_{13} + c_{14}\varepsilon_f & 0.97 < \varepsilon_f \leq 1 \end{cases} \tag{2.16}$$

where:

$c_0 = 150$	$c_1 = 1.75$	$c_2 = 1.0$	$c_3 = 0.15$	$c_4 = 0.44$
$c_5 = -0.576$	$c_6 = 0.0214$	$c_7 = 0.7463$	$c_8 = 0.0044$	$c_9 = -0.0101$
$c_{10} = 0.0038$	$c_{11} = 0.7789$	$c_{12} = 0.0040$	$c_{13} = -31.8295$	$c_{14} = 32.8295$
$n_0 = 0.687$				

2.1.2.2 Ganser

The implemented drag law for "Non-spherical Ganser", subsequently called "Ganser" is already implemented in the software and the governing equations are listed below as described by the Barracuda user manual [5]. The drag law is based on studies of Chhabra et al. [7] and Wen and Yu [8]. The sphericity of the particles in this work is $\phi_p = 1$.

$$\boldsymbol{F}_d = m_p * D * (\boldsymbol{u}_f - \boldsymbol{u}_p) \tag{2.17}$$

$$D = \frac{3}{8} * C_d * \frac{\rho_f * |\boldsymbol{u}_f - \boldsymbol{u}_p|}{\rho_p * r_p} \tag{2.18}$$

$$C_d = \varepsilon_f^{n_0} * K_2 * \left[\frac{24}{ReK_1K_2}(1 + c_0(ReK_1K_2)^{n_1}) + \frac{24c_1}{1 + \frac{c_2}{ReK_1K_2}} \right] \tag{2.19}$$

$$K_1 = \frac{3}{1 + 2\phi_p^{-0.5}} \tag{2.20}$$

$$K_2 = 10^{n_2(-\log \phi_p)^{n_3}} \tag{2.21}$$

$K_1 = 1$ and $K_2 = 1$ with $\phi_p = 1$ and the equations is simplified.

$$C_d = \varepsilon_f^{n_0} * \left[\frac{24}{Re}(1 + c_0 * Re^{n_1}) + \frac{24c_1}{1 + \frac{c_2}{Re}} \right] = \frac{24}{Re} * \varepsilon_f^{n_0} * \left((1 + c_0 * Re^{n_1}) + \frac{c_1}{Re + c_2} \right) \tag{2.22}$$

where:

$c_0 = 0.1118$	$c_1 = 0.01794$	$c_2 = 3305$	$n_0 = -2.65$
$n_1 = 0.6567$	$n_2 = 1.8148$	$n_3 = 0.5743$	

2.1.2.3 WYE

The Wen-Yu correlation is appropriate for more dilute systems, the Ergun relationship is appropriate at higher packing fractions, and a drag function blending both is already implemented in Barracuda [5] as Wen-Yu and Ergun (WYE) drag function.

$$\boldsymbol{F}_d = m_p * D * (\boldsymbol{u}_f - \boldsymbol{u}_p) \tag{2.23}$$

$$D = \begin{cases} D_1 & \varepsilon_p < 0.75\,\varepsilon_{cp} \\ (D_2 - D_1)\left(\frac{\varepsilon_p - 0.75\,\varepsilon_{cp}}{0.85\,\varepsilon_{cp} - 0.75\,\varepsilon_{cp}}\right) + D_1 & 0.75\,\varepsilon_{cp} \ge \varepsilon_p \ge 0.85\,\varepsilon_{cp} \\ D_2 & \varepsilon_p > 0.85\,\varepsilon_{cp} \end{cases} \tag{2.24}$$

D_1 is the Wen and Yu drag function defined as

$$D_1 = \frac{3}{8} C_d \frac{\rho_f |\boldsymbol{u}_f - \boldsymbol{u}_p|}{\rho_p r_p} \tag{2.25}$$

The drag coefficient C_d is the Wen and Yu drag coefficient.

$$C_d = \begin{cases} \frac{24}{Re} * \varepsilon_f^{n_0} & Re < 0.5 \\ \frac{24}{Re} * \varepsilon_f^{n_0} * (c_0 + c_1 * Re^{n_1}) & 0.5 \le Re \le 1000 \\ c_2 * \varepsilon_f^{n_0} & Re > 1000 \end{cases} \tag{2.26}$$

where:

$c_0 = 1 \qquad c_1 = 0.15 \qquad c_2 = 0.44 \qquad n_0 = -2.65 \qquad n_1 = 0.687$

D_2 is the Ergun drag function defined as

$$D_2 = 0.5\left(\frac{c_1 \varepsilon_p}{\varepsilon_f Re} + c_0\right) \frac{\rho_f |\boldsymbol{u}_f - \boldsymbol{u}_p|}{\rho_p r_p} \tag{2.27}$$

where:

$c_0 = 2 \qquad\qquad c_1 = 180$

2.1.3 States of fluidization

Particles in bulk in a column will form a fixed bed if no fluid flow through the column is present. Introducing a fluid flow at the bottom of the column will force the fluid to travel upwards through the packed bed's voids. The fluid-solid interaction will cause a pressure drop over the fixed bed and eventually the fixed bed expands. The pressure drop over the fixed bed will increase with increasing superficial velocity, u_0, of the fluid. By increasing u_0 further the particles will start to move at some point. This state is the beginning of fluidization, referred as minimum fluidization (Figure 2.1b) which occurs at minimum fluidization velocity u_{mf}. At this point the pressure drop over the bed will remain constant with increased u_0. With higher fluid flow rates the movement of the particles becomes more vigorous and gas bubbles will form and rise as the bed becomes a bubbling bed (Figure 2.1c). Once the terminal velocity of the particles is exceeded, the upper surface of the bed will disappear and particles are entrained, and turbulent fluidization occurs. At this state turbulent motions of solid clusters and voids of gas can be observed (Figure 2.1d) and an increased pressure drop over the bed with increasing u_0 can be detected again. Increasing the gas flow even more will lead to a very diluted system of solids being carried out of the bed by pneumatic transport (Figure 2.1e). For steady state behaviour in a turbulent or pneumatic transport regime, recirculation of the particles is necessary [4].
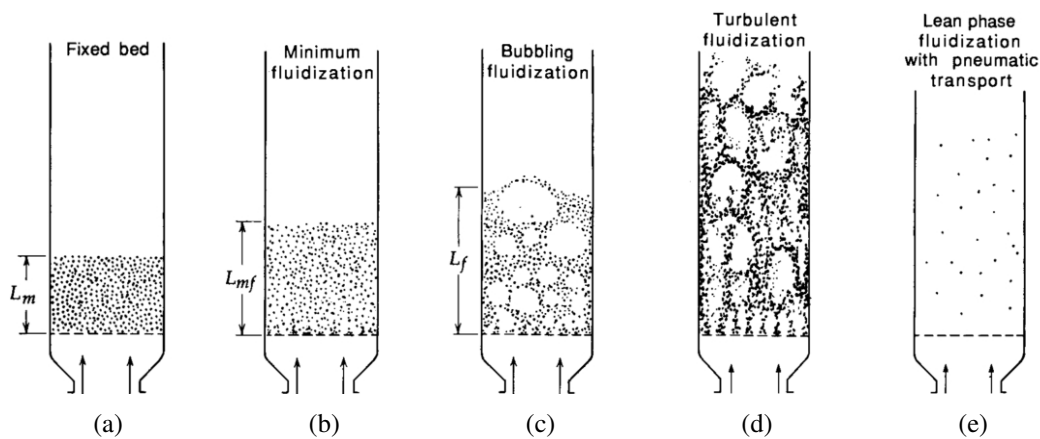

Figure 2.1: States of fluidization - overview [4]

2.1.3.1 Pressure Drop over Fluidization

The transition of a fixed to fluidized bed and to pneumatic conveying can also be observed in the pressure drop over the fluidized bed. With increasing superficial velocity,

the pressure drop over a fixed bed increases until the minimum fluidization velocity is reached. At this point the pressure drop remains constant and equals the pressure drop due to the weight of the particles in the fluidized bed. Once the terminal velocity, u_t, is exceeded, the particles will be carried out of the column by the fluid.
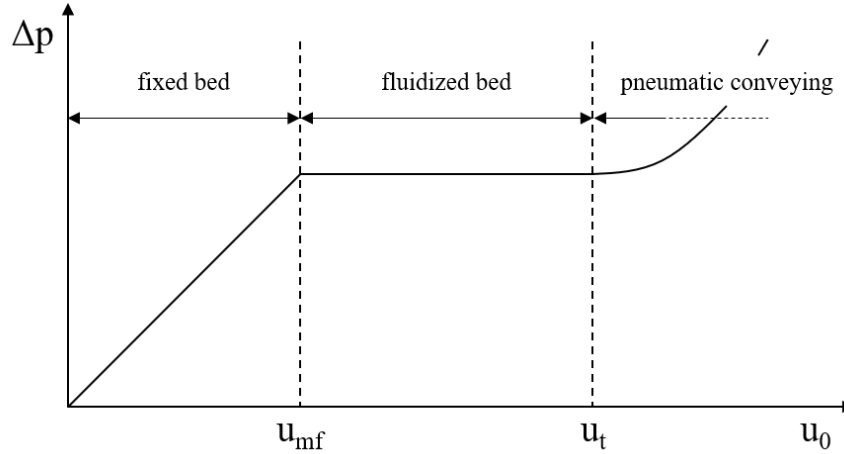

Figure 2.2: Pressure profile over superficial velocity for fluidization regimes

2.1.3.2 Minimum fluidization velocity

The minimum fluidization velocity, u_{mf}, indicates the transition of a fixed bed to a fluidized bed. The u_{mf} can be calculated by combining Ergun's equation to calculate the pressure drop over a fixed bed [9], which equals at u_{mf} the pressure drop over a fluidized bed, the pressure drop due to the particles being lifted by the fluid. By rearranging and making the terms dimensionless Eq. 2.28 can be obtained [10]. Different authors, e.g. Wen and Yu [10] or Grace [11], proposed different values for the constants C_1 and C_2.

Inserting Grace's proposed constants Eq. 2.29 can be obtained and rearranging leads to Eq. 2.30 to calculate u_{mf} [11].

$$Re_{p,mf} = \sqrt{C_1^2 + C_2 Ar} - C_1 \tag{2.28}$$

$$Re_{p,mf} = \sqrt{27.2^2 + 0.0408 Ar} - 27.2 \tag{2.29}$$

$$u_{mf} = \frac{\mu_f}{d_{sv} * \rho_f} * \left(\sqrt{27.2^2 + 0.0408 Ar} - 27.2 \right) \tag{2.30}$$

2.1.3.3 Drag force

A particle moving through a fluid experiences a force, the drag force, depending on the realtive velocity between the particle and fluid, opposite to the direction of movement, due to shear forces acting on the particle's surface. The drag force, $\boldsymbol{F}_d$, for a single spherical particle is expressed in Eq. 2.31 [12]. The area A_p is the cross-sectional area of the particle and for a spherical particle the area of a circle with the same diameter.

$$\boldsymbol{F}_d = \frac{\rho_f * (\boldsymbol{u}_f - \boldsymbol{u}_p) * |\boldsymbol{u}_f - \boldsymbol{u}_p|}{2} * A_p * C_d(Re_p) \tag{2.31}$$

The drag coefficient C_d is a function of Re_p and can be determined over its Reynolds number experimentally. The correlation of C_d and Re_p is depicted in Figure 2.3. The correlation can be split roughly into three categories: the Stokes regime, where the viscous forces are dominant, the transition region, where the influence of inertial forces increases, and the Newton regime, where the inertial forces dominate and the drag coefficient is almost constant. At $Re_{p,crit}$ a drastic decrease of C_d occurs due to the transition of a laminar to a turbulent boundary layer on the particles surface and a resulting smaller trail area [13].
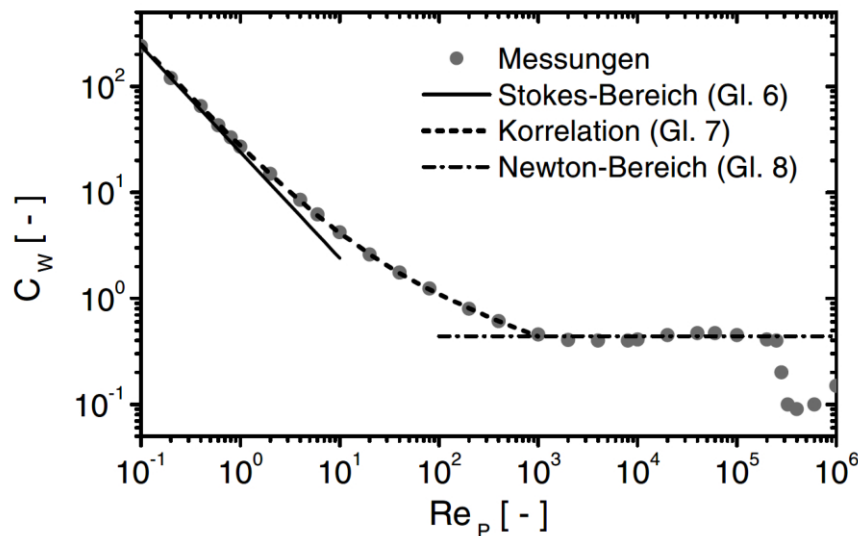

Figure 2.3: C_d-Re_p diagram [13]

Table 2.1: C_d-Re_p correlation - overview [13]

	Formula	Limits
Stokes	$C_d = \frac{24}{Re_p}$	$Re_p < 0.5$
Transition	$C_d = \frac{24}{Re_p} * \left(1 + 0.15 * Re_p^{0.687}\right)$	$0.5 < Re_p < 1000$
Newton	$C_d \approx 0.44$	$1000 < Re_p < Re_{p,crit}$

where:

$$Re_{p,crit} = \text{critical Reynolds number} \approx 2.5 * 10^5$$

2.1.3.4 Terminal velocity

The terminal velocity, u_t, is the stationary velocity of a single spherical particle in a stationary fluid when the forces acting on the particle are in equilibrium. At this point the forces acting on the particle from fluid, drag $\boldsymbol{F}_d$ and buoyancy $\boldsymbol{F}_b$, equal the gravity force $\boldsymbol{F}_g$ [12]. Therefore, if a fluid flows towards a stationary spherical particle from below with terminal velocity the particle will stay at the same spot. If the fluid velocity will be further increased the particle will start moving in the fluid's direction.
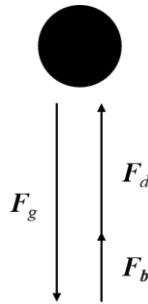

Figure 2.4: Forces acting on spherical particle in fluid with terminal velocity

The forces acting on the particle in equilibrium:

$$\boldsymbol{F}_g = \boldsymbol{F}_d + \boldsymbol{F}_b \tag{2.32}$$

Expressing and rearranging the terms for the forces leads to Eq. 2.33.

$$(\rho_p - \rho_f) * \frac{d_{sv}^3 * \pi}{6} * g = \frac{\rho_f * u_t^2}{2} * \frac{d_{sv}^2 * \pi}{4} * C_d(Re_p) \tag{2.33}$$

Therefore, the terminal velocity is given by Eq. 2.34.

$$u_t = \sqrt{\frac{4}{3} * \frac{\rho_p - \rho_f}{\rho_f} * \frac{d_{sv} * g}{C_d(Re_p)}} \tag{2.34}$$

where:

$$Re_p = \frac{u_p * d_{sv} * \rho_f}{\mu_f}$$

$C_d(Re_p)$ = drag coefficient as a function of Re_p

Re_p = particle Reynolds number

μ_f = dynamic viscosity of fluid

2.1.4 Fluidization regime diagram by Grace

Grace proposed a unified regime diagram based on literature data to show the operating ranges of fluidized beds. Figure 2.5 includes the particle classification after Geldart and abbreviates the superficial velocity for state i as U_i as in this section. The different particle groups C, A, B, D by Geldart [14, 15] are subsequently described briefly. Group C are fine cohesive materials which tend to channel instead of fluidizing. Group A are fine solids which have a considerable range between minimum and bubbling fluidization and generally fluidize nicely. Group B particles do have an intermediate size and fluidize as soon as u_{mf} is reached. Group D consists of larger particles which poorly mix when fluidized and are easily spouted [16]. The bronze particles used in this work are Geldart group B particles.

The fixed bed transforms to a fluidized bed at U_{mf}. Transition from bubbling to fluidized fluidization, at U_c, is defined by Grace to occur at the maximum of standard deviation of the pressure fluctuation in a fluidized bed. The velocity, U_{se}, where particles are entrained significantly marks the point where the bed material can no longer be maintained in the column and the batch operation is terminated and U_t is the terminal velocity of the particle. [16]

For an idealized system with uniform spherical particles in a steady fluid upwards flow without significant interparticle forces the particle volume fraction of the bed may

be written as in Eq. 2.35 [17]. Assuming uniform spherical particles $d_p = d_{sv}$ is valid. Therefore, ε_p can be described as following function:

$$\varepsilon_p = f(\rho_f, g, \Delta\rho, \mu_f, d_p, u_0) \tag{2.35}$$

where: $\Delta\rho = \rho_p - \rho_f$.

The dimensionless particle diameter, d_p^*, and the dimensionless superficial fluid velocity, u_0^* or U^*, used in Figure 2.5, can be obtained from the Archimedes number, Ar, and Reynolds number, Re_p.

$$Re_p = \frac{u_0 * d_p * \rho_f}{\mu_f} \tag{2.36}$$

$$Ar = \frac{d_p^3 * \rho_f * g * \Delta\rho}{\mu_f^2} \tag{2.37}$$

$$d_p^* = d_p * \left(\frac{\rho_f * g * \Delta\rho}{\mu_f^2}\right)^{\frac{1}{3}} = Ar^{\frac{1}{3}} \tag{2.38}$$

$$u_0^* = u_0 * \left(\frac{\rho_f^2}{\mu_f * g * \Delta\rho}\right)^{\frac{1}{3}} = \frac{Re_p}{Ar^{\frac{1}{3}}} \tag{2.39}$$
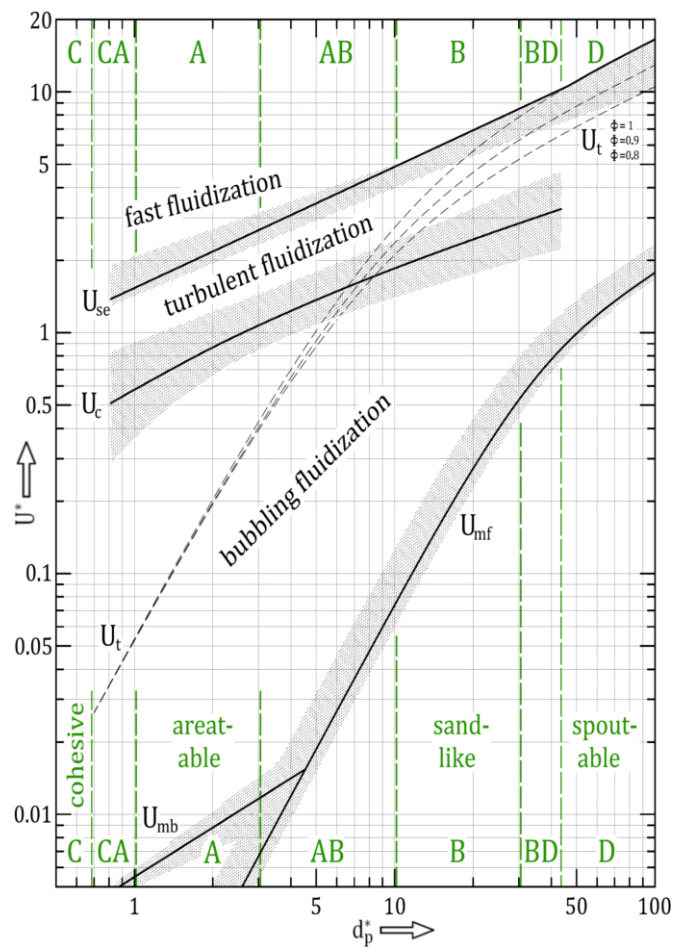
Figure 2.5: Grace diagram [17] adapted by Schmid [2]

2.2 C(P)FD fundamentals

The fundamental concepts of physics, conservation of mass, momentum and energy are mathematically described in the fundamental equations of fluid dynamics, the continuity, momentum and energy equations. The fluid region is divided into finite control volumes by a grid and the governing partial differential equations are discretized and solved in an algebraic equation system for each control volume [18].

Usually, models for fluid and particulate multi-phase flow have either used an Eulerian continuum description for the fluid and solid phase (Eulerian-Eulerian approach) or a continuum approach for the fluid and a Lagrangian description for the particulate phase (Eulerian-Lagrangian approach) [19].

In fluid dynamics the Eulerian approach describes the entire movement of the fluid at any given time, t, at any given location, x, in a velocity field using $u(x, t)$. The Lagrangian description is based on all trajectories $X(t)$ of the fluid (or solid) particles. The particles are distinguished by their respective starting points $x_0 = X(t = t_0)$. To put it simply, the particles are marked and their pathways are tracked in space [20].

The Eulerian-Eulerian approach averages the fluid phase as a continuum and the particulate phase as a pseudo-continuum by a statistical procedure. There are no more discrete particles. This averaging leads to many unclosed terms which need to be closed and must be modeled. If a particle size distribution is used, with the Eulerian-Eulerian approach separate continuity and momentum equations for each size and type must be solved [21].

The particle phase can also be modeled as discrete computational particles by different approaches, like direct numerical solution (DNS), discrete element method (DEM) or multi-phase particle in cell (MP-PIC) method [21].

The DNS method models the gas flow field at scales much smaller than the size of the particles and the interaction is incorporated using stick boundary conditions at the particle surface [22]. The Navier-Stokes equations are solved without any turbulence model and the momentum exchange is solely determined by the interaction of the fluid with the particle surface [23]. Due to the high computational cost the number of particles is limited to small numbers (10^2-10^3). Because of the limited particle number DNS is not applicable for e.g cold flow models and large-scale applications. DNS is used to study fundamental solid-fluid flow behavior. For instance, it can be used to construct drag laws for gas-solid systems or developing other close models for the fluid-particle interactions needed in continuum models. [21, 22].

The DEM method models discrete particles transferring momentum to the fluid using a drag closure model [21]. The particles are semi-rigid and particle-particle forces are calculated directly contact by contact using a spring-damper model [24]. This allows simulations with a wide range of particle types and sizes. Due to the high collision frequency and resulting computational cost, for volume fractions above 5%, the method is usually limited to the order of 10^5 particles and therefore too computing intensive for e.g. large-scale plants [21]. Therefore, a new method, the MP-PIC method, was developed.

The advantage of possible high particle counts of an Eulerian approach and the advantage to simulate particles with different sizes, types and velocities of an Lagrangian approach is combined by the MP-PIC method.

2.2.1 MP-PIC

The MP-PIC approach is an Eulerian-Lagrangian approach, modeling the fluid phase as a continuum and the particulate phase as Lagrangian numerical particles, which are particles with the same properties like size, type and species grouped together in "clouds". The position of those clouds is tracked in a Lagrangian sense, but the collision of the particles is resolved by a continuum stress model [25] (see Eq. 2.50).

An Eulerian continuum-continuum model already allowed modeling of dense particle flows, but modeling a distribution of types and sizes of particles required the solving of separate continuity and momentum equations. Traditional Lagrangian approaches to simulate dense particle flows experienced difficulties with higher particle volume fractions due to the high computational cost to calculate particle interaction. Those problems can be eliminated by grouping particles in numerical particles with identical properties, mapping those particle properties to an Eulerian grid and mapping back computed stress tensors to the particle positions. The particle-particle collisions are not resolved anymore by a costly spring-damper model but predicted in a continuum approach, making simulation of dense particle flows possible with an Lagrangian method. In the MP-PIC method, particles are treated both as particles and continuum [21, 25].

2.2.2 Governing equations

The governing equations in Barracuda are listed in this section.

2.2.2.1 Equations for fluid phase

The continuity equation for the fluid without mass transport ($\delta \dot{m}_p = 0$) is [21]:

$$\frac{\partial \left(\varepsilon_f \rho_f \right)}{\partial t} + \nabla \cdot \left(\varepsilon_f \rho_f \boldsymbol{u}_f \right) = \delta \dot{m}_p = 0 \tag{2.40}$$

The momentum equation for the fluid [21] with the interphase momentum transfer function $\boldsymbol{F}$ (see Eq. 2.49) is:

$$\frac{\partial (\varepsilon_f \rho_f \boldsymbol{u}_f)}{\partial t} + \nabla \cdot \left(\varepsilon_f \rho_f \boldsymbol{u}_f \boldsymbol{u}_f \right) = -\nabla p + \boldsymbol{F} + \varepsilon_f \rho_f \boldsymbol{g} + \nabla \cdot \left(\varepsilon_f \boldsymbol{\tau}_f \right) \tag{2.41}$$

with the stress tensor in index notation

$$\tau_{f,ij} = \mu \left(\frac{\partial u_i}{\partial x_j} + \frac{\partial u_j}{\partial x_i} \right) - \frac{2}{3} \mu \delta_{ij} \frac{\partial u_k}{\partial x_k} \tag{2.42}$$

where μ is the sum of laminar shear and turbulence viscosity and x_i is the spatial variable.

In Barracuda the Large Eddy Simulation (LES) turbulence model was chosen. The large eddies are calculated from the flow equations and Barracuda uses the Smagorinsky subgrid scale (SGS) model to capture the subgrid turbulence [5, 24]. The form of the SGS eddy viscosity is:

$$\mu_t = C_s * \rho_f * \varepsilon_f * \Delta^2 * |\bar{S}| \tag{2.43}$$

$$|\bar{S}| = \sqrt{2 * S_{ij}^2} \tag{2.44}$$

$$S_{ij} = \frac{1}{2} * \left(\frac{\partial u_i}{\partial x_j} + \frac{\partial u_j}{\partial x_i} \right) \tag{2.45}$$

where:

C_s = Smagorinsky constant [26]
μ_t = turbulent viscosity of fluid
Δ = $(\delta x \delta y \delta z)^{1/3}$ is the filter length scale
S_{ij} = strain rate tensor

2.2.2.2 Equations for particulate phase

The particle acceleration, as described in Eq. 2.46, was extended with an additional term, the modified acceleration due to contact stress. For further information the reader is referred to O'Rourke et al. [27].

$$\boldsymbol{a}_p = D\left(\boldsymbol{u}_f - \boldsymbol{u_p}\right) - \frac{1}{\rho_p}\nabla p + \boldsymbol{g} - \frac{1}{\varepsilon_p \rho_p}\nabla \tau_p + \frac{\bar{\boldsymbol{u}}_p - \boldsymbol{u}_p}{\tau_D} \tag{2.46}$$

$\bar{\boldsymbol{u}}_p$ is the particle mean velocity and τ_D is a damping time due to inelastic particle collisions (see [27]). The particle normal stress, τ_p, used will be discussed in greater detail in Section 2.2.3.

The particle acceleration for the particles is calculated using a blended particle acceleration model developed by O'Rourke and Snider [27]. In polydisperse granular beds relative motion of particles of different sizes is inhibited if closely packed, as modeled by the blended acceleration model. Without the blended model a higher degree of particle segregation occurs [5].

The MP-PIC method used in Barracuda describes the dynamics of the particle phase using the particle probability distribution function $f\left(\boldsymbol{x}, \boldsymbol{u}_p, \rho_p, V_p, t\right)$. The evolution of the particle phase is determined by solving a Liouville equation for f [19]:

$$\frac{\partial f}{\partial t} + \nabla \cdot \left(f \boldsymbol{u}_p\right) \nabla_{\boldsymbol{u}_p} \cdot \left(f \boldsymbol{a}\right) = 0 \tag{2.47}$$

$\nabla_{\boldsymbol{u}_p}$, used in Eq. 2.47, is the divergence operator with respect to velocity.

The particle volume fraction is related to f by Eq. 2.48 [19]:

$$\varepsilon_p = \iint f \frac{m_p}{\rho_p} dm_p d\boldsymbol{u}_p \tag{2.48}$$

The interphase momentum transfer function per volume is defined as [19]:

$$\boldsymbol{F} = -\iint f\left(m_p\left[D(\boldsymbol{u}_f - \boldsymbol{u}_p) - \frac{\nabla p}{\rho_p}\right]\right) dm_p d\boldsymbol{u}_p \tag{2.49}$$

2.2.3 Particle normal stress

The used particle stress model is an extension from the model by Harris and Crighton [28]. An earlier approach by Snider et al. [29] was an implicit scheme for calculating the volume fraction and particle normal stress on the Eulerian grid. The implicit calculation of the volume fraction was used solely to calculate the particle normal stress. The calculation was discarded at the end of a calculation step and the final volume fraction was calculated from mapping particle volumes to the grid [29]. A new particle stress model presented by Snider [25] models the particle normal stress by a continuum calculation of the particle pressure and applies the subsequent normal stress force to discrete particles. The new Lagrangian discrete particle stress model which uses the stress gradient, is faster and eliminates the need for an implicit solution for the particle volume fraction and particle normal stress [25]. In a dense flow it is difficult to calculate the particle stress gradient for each particle, therefore the particle stress gradient is calculated as a spatial gradient (as a gradient on the grid) and mapped back to the particles to calculate the particle-particle interaction forces [30]. The particle normal stress is calculated dependent on the particle volume fraction and other constants as:

$$\tau_p = \frac{P_S * \varepsilon_p^{\beta}}{max[\varepsilon_{cp} - \varepsilon_p, \alpha(1 - \varepsilon_p)]} \tag{2.50}$$

The particle normal stress, τ_p, models the particle-particle interactions and is only important near close-pack and has little effect elsewhere [25]. The constants α, a very small number to avoid dividing by zero, and β are dimensionless. The constant P_S has the units of pressure and by adjusting it the particle normal stress can be influenced. As Eq. 2.50 shows, τ_p increases rapidly as the particle volume fraction approaches the close-pack volume fraction and further packing is prevented [24].

2.3 Barracuda cold flow literature

Kraft [23] already reviewed relevant studies published using Barracuda in his PhD thesis which covered mainly the years 2013 to 2016. A short overview of what he covered will be given briefly and afterwards insights in more recent studies. As he already summarized Barracuda was used for studies over a broad range of fluidization regimes ranging from bubbling beds [31, 32, 33], spouting beds [34], circulating beds [35], risers [36, 37, 38, 39, 40, 41] and full loop circulating fluidized beds (CFBs) [42, 43, 44]. The latter will be described shortly.

A full-loop CFB, consisting of a bubbling fluidized bed, a fast fluidized bed, two loop seals, a riser and a cyclone, was simulated by Clark et. al [42]. The flow behavior in the simulation matched well with video recordings and the pressure drops were reasonably accurate, while bed material circulation rates were not measured by the author and can not be evaluated.

Wang et al. [43] simulated a circulating fluidized consisting of a fast fluidized bed, cyclone and a U-type loop seal to investigate the influence of various modeling parameters. They used the Wen-Yu drag model, two different configurations of WYE, and the Ganser drag model. Compared to experimental data the Wen-Yu drag model predicted the particle circulation rate best while the standard WYE drag predicted the total pressure drop best. Ganser overestimated both the pressure drop and particle circulation rate in this simulation.

For a chemical looping process two different set-ups of a fluidized bed were tested by Hamilton et al. [44] using the Wen-Yu drag model, which overpredicted the drag force in the simulation. They tested a CFB and a bubbling bed (BB) set-up, both were built up of an air and fuel reactor connected by loop seals and cyclones where applicable. They compared circulation rate, residence time and velocity distribution but no pressure distribution. The simulated particle circulation rates of the CFB were higher but provided good predictions of the trend, while the circulation rates of the BB did not agree with the experimental data and failed to predict the dependences.

More recent studies were also done on riser and pneumatic conveying, minimum fluidization velocity and CFBs.

Amarasinghe et al. [45] simulated the fluidization of three different particles of Geldart types: zirconia material (group A), bronze (group B) and steel (group D). The simulations were conducted using the different drag laws available in Barracuda. The best results were obtained with Wen-Yu and WYE. The predictions for bronze and steel particles corresponded well with the experiments and the results of the zirconia

material were not comparable to experimental results.

Ariyaratne et al. [26] used Barracuda and its MP-PIC method for simulation for pneumatic conveying of very dilute phase flows in a horizontal pipe using the WYE drag model. The results were compared with previous results of Tsuji and Morikawa [46] and predicted the pressure drop with a deviation case-depended of 4% to 20% while reproducing the general trend of the experimental velocity profiles.

The performance of riser terminators, using the Wen-Yu drag model, were simulated by a set-up of a riser, riser terminator and part of a free-board, while testing two different types of terminators by Kodam et al. [24]. The results indicated that a better separation efficiency with slots-elbow terminator compared to a disk terminator can be achieved. The simulation was not validated with real data or experiments.

Bobek et al. [47] simulated a vortexing circulating fluidized bed, using the Wen-Yu drag law, with different superficial velocities up to $150^{m}/_{s}$ (equal to 1153 times the u_{mf}) and compared it with experimental data. The set-up consisted of a vortexing bed, recirculation pipes, drive screw feeder, and tangential entrance for gas flow. Geldart group B particles made out of HDPE (high density polyethylene) were used. Comparison to the experimental data showed similarities in the pressure profiles. Qualitatively the vortex's flow structure was consistent. Big differences were observed in total mass in system, total pressure drop and the mass flow behavior in the recirculation section. Physical characteristics like frictional and static electricity effects were not considered.

Adkins et al. [48] conducted cold flow experiments to validate CPFD simulations. The WYE and the Parker drag model were used, a fixed fluidized and a circulating fluidized bed. The WYE drag model overestimates drag forces in fixed and CFB, especially the riser as mentioned by Li et al. [49], while a modified drag correlation, with an increased P_S value in the stress model, derived by Parker improved the correlation of data and simulation in both application and provides a useful starting platform for catalyst-biomass hydrodynamics simulation in CFBs.

A high-density circulating fluidized bed simulation was conducted by Ma [50] using the EMMS model evaluating the pressure distribution, solid circulation rate and tracking the solids residence time. The model included a riser, connected at the upper end to a cyclone leading the particles into a stand-pipe which connects again to the lower end of the riser via a j-leg. While the predicted pressure distribution deviated from the experimental data in dense regions of the riser, the solid circulation rate in the loop was predicted with a maximum relative error less than 10% in all cases of this study.

Kraft et al. [51] simulated a dual fluidized bed with EMMS, Ganser, Turton-Levenspiel, and WYE drag laws. The pressure at distinct points and the recirculation rate of the bed

material were measured. The set-up consisted of a gasification reactor, a combustion reactor, a chute, a cyclone and a loop seal. The best results for pressure distribution were predicted by the EMMS drag law, while Ganser, Turton-Levenspiel, and WYE underestimated the pressure at the bottom. The best particle recirculation rates were achieved using the Ganser drag law, while EMMS's were notably lower. The different drag laws were able to predict the recirculation rates in most cases within a range of 25% or less, excluding the results of the EMMS drag law, but did not predict the trends correctly.

Based on the literature review the EMMS, Ganser and WYE drag laws will be tested. Generally spoken the WYE and Ganser drag law cover both dense and dilute flow while they seem to overpredict the drag force in some cases. The EMMS is also a viable option in terms of predicting the pressure distribution while underpredicting particle circulation rates in some cases.

3 Overview of simulation

The simulation was conducted trying different settings. Settings like the drag law, mesh size, fluidization rate, particle stress parameter P_S constant, and geometry were subject of variation. The influence of the modified settings was investigated and if applicable quantified. The best set-up was determined step-by-step to find the best fit for the simulation compared to the real cold flow model. Table 3.2 gives an overview over all conducted simulations in this thesis and will be referred to at the beginning of each section. The letters used as indices are described in Table 3.1.

The simulations were conducted using Barracuda VR® version 17 from the company CPFD Software, LLC. The hardware infrastructure was a workstation with an Intel Core i5-3570, 16 GB RAM, and a GeForce TITAN X graphics card.

Table 3.1: Indices for simulation overview (Table 3.2)

a	Drag Law	EMMS used as drag law	l	Pipe diameter	Pipe diameter was not altered
b		Ganser used as drag law	m		Pipe diameter of pipe connecting ULS and AR SEP increased from $32mm$ to $40mm$
c		WYE used as drag law	n		All pipe diameters increased from $32mm$ to $40mm$
d	FR Gap	FR Gap $16mm$	o	AR	AR air flow set to $24^{Nm^3/h}$
e		FR Gap $18mm$	p		AR air flow set to $20^{Nm^3/h}$
f		FR Gap $20mm$	q		AR air flow set to $16^{Nm^3/h}$
g	P_S	P_S set to $1Pa$	r	FR	FR air flow set to $12^{Nm^3/h}$
h		P_S set to $30Pa$	s	Loop seal	Loop seal fluidization rate not increased
i		P_S set to $50Pa$	t		Loop seal fluidization rate increased by factor 1.75
j		P_S set to $65Pa$	u		Loop seal fluidization rate increased by factor 2.5
k		P_S set to $100Pa$			

Abbreviation	Name	Drag Law			FR Gap				P_S				Pipe diam.			AR			FR		Loop seal	
		a	b	c	d	e	f	g	h	i	j	k	l	m	n	o	p	q	r	s	t	u
E1	GEOM_EMMS_Geom2_16_300k	x			x			x					x			x			x	x		
E2	SETTING_EMMS_Geom2_16_500k_PS30	x			x				x				x			x			x	x		
E3	SETTING_EMMS_Geom2_16_500k_PS30_changed	x			x				x				x			x			x	x	x	
G1	FLOW_Ganser_Geom2_18_ULS40_500k_ULS_and_LLS_changed_without_weigthing		x			x		x						x		x			x		x	
G2	GEOM_Ganser_Geom2_16_300k_RERUN		x		x			x					x			x			x	x		
G3	GEOM_Ganser_Geom2_16_500k		x		x			x					x			x			x	x		
G4	GEOM_Ganser_Geom2_18_ULS40_500k		x			x		x						x		x			x	x		
G5	GEOM_Ganser_Geom2_20_Large_500k		x				x	x							x	x			x	x		
G6	SETTING_Ganser_Geom2_16_150k_PS50		x		x					x			x			x			x	x		
G7	SETTING_Ganser_Geom2_16_300k_PS50		x		x					x			x			x			x	x		
G8	SETTING_Ganser_Geom2_16_400k_PS50		x		x					x			x			x			x	x		
G9	SETTING_Ganser_Geom2_16_500k_PS30		x		x				x				x			x			x	x		
G10	SETTING_Ganser_Geom2_16_500k_PS30_changed		x		x				x				x			x			x	x	x	
G11	SETTING_Ganser_Geom2_16_500k_PS30_changed_AR16		x		x				x				x					x	x	x	x	
G12	SETTING_Ganser_Geom2_16_500k_PS30_changed_AR20		x		x				x				x				x		x	x	x	
G13	SETTING_Ganser_Geom2_16_500k_PS30_changedx2		x		x				x				x			x			x			x
G14	SETTING_Ganser_Geom2_16_500k_PS50		x		x					x			x			x			x	x		
G15	SETTING_Ganser_Geom2_16_500k_PS50_AR16		x		x					x			x					x	x	x		
G16	SETTING_Ganser_Geom2_16_500k_PS50_AR20		x		x					x			x				x		x	x		
G17	SETTING_Ganser_Geom2_16_500k_PS65		x		x						x		x			x			x	x		
G18	SETTING_Ganser_Geom2_16_500k_RERUN_PS100		x		x							x	x			x			x	x		
G19	SETTING_Ganser_Geom2_16_80k_PS50		x		x					x			x			x			x	x		
G20	SETTING_Ganser_Geom2_18_500k_PS30_changed		x			x			x				x			x			x	x	x	
G21	SETTING_Ganser_Geom2_18_500k_PS50		x			x				x			x			x			x	x		
G22	SETTING_Ganser_Geom2_18_ULS40_500k_PS100		x			x						x		x		x			x	x		
G23	SETTING_Ganser_Geom2_18_ULS40_500k_PS30		x			x			x					x		x			x	x		
G24	SETTING_Ganser_Geom2_18_ULS40_500k_PS50		x			x				x				x		x			x	x		
G25	SETTING_Ganser_Geom2_18_ULS40_500k_PS65		x			x					x			x		x			x	x		
G26	SETTING_Ganser_Geom2_20_500k_PS30_changed		x				x		x						x	x			x	x	x	
W1	GEOM_WYE_Geom2_16_300k			x	x			x					x			x			x	x		
W2	GEOM_WYE_Geom2_16_500k			x	x			x					x			x			x	x		
W3	SETTING_WYE_Geom2_16_500k_PS30			x	x				x				x			x			x	x	x	
W4	SETTING_WYE_Geom2_16_500k_PS30_changed			x	x				x				x			x			x	x		x

Table 3.2: Overview of all conducted simulations

3.1 Description of the cold flow model

The cold flow model described in this thesis was used for experiments by Martinovic [52]. All the data from the cold flow model to model and validate the simulation are obtained from Martinovic's work.

3.1.1 Geometry

The CAD software Autodesk Inventor Professional 2018 was used to design and adapt the cold flow model pictured in Figure 3.1. The simulations have been conducted with slightly varied geometries. In some simulations the spacing of the built-ins in the FR column and some pipe diameters were altered (see Table 3.2). All modifications are highlighted and described in the regarding chapter. The main parts of the designed virtual cold flow model are listed in Table 3.3 and their location is shown in Figure 3.1.

Table 3.3: Model parts - abbreviation and overview

AR	Air reactor
AR SEP	Air reactor separator
FR	Fuel reactor
FR junction	Fuel reactor junction
FR (BB)	Fuel reactor bubbling bed
FR SEP	Fuel reactor separator
ILS	Inner loop seal
LLS	Lower loop seal
ULS	Upper loop seal
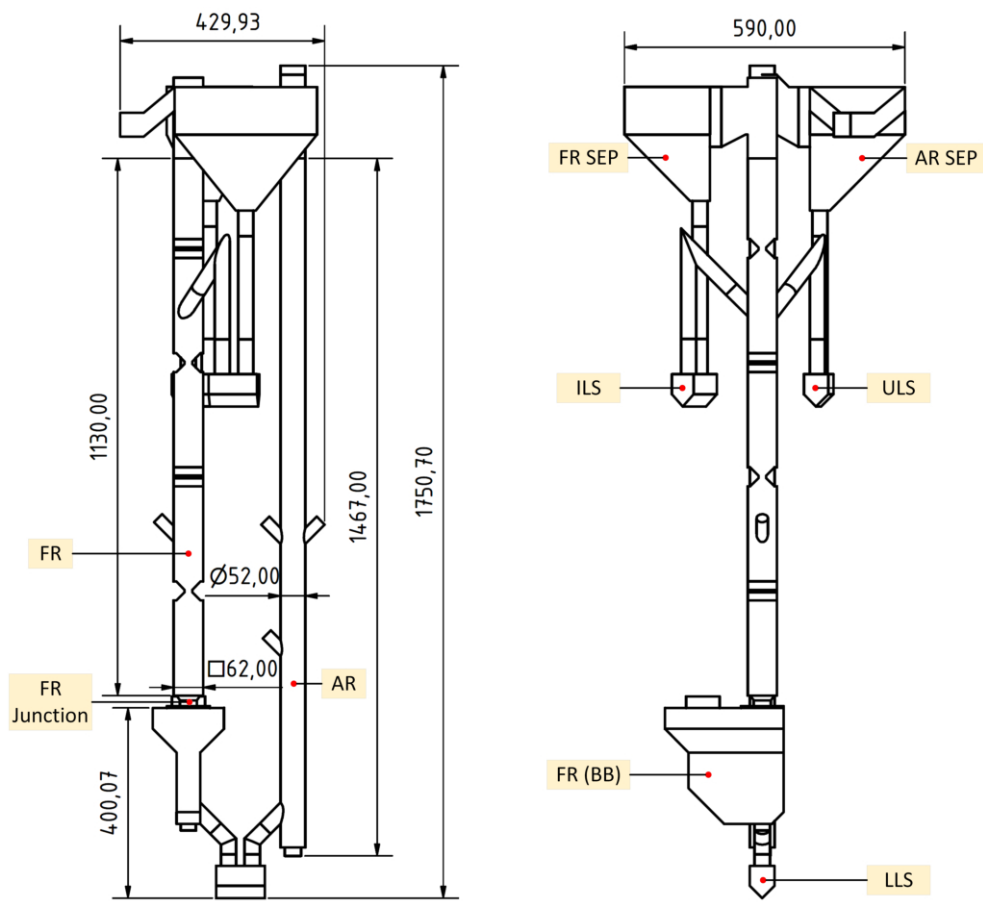
Figure 3.1: Model - overview
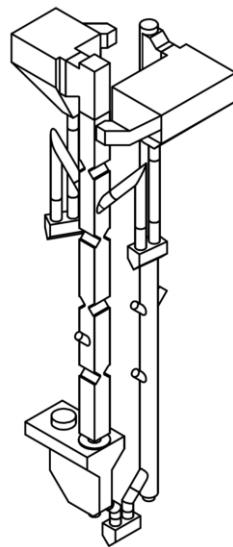
Figure 3.2: Model - isometric view

3.1.1.1 FR junction

The junction between the FR column and bubbling bed, henceforth called *FR junction*, was a result of the column being connected to the bubbling bed. The used FR junction shape, called *"Geom2"* as seen in Figure 3.3, was slightly altered and simplified from the original shape. The level of detail of the original geometry would be too fine for the resolution of the mesh and was therefore simplified. The lower cylindrical elevation with a diameter of 90mm is caused by connectors between the FR column and the bubbling bed.
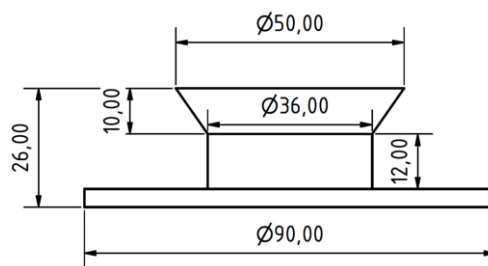
Figure 3.3: FR junction - simplified "Geom2"

3.1.1.2 FR gap

The FR column has built-ins to narrow the cross-section resulting in segmented compartments. The formation of smaller fluidized beds is enabled in those sections due to the reduced gap width. Those built-ins do have a defined gap width of 16mm (see Figure 3.4) but were eventually altered in the CAD model to 18mm and 20mm to study their influence.

(a) Built-ins 16mm gap   (b) Built-ins 18mm gap
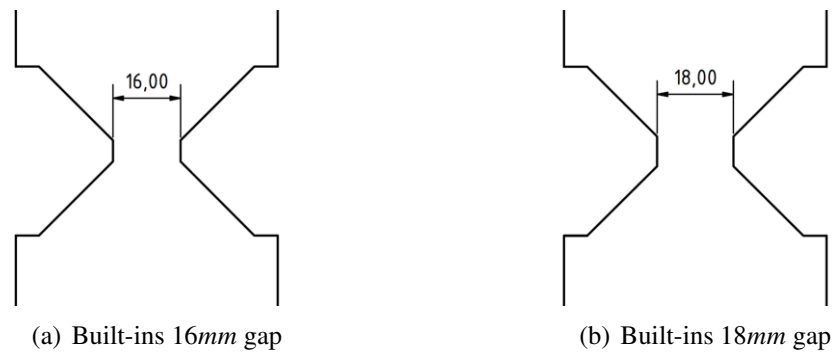
Figure 3.4: FR column gap - built-ins spacing

3.2 General settings

In this section the general settings are described. The simulations had mainly the same settings and only differed in a few aspects like drag law, geometry or specific parameters. Those adaptations are specifically addressed in the regarding chapters. The simulations were conducted without chemical reactions, isothermal at $300K$, and air as a compressible fluid. On average the computing time to calculate $1s$ in the simulation was approximately $3h$.

3.2.1 Grid

In Barracuda the grid is determined by a rectangular cuboid mesh overlapping with the STL file of the model, which was generated with the CAD software Autodesk. The intersections define the outline of the mesh and the resulting real cell number. Therefore, by varying the total number of cells the total number of real cells was adjusted. When talking about the grid in this thesis the factor thousand is abbreviated by the lower-case letter "k" (e.g. $300k \approx 300\,000$ cells). The number of real cells was set between roughly $300k$ to $500k$ real cells for the simulations. To generate a better resolution on important parts (i.e. the built-in applications to interfere with the stream in the FR column) the mesh got manipulated by adding grid lines manually. This resulted in the mesh as described in Table 3.4. The average side length of a cell was calculated by calculating the side length of a cube with the average cell volume. Those values varied slightly if the geometry was altered.

Table 3.4: Grid settings

	$80k$	$150k$	$300k$	$400k$	$500k$
Real cell number	82\,507	149\,314	296\,492	402\,040	483\,338
Average cell volume [mm^3]	385.01	213.34	107.53	79.32	65.95
Average cell side length [mm]	7.27	5.98	4.76	4.30	4.04

3.2.2 Base materials

The simulation was run using air as the fluid and bronze particles as the solid phase. For air an already predefined material was chosen, which is implemented in Barracuda, with a predefined composition (see Table 3.5) and properties (see Table 3.6) [5]. The

bronze particles density and close-pack density values were taken from Martinovic's thesis [52] (see Table 3.7).

Table 3.5: Air composition

Component	Volume fraction
N_2	0.780840
O_2	0.209476
Ar	0.009365
CO_2	0.000319
Total	**1.000000**

Table 3.6: Air properties

Molar mass $\left[\frac{g}{mol}\right]$	28.9652
Viscosity $[Pa * s]$	$1.844687 * 10^{-5}$
Mass diffusivity $\left[\frac{m}{s^2}\right]$	0
Flow type	compressible

Table 3.7: Bronze particle properties [52]

ρ_p	$8800 \, kg/m^3$
ρ_{bulk}	$5100 \, kg/m^3$
ε_{cp}	0.57955

For compressible gas materials, the ideal gas law is used to calculate the gas density ρ_f in Barracuda [5].

$$\rho_f = \frac{p}{RT} * M \tag{3.1}$$

Assuming a temperature of $300K$ and a pressure of $101325Pa$ the resulting density is calculated in Eq. 3.2.

$$\rho_f = \frac{101325Pa}{8.3145\frac{J}{mol\,K} * 300K} * 0.0289652\frac{kg}{mol} = 1.177\frac{kg}{m^3} \tag{3.2}$$

The close-pack volume fraction ε_{cp} is calculated by dividing the bulk density by the particle density.

$$\varepsilon_{cp} = \frac{\rho_{bulk}}{\rho_p} = \frac{5100\frac{kg}{m^3}}{8800\frac{kg}{m^3}} = 0.57955 \tag{3.3}$$

where:

R = gas constant $\left(8.3145 \, \frac{J}{mol\,K}\right)$

3.2.2.1 Particle settings

Table 3.8: Bronze particle settings used for the simulations

Maximum momentum redirection from collision	40%
Blended acceleration model for the contact force	on
P_S constant [Pa]	1 to 100
B constant (β in Eq. 2.50)	3
ϵ constant (α in Eq. 2.50)	$1 * 10^{-8}$
Normal-to-wall momentum retention	0.85
Tangent-to-wall momentum retention	0.85
Diffuse bounce	0

The total number of particles ($\sim 1.16 * 10^{10}$) were determined automatically by the total particle mass in the system. The number of numerical particles also depends on the mesh. The size of the numerical particle should be smaller than the cell, therefore a coarser mesh allows more particles per numerical particle (*"cloud"*) than a finer mesh. The particles per cloud were determined automatically and could be influenced by adjusting the cloud resolution setting. The global cloud resolution was set to *medium* in Barracuda. All simulations with a mesh size of $500k$ real cells had roughly the same total number of numerical particles. The simulations in the mesh sensitivity analysis also had the same number of numerical particles due to being initialized with initial conditions of a simulation with $500k$ real cells. The only exception are the simulations in Section 5.3.1.1, which were initialized with $300k$ real cells.

Table 3.9: Number of numerical particles

Real cell number	Total number of numerical particles
$300k$	$\sim 9.40 * 10^5$
$500k$	$\sim 2.19 * 10^6$

3.2.2.2 Particle size distribution

The particle size distribution ("PSD") was taken from the MasterSizer analysis of Martinovic's thesis [52]. The Sauter mean diameter, d_{sv}, is $81.7 \mu m$ with a PSD pictured in Figure 3.5. The input values for the simulation are listed in Table 3.10.

Table 3.10: Cummulative PSD

Particle Size Upper Limit [μm]	Cumulative Percent [%]
34.674	0.0000
39.811	0.0100
45.709	0.2100
52.481	1.9402
60.256	8.1808
69.183	20.7421
79.433	40.7641
91.201	62.9863
104.713	82.3582
120.226	93.2793
138.038	98.8399
158.489	99.8900
181.970	100.0000
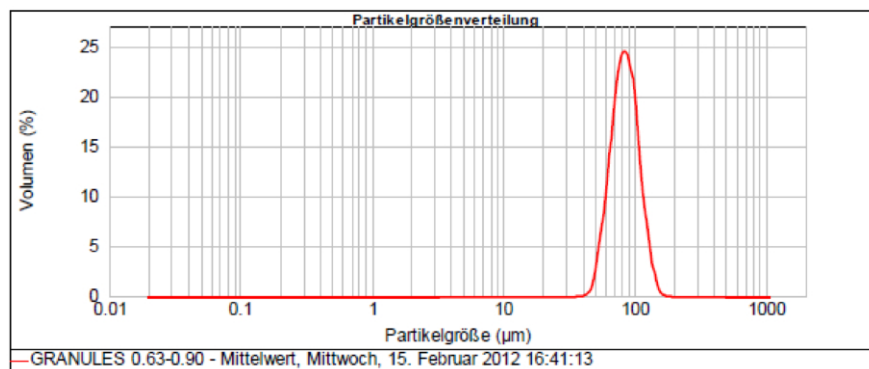
Figure 3.5: PSD of bronze bed material [52]

3.2.3 Boundary conditions

For the simulation two types of boundary conditions, flow and pressure boundary conditions, were necessary. The flow boundary conditions are denoted as *"injection boundary conditions"* as they are labeled in Barracuda. The fluid enters the system through the injection BC with a defined mass flow via a set area. The area and mass flow of each injection BC can be split up to various desired locations as spots, so-called *jets*. The boundary conditions are labeled and visualized in Figure 3.6.
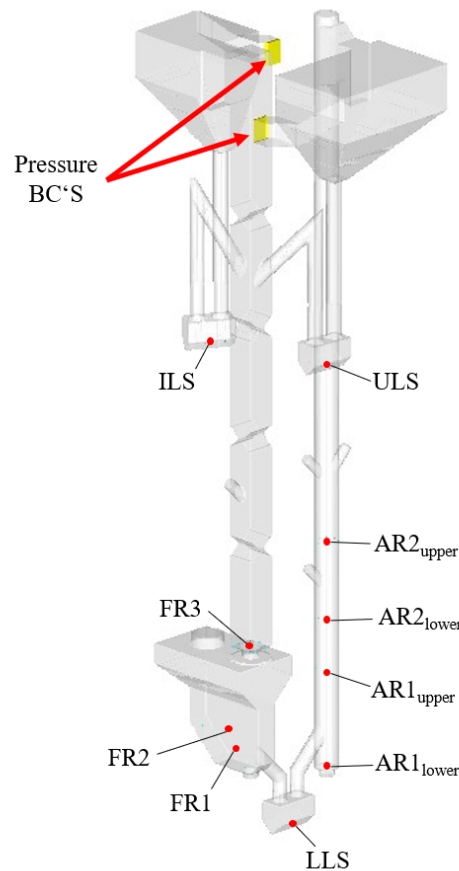
Figure 3.6: Boundary conditions for the simulation geometry

3.2.3.1 Pressure BC's

The pressure boundary conditions were set at the exit of the AR SEP and FR SEP with $101325Pa$. Based on experiments by Martinovic [52] it can be assumed that with this geometry the solid and fluid phase is separated completely in the AR SEP and FR SEP. Therefore, the pressure BC was set to only let fluid pass through those planes in order that the particles remained in the system.

3.2.3.2 Injection BC's

A total of 10 different injection boundary conditions were set with a total of 94 spots for air injection. Because *FR3* was always set to zero a total of 9 different injection boundary conditions with 54 spots were actually used. Alignment and orientation of the individual jets are pictured in Figure 3.7 and location and amount are listed in

Table 3.11. The area listed in Table 3.11 is the total cross-sectional area of the real inlets at its specific location. The total area and air flow is split up evenly to each jet.

(a) $AR1_{lower}$ (b) $AR1_{upper}$ (c) $AR2_{lower}$ (d) $AR2_{upper}$

(e) FR1 and FR2 (f) FR3 (g) Loop seals
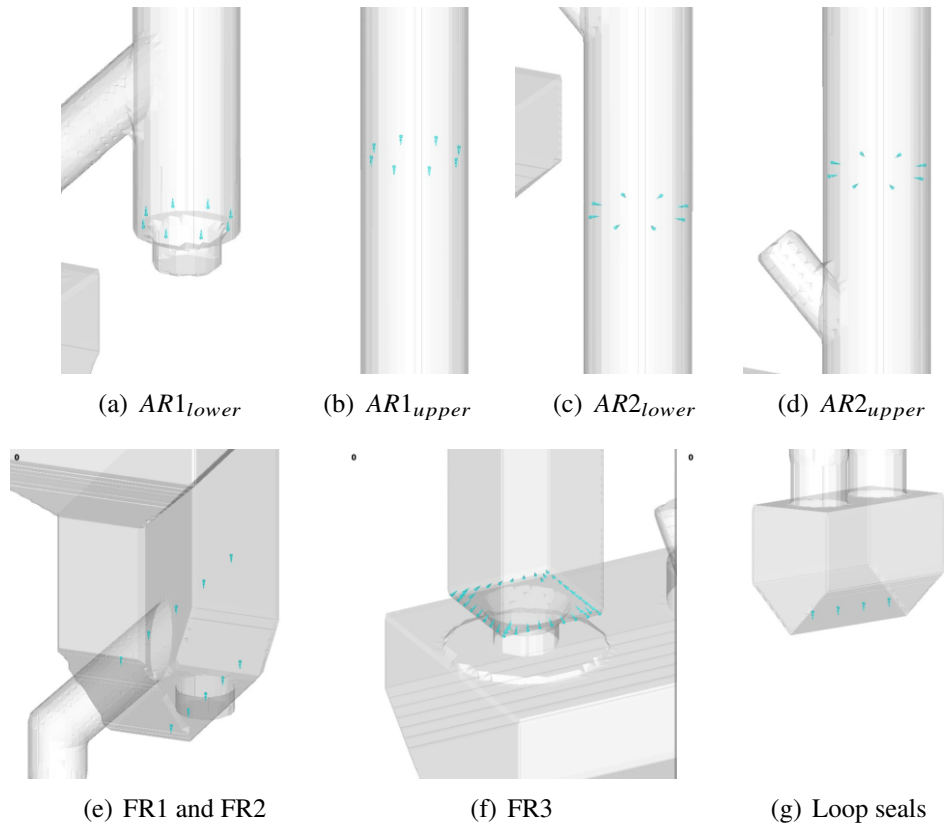
Figure 3.7: IC injection jets arrangement

For the injection at AR1 and AR2 the total air volume flow was split. AR1 was split into $AR1_{lower}$ and $AR1_{upper}$. AR2 was split into $AR2_{lower}$ and $AR2_{upper}$. The distribution of AR1 to $AR1_{lower}$ and $AR1_{upper}$ was split up accordingly to their area of the injection BC. The total air flow in the AR between AR1 and AR2 was always distributed equally therefore $\frac{\dot{V}_{AR1}}{\dot{V}_{AR2}} = 1$. As an example if $24^{Nm^3}/h$ were injected into the AR a total of $12^{Nm^3}/h$ would be set to flow into AR1. So if a total of $12^{Nm^3}/h$ were injected at AR1, the respective air flows will be calculated as shown in the example Eq. 3.4. The standard case is listed in Table 3.13 and other AR volume flows were calculated accordingly if the conditions were altered.

Table 3.11: Injection BC - jets

	Number of jets	Height [mm]	Area [mm^2]
FR1	5	164.07	888.58
FR2	5	222.07	1999.30
FR3	40	426.40	1553.78
$AR1_{lower}$	8	111.00	1005.31
$AR1_{upper}$	8	326.00	2261.95
$AR2_{lower}$	8	425.00	2261.95
$AR2_{upper}$	8	601.00	1005.31
LLS	4	11.00	399.86
ULS	4	1044.70	399.86
ILS	4	1045.07	399.86

$$AR1_{lower} = 12\frac{Nm^3}{h} * \frac{AR1_{lower}}{AR1_{lower} + AR1_{upper}} \tag{3.4}$$

$$= 12\frac{Nm^3}{h} * \frac{1005.31mm^2}{3267.26mm^2} = 3.69\frac{Nm^3}{h}$$

The air volume flow was set as listed in Table 3.12.

In Martinovic's thesis the lower loop seal fluidization rate was added to describe the total AR and FR flow. In this thesis the same settings were used, but the loop seal fluidization rate was not added when describing the AR and FR flow. Therefore, an AR flow of 24$^{Nm^3}/_h$ is eventually listed as 24.4$^{Nm^3}/_h$ with the same settings in his thesis.

Table 3.12: Air injection mass flow [52]

	Volume flow $\left[\frac{Nm^3}{h}\right]$
AR1	12
AR2	12
FR1	2
FR2	10
FR3	0
LLS	0.8
ULS	0.8
ILS	0.6
AR_{Gesamt}	24
FR_{Gesamt}	12

Table 3.13: AR air flow split

		Volume flow $\left[\frac{Nm^3}{h}\right]$
AR1	$AR1_{lower}$	3.69
	$AR1_{upper}$	8.31
AR2	$AR2_{lower}$	8.31
	$AR2_{upper}$	3.69

3.2.4 Initial conditions

3.2.4.1 Particle distribution IC

The overall mass of particles was always about $25kg$ [52] in the simulations but could slightly vary due to the initialization. Different particle initial conditions (*"ICs"*) were used in the simulations. The first option was distributing close-pack amounts of particles in the model (see Figure 3.8a). During this work, Barracuda updated its software and implemented a new feature which allowed to distribute a certain mass of particles in a designated region, e.g. the FR column (see Figure 3.8b). In first simulations, it was observed that the total mass in the FR column started to raise at the beginning before reaching a steady state, the initial mass of the column could be influenced more precisely using this option. With the already mentioned update another feature was implemented that made is possible to start a simulation from existing initial conditions of a previous simulation, a so-called *"IC file"*. Using an IC file the initial condition could be a real operating point of an existing simulation at a certain time step (see Figure 3.8c). Therefore, the time needed to reach a steady state can be reduced.

Generally spoken, the initial conditions for particles were altered in an approach trying to reduce the simulation time by redistributing the particles from the beginning to reach a steady state earlier. This led to different initial conditions ranging from distributed closed pack areas, areas with looser particle volume fractions and initial conditions based on a previous simulation. The different states of initial particle mass

in the model are visualized in Figure 3.8.

(a) close-pack distribution

(b) Defined distribution of particle mass

(c) start from an IC file
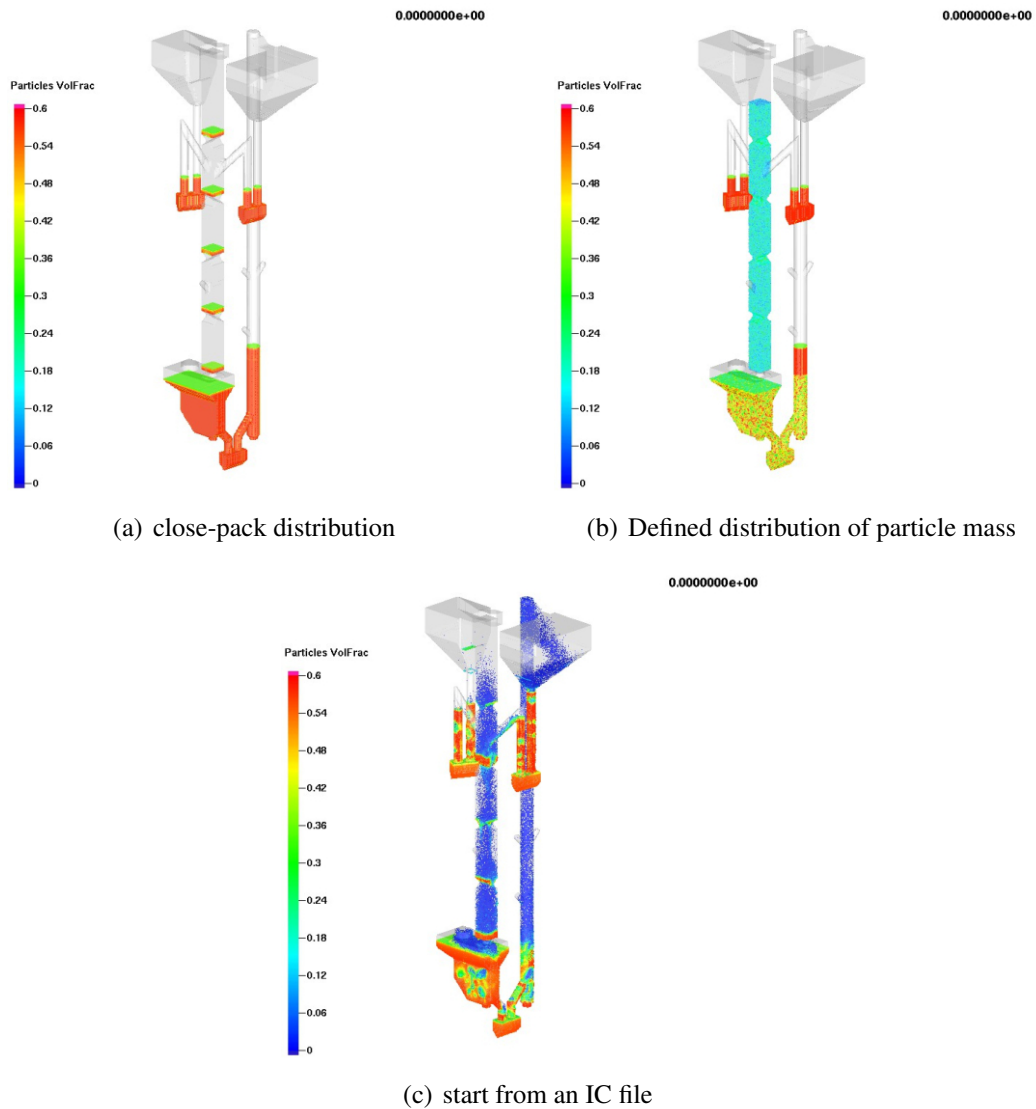
Figure 3.8: Particle IC - overview

3.2.4.2 Fluid IC

For the fluid initial conditions of the simulation the model was filled with air at $101325Pa$. As already mentioned Barracuda was updated with the option to start a simulation from an existing operating point. Therefore, this option was also used after this feature was implemented.

3.2.5 Numerics

The default values of the solver settings were used and are listed in this section.

3.2.5.1 Solver settings

Table 3.14: Solver settings

	Iterations	Residual
Volume	10	$1 * 10^{-7}$
Pressure	2000	$1 * 10^{-6}$
Velocity	50	$1 * 10^{-7}$
Energy	100	$1 * 10^{-6}$

3.2.5.2 Turbulence and advection settings

In Barracuda the Large Eddy Simulation (LES) turbulence model was chosen with a Smagorinsky subgrid scale model.

To verify that LES is appropriate the Kolmogorov length scale has to be smaller than the grid scale [24]. Therefore, the magnitude was estimated with a quick calculation. The grid scale was estimated by taking the average volume of a cell and calculating the side length of a cube, x_{cube}, with the same volume. The average volume of a cell is $6.599 * 10^{-8} m^3$.

$$x_{cube} = \sqrt[3]{6.599 * 10^{-8} m^3} = 4.041 mm \tag{3.5}$$

The Kolmogorov length scale, η, can be computed as:

$$\eta = \left(\frac{v^3}{\epsilon} \right)^{\frac{1}{4}} \tag{3.6}$$

where v is the kinematic viscosity and the energy dissipation rate, ϵ, can be approximated as:

$$\epsilon = \frac{U^3}{L} \tag{3.7}$$

where U is a velocity and L the length scale.

The Kolmogorov length scale will be smallest with the lowest U and highest L value. For estimation the superficial velocity of the AR and FR were chosen.

The AR fluid flow is about $24^{Nm^3}/h$ through the column with a diameter of $52mm$ and the FR flow is about $12^{Nm^3}/h$ with a square with a side length of $62mm$. At normal

conditions of $1atm$ and $0°C$ the air has a density of $\rho_{air,N} = 1.276^{kg}/m^3$ [13]. The air velocity can be estimated using an air density of $\rho_{air} = 1.177^{kg}/m^3$ (see Eq. 3.2) for $1atm$ and $300K$ and the cross-sectional area A. This calculation is an estimation for the average velocity of an upward fluid stream in the reactors.

$$\dot{m}_{air} = \dot{V}_1 * \rho_1 = \dot{V}_2 * \rho_2 = u_i * A_i * \rho_i \tag{3.8}$$

$$u_{air} = \dot{V}_{air,273.15K} * \frac{\rho_{air,273.15K}}{\rho_{air,300K}} * \frac{1}{A} \tag{3.9}$$

$$u_{air,AR} = 24\frac{Nm^3}{h}\frac{1h}{3600s} * \frac{1.276\frac{kg}{m^3}}{1.177\frac{kg}{m^3}} * \frac{1}{(0.026m)^2 * \pi} = 3.403\frac{m}{s} \tag{3.10}$$

$$u_{air,FR} = 12\frac{Nm^3}{h}\frac{1h}{3600s} * \frac{1.276\frac{kg}{m^3}}{1.177\frac{kg}{m^3}} * \frac{1}{(0.062m)^2} = 0.940\frac{m}{s} \tag{3.11}$$

Assuming a large length scale as large as the FR column diameter the smallest Kolmogorov length scale computed with those values is:

$$\epsilon = \frac{(1^m/_s)^3}{0.064m} = 15.625\frac{m^2}{s^3} \tag{3.12}$$

$$\eta = \left(\frac{\left(1.844687 * 10^{-5}Pa\,s * 1.177^{kg}/m^3\right)^3}{15.625^{m^2}/s^3}\right)^{\frac{1}{4}} = 0.1253mm \tag{3.13}$$

For comparison, if both, velocity and length would be altered by a factor of 10 ($0.1^m/_s$ and $0.64m$) the Kolmogorov length scale would be $1.25mm$ and still about 3 times smaller than the grid scale. Therefore, the LES model was assumed to be appropriate for the simulation.

For advection the default settings were chosen.

Table 3.15: Turbulence and advection settings

Turbulence model	Large Eddy Simulation
C_s	0.01
Advection	Partial Donor Cell
α	0.3
β	1

where α and β are constants to calculate the weighting factor Φ. For further information and description the reader is referred to the Barracuda user manual [5].

3.2.5.3 Time controls

The time steps used for the simulation were adjusted automatically during simulation according to the CFL (Courant-Friedrichs-Lewy) number.

The CFL number is dimensionless and describes how far fluid can travel in a single time step. Barracuda computes a CFL number for each direction:

$$\text{CFL} = \frac{u\Delta t}{\Delta x_{cell}} \tag{3.14}$$

where:

u = fluid velocity in current direction

Δt = time step

Δx_{cell} = cell dimension in the current direction

Initial time step	$10^{-3}s$
Average time step	$\sim 1.6 * 10^{-4}s$
Min CFL	0.8
Max CFL	1.5

Table 3.16: Time control settings

4 Mass flow and pressure measurement

4.1 Particle mass flow measurement

The circulation rate of the bed material measured by Martinovic [52] was $823^{kg}/_h$ and is the target value for the simulation. The circulation rate of the bed material is one of the most important parameters for this thesis to rate the quality of a simulation.

The mass flow was calculated using so-called *"flux planes"* in the system. A flux planes can be set to record the total mass of particles crossing the defined plane, and therefore the particle mass flow rate can be computed based on this data. A total of nine flux planes were added with the flux planes "FLUX AR", "FLUX FR", and "FLUX ULS AR OUT" being the most important ones for calculating the global circulation rate of the particles. The global particle circulation rate in Martinovic's experiment [52] was determined by switching off the ULS to prevent further circulation, which leads to filling up the connecting pipe to the AR SEP. The time it takes until the pipe is filled to a certain height was measured and the circulation rate calculated by using the diameter, filled pipe height, bulk density and time.

Table 4.1: Flux planes list - overview

Abbreviation	Description
FLUX AR TOP	AR top part of column
FLUX ILS FR IN	Connection of FR SEP to ILS
FLUX ILS FR OUT	Connection of ILS to FR column
FLUX ULS AR OUT	Connection of ULS to FR column
FLUX ULS FR IN	Connection of ULS to FR column
FLUX AR	AR column
FLUX FR	Connection of FR column to bubbling bed
FLUX LLS AR	Connection of LLS to AR
FLUX LLS FR	Connection of FR to LLS

The flux planes listed in Table 4.1 and Table 4.2 are visualized in Figure 4.1 (without the prefix *"FLUX"*)

Table 4.2: Flux planes list - location

Abbreviation	Location [mm]		
	x	y	z
FLUX AR TOP	30 to 90	-330 to -260	1550
FLUX ILS FR IN	223 to 261	-450 to -410	1200
FLUX ILS FR OUT	265 to 305	-475 to -435	1200
FLUX ULS AR OUT	140 to 185	-200 to -155	1200
FLUX ULS FR IN	190 to 240	-205 to -160	1200
FLUX AR	38 to 96	-329 to -270	650
FLUX FR	250 to 320	-340 to -260	430
FLUX LLS AR	132 to 171	-320 to -280	103
FLUX LLS FR	183 to 222	-320 to -280	103
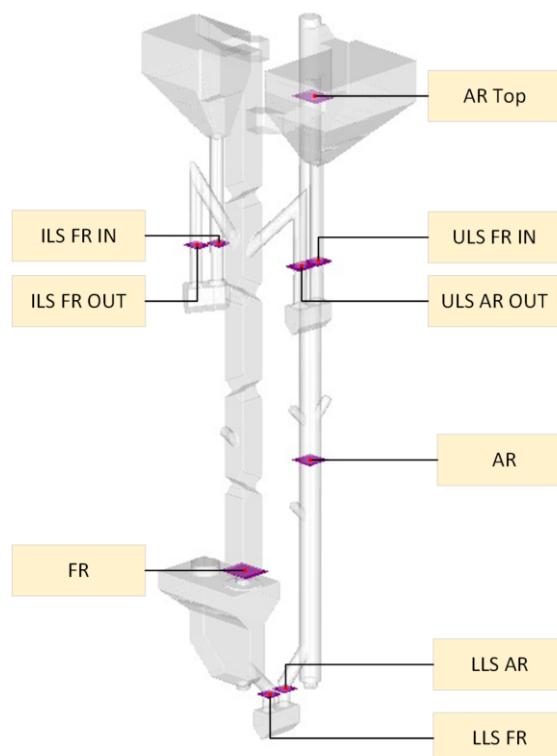
Figure 4.1: Flux planes - overview

The particle mass flow is anticipated to flow upwards in the AR, through the AR SEP to the ULS and downwards in the FR column. The particles transported out in the FR are returned via the ILS into the FR column. The particles in the FR column cross the FR junction and end up in the bubbling bed of the FR. The bubbling bed is connected to the AR with the LLS. The particle flow direction is visualized in Figure 4.2.
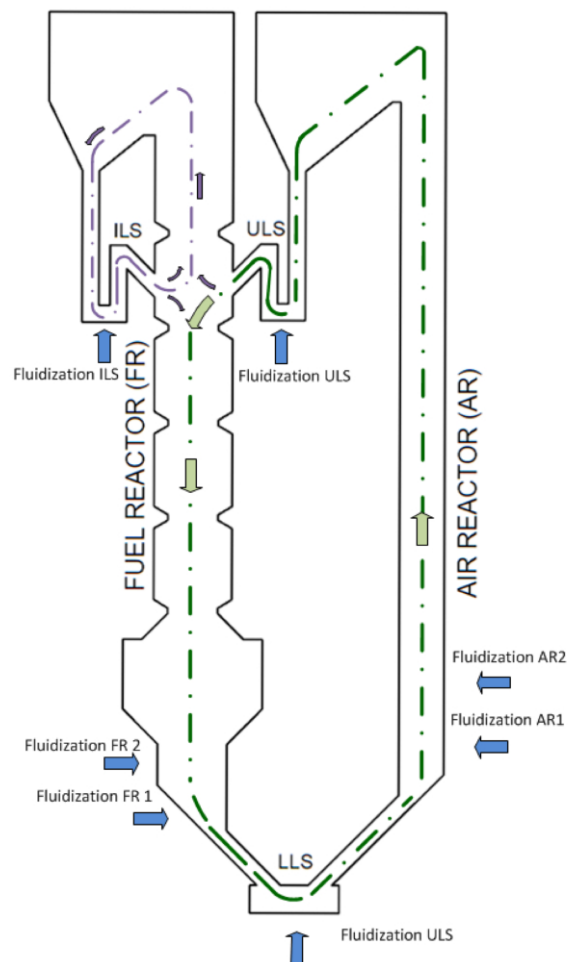
Figure 4.2: Particle mass flow direction [52]

4.2 Pressure measurement

The pressure has been recorded over time at the same height as in the physical cold-flow model in a total of 31 transient data points. The locations are listed in Table 4.5. Transient data point #23 was labeled differently in Martinovic's thesis as a fictional data point. The constant space of 53mm of the pressure sensors between the sections of the FR was necessary to compare the pressure gradients in his thesis and therefore he introduced the fictional data point, which is comparable to #22 but in theory #23 would be on the right position. Furthermore, the pressure in the free space above the bubbling bed is almost uniform and therefore the choice of data point #22 or #23 should not influence the results. Additionally, the transient data of those data points are congruent and therefore identical for evaluation.

Table 4.4: Transient data points - FR

Num#	z [mm]	Location
1	40	LLS
19	117	LLS
20	170	FR
21	301	FR
22	383	FR
23	389	FR
25	442	FR
26	625	FR
27	678	FR
30	865	FR
31	918	FR
32	1105	FR
33	1158	FR
36	1345	FR
37	1398	FR
40	1616	FR
41	1722	FR

Table 4.3: Transient data points - AR

Num#	z [mm]	Location
1	40	LLS
2	117	LLS
4	228	AR
5	389	AR
6	532	AR
7	772	AR
8	1151	AR
9	1599	AR
10	1748	AR

The transient data points listed in Table 4.3 and Table 4.4 are visualized in Figure 4.3 (scale is given as reference in meters). A complete list of all transient data points, including points not used for evaluation, are listed in Table 4.5.
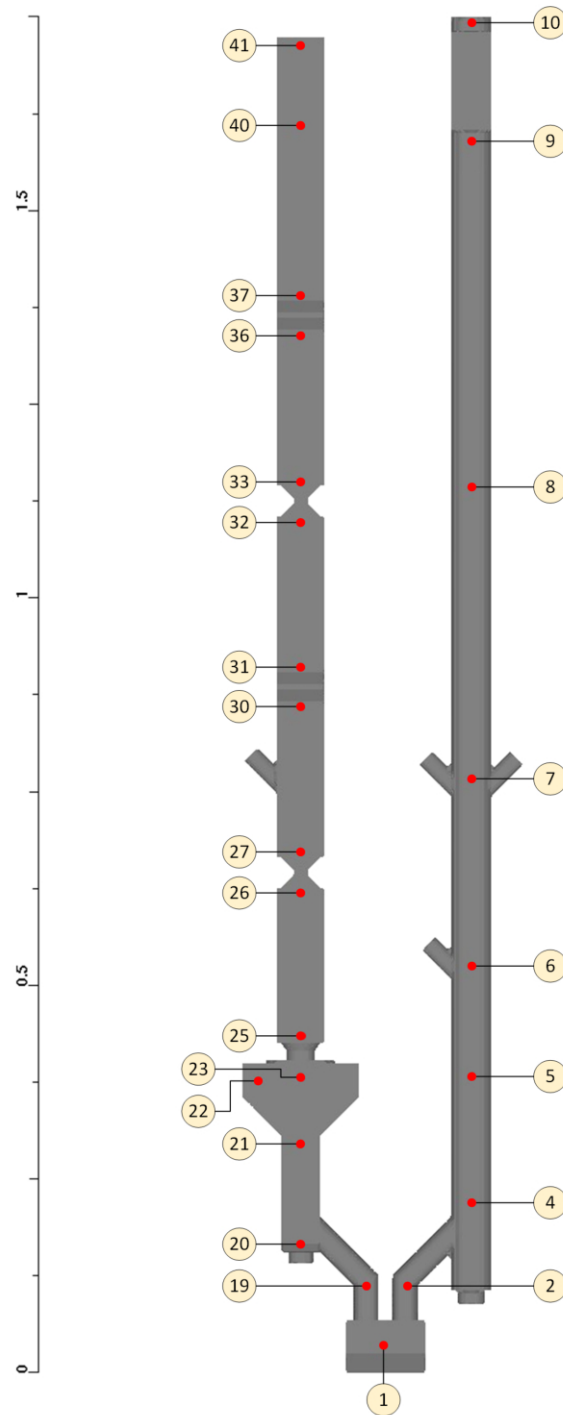
Figure 4.3: Transient data points - overview

Table 4.5: Transient data points - overview

Num#	x [mm]	y [mm]	z [mm]	Location
1	177	-300	40	LLS
2	202	-300	117	LLS
4	67	-300	228	AR
5	67	-300	389	AR
6	67	-300	532	AR
7	67	-300	772	AR
8	67	-300	1151	AR
9	67	-300	1599	AR
10	67	-300	1748	AR
11	166	-179	1437	AR SEP
12	166	-179	1142	ULS
13	216	-184	1142	ULS
19	152	-300	117	LLS
20	287	-300	170	FR
21	287	-300	301	FR
22	342	-300	383	FR
23	287	-300	389	FR
25	287	-300	442	FR
26	287	-300	625	FR
27	287	-300	678	FR
30	287	-300	865	FR
31	287	-300	918	FR
32	287	-300	1105	FR
33	287	-300	1158	FR
36	287	-300	1345	FR
37	287	-300	1398	FR
40	287	-300	1616	FR
41	287	-300	1722	FR
42	243	-431	1458	FR SEP
43	287	-455	1142	ILS
44	243	-431	1142	ILS

4.3 Data evaluation

4.3.1 Visual observation

The simulation data was rendered into an animation in Barracuda in order that the fluid dynamical behavior can be observed qualitatively. The color in the snapshots of the animation (e.g. Figure 5.1) indicates the particle volume fraction ranging from red (a close-packed bed where $\varepsilon_p \approx \varepsilon_{cp}$) to blue (a diluted system where $\varepsilon_p \rightarrow 0$).

4.3.2 Mass flow rate

How flux planes were used to determine the total mass of particles travelling through a defined plane in the simulation and how Martinovic measured the particle circulation rate in his thesis [52] was explained in Section 4.1. The AR mass flow rate was defined as the particle circulation rate in this work. The mass flow rates were calculated from the total mass crossing the flux planes in a certain time. The flux planes for the AR, the FR and ULS mass flow rate are listed in Table 4.6.

Table 4.6: Flux planes for mass flow rate

mass flow rate	flux plane
AR	FLUX AR
FR	FLUX FR
ULS	FLUX ULS AR OUT

Those values are also plotted in the mass flow rate graphs. The evaluation of the mass flow rates and the resulting mass differences in different sections of the model was done by comparing them with each other and with other simulations. If the mass flow rates differ from each other the mass difference will increase over time. The simulation will be steady if the mass difference is constant. For example, Figure 4.4 shows an increasing mass difference of an unstable simulation.
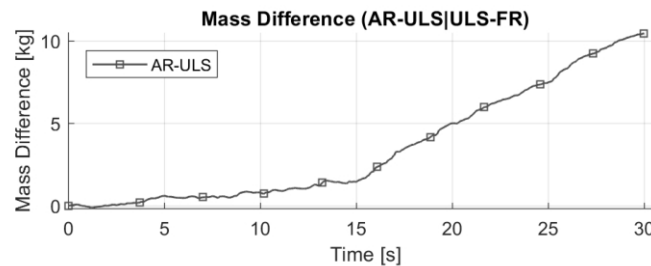
Figure 4.4: Mass difference - unstable example

4.3.3 Pressure profile

The pressure profiles were created from averaging the pressure data of the transient data points. The transient pressure profiles were generated using a moving average of 5 000 time steps for better visualization (see Figure 4.5) because of the large data set and small time steps ($\sim 1.6 * 10^{-4}\,s$).

   The pressure over height profiles were generated by the calculating arithmetic mean values over all time steps in-between the starting time and end time step. The pressure over height profile was plotted for the AR and FR (see Figure 4.6). A flat slope indicates a high pressure drop and therefore many particles.

(a) moving average of 5 time steps   (b) moving average of 5000 time steps
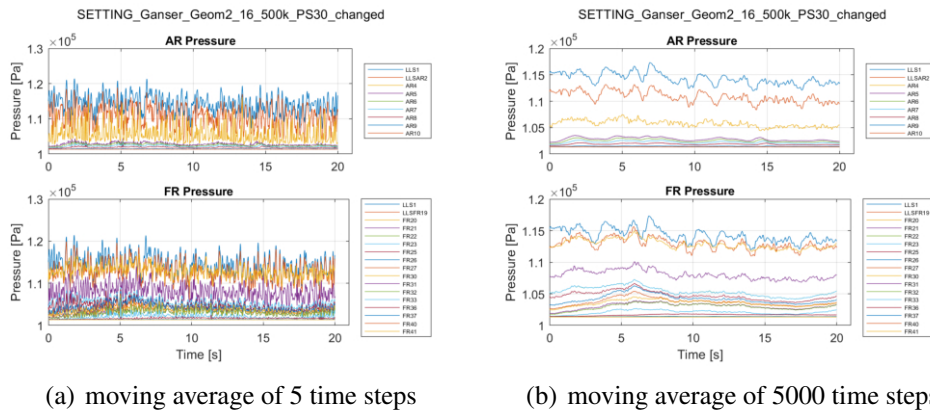
Figure 4.5: Moving average - transient data plot
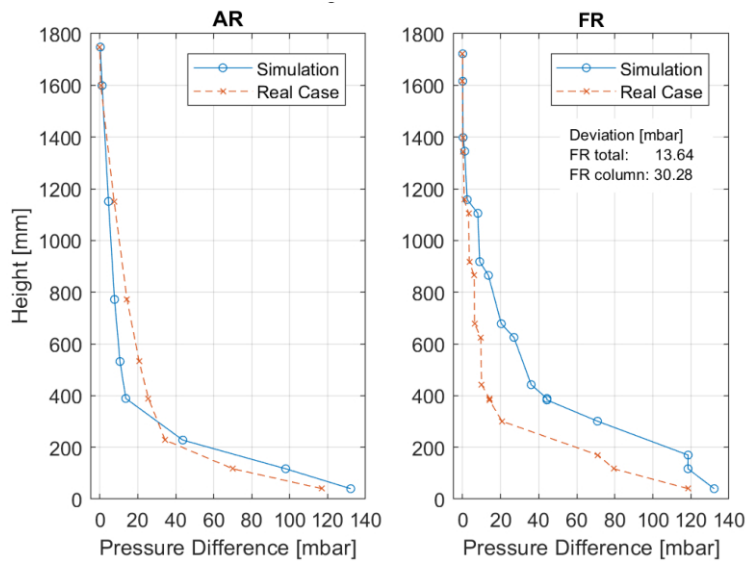
Figure 4.6: Example of a pressure profile

4.3.4 Pressure gradient

The pressure gradient at height H_i (see Figure 4.7), the middle between two measuring points, is calculated by dividing the pressure difference by distance difference [52]. The arithmetic mean value, which was determined for the pressure profile, was used for calculation.

$$\frac{\partial p(H)}{\partial H}\bigg|_{H=H_i} = p'(H_i) \cong \frac{p(H_{n+1}) - p(H_n)}{H_{n+1} - H_n} \tag{4.1}$$

$$H_i = H_n + \frac{H_{n+1} - H_n}{2} \tag{4.2}$$

A large pressure gradient indicates high pressure drops and therefore more particles in the investigated section. The pressure gradient was only calculated for the FR (see Figure 4.8).
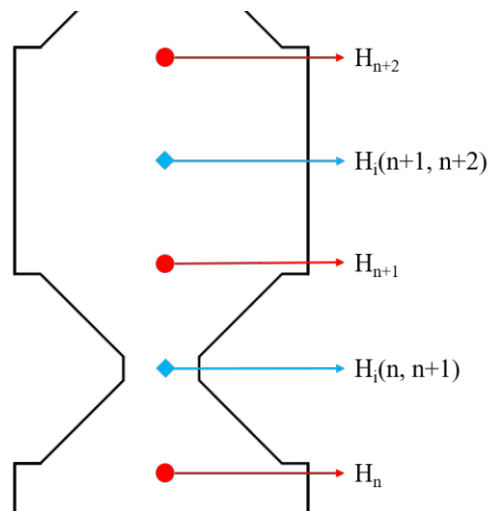
Figure 4.7: H_i used for pressure gradient calculation
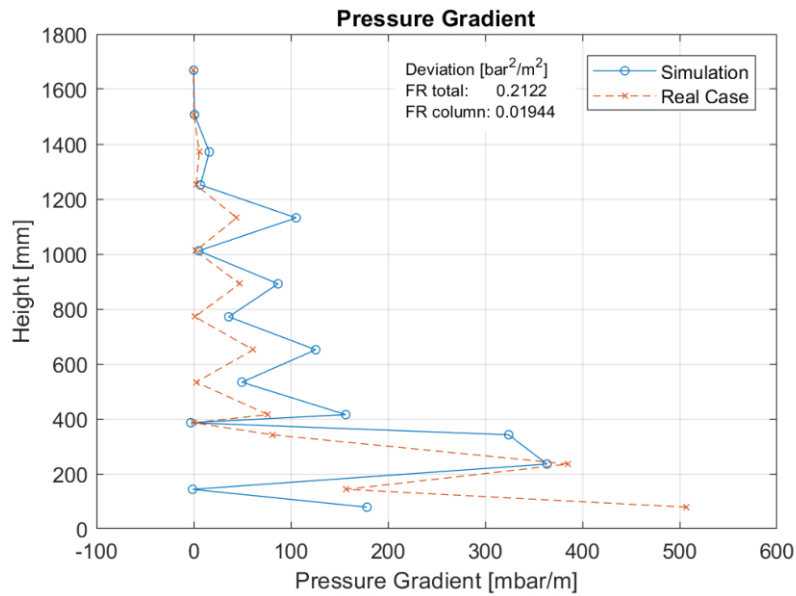
Figure 4.8: Example of a pressure gradient plot

4.3.5 Pressure parameters

To quantify and rate the quality of the simulation of the pressure in the FR column two parameters are introduced, one for the pressure profile and one for the pressure gradient. The parameters are displayed in the respective pressure plots labeled as *"Deviation"* of the *"FR Column"*.

4.3.5.1 Pressure profile parameter

The pressure profile parameter was used to display the deviation of the pressure in the FR column and therefore taking to account the total amount of particles in the column and rating its total mass in the column. This value is calculated by taking the absolute pressure difference of the simulation and the real measurements of the cold flow model at the transient pressure data point or, respectively, the pressure measuring point #22 at a height of $383mm$.

$$P_{PP} = p_{Simulation} - p_{RealCase} \qquad (4.3)$$
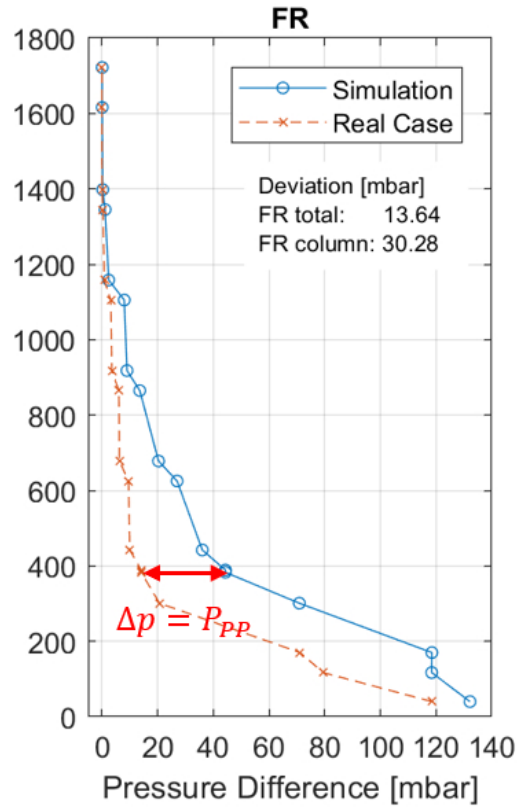
Figure 4.9: Pressure difference in FR column - P_{PP}

4.3.5.2 Pressure gradient parameter

The pressure gradient was quantified and rated by using a sum over the squared deviation of the pressure gradient from the real case. Therefore, a big deviation has a bigger impact on the parameter. Compared to the pressure profile parameter, it rates the distribution of the particles rather than the total amount. The summation started at the bottom of the FR column and was finished at the top, therefore taking pressure measuring points #22, #23, #25, #26, #27, #30, #31, #32, #33, #36, #37, #40, and #41 into account for calculation. The parameter over the whole FR section was calculated using all relevant pressure measuring points and can be found in the corresponding graphs but was not used to evaluate the quality of the simulation.

$$P_{PG} = \sum_i \left(|p'(H_i)_{Simulation} - p'(H_i)_{RealCase}|^2 \right) \tag{4.4}$$

5 Simulations

A broad spectrum of different settings and combinations were tested in the conducted simulations. The simulations were improved step-by-step and rated based on their performance. The varied parameters in this chapter are the drag law, P_S value for the particle normal stress, geometry and fluidization rates.

5.1 Mesh sensitivity

Simulations in this section: G6, G7, G8, G14, G19 according to Table 3.2

The grid used in the simulation must be fine enough in order that the mesh size itself does not significantly influence the simulation results. However, a finer mesh requires more computing time for calculations. The mesh sensitivity analysis was performed using settings for a stable simulation, in this particular case the P_S value was set to $50Pa$. The influence of the mesh has been studied by varying the total amount of cells resulting in the respective real cell numbers listed in Table 3.4. Based on the pressure and mass flow data compared to each preceding simulation the mesh size was refined until only small deviations occurred in the following simulation. Good and stable results were achieved after refining the grid to around $500k$ real cells.

5.1.1 Evaluation

The evaluation of the different cell numbers was done by quantifying the AR, FR, and ULS mass flow, the pressure profile and gradient, and qualitatively by visual observations and reviewing the graphs of each simulation. The graphs of each simulation are attached in the appendix (Figure A.4 to Figure A.7).

The mass flow, pressure profile, and pressure gradient were averaged between $20s$ and $30s$ (except simulation with $80k$ averaging between $10s$ to $15s$). The snapshots of the animated simulation results are displayed at time step $30s$ (respectively $15s$), the end of the simulation (see Figure 5.3). The end of the simulation was either a steady state condition or when flooding in some part of the model occurred.

5.1.2 Settings

The mesh sensitivity was tested by using settings listed in Table 5.1. Initial conditions from the simulation *G23* at 60*s*, which had similar settings, were used to initialize the particle distribution and fluid conditions. The initial state is displayed by using the initial state of the simulation with about 500*k* real cells as depicted in Figure 5.1 and Figure 5.2. The total amount of numerical particles was intentionally the same throughout the mesh sensitivity simulations despite different mesh resolutions.

Table 5.1: Mesh sensitivity settings - overview

Setting	Value
Drag Law	Ganser
FR column gap space	16*mm*
P_S constant for particle normal stress	50*Pa*
Approximate real cell number	80*k* 150*k* 300*k* 400*k* 500*k*
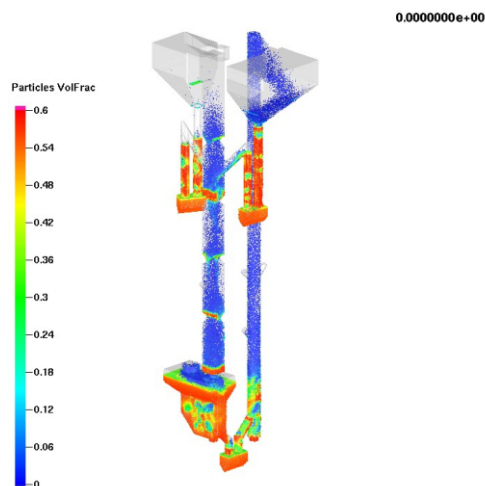
Figure 5.1: Mesh sensitivity - particle IC

(a) Pressure profile   (b) Pressure gradient
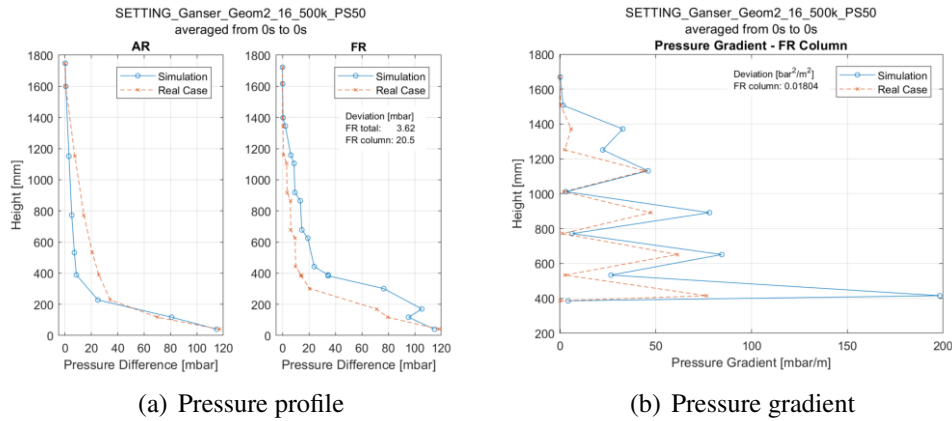
Figure 5.2: Mesh sensitivity - pressure IC

5.1.3 Mesh sensitivity - 80k cells

Simulations in this section: G19 according to Table 3.2

In the simulation with $80k$ cells the FR column and AR SEP did flood during the simulation and as a result the lower part of the FR started to drain and did not reach a steady state. This behavior is displayed in Figure A.4a and Figure A.4b indicated by the increasing mass difference of the total mass passing the AR and ULS flux planes and the resulting lower mass flows in the FR and ULS sections compared to the AR mass flow.

5.1.4 Mesh sensitivity - 150k cells

Simulations in this section: G6 according to Table 3.2

The simulation with $150k$ showed a similar behavior as the one with $80k$ but slightly improved. Nevertheless, the FR column and AR SEP did also flood.

5.1.5 Mesh sensitivity - 300k cells

Simulations in this section: G7 according to Table 3.2

The simulation with $300k$ showed signs of flooding of the FR column and AR SEP because of the increasing mass differences (see Figure A.6a) but a much more improved performance compared to simulations with $80k$ and $150k$ cells.

5.1.6 Mesh sensitivity - 400k cells

Simulations in this section: G8 according to Table 3.2

The simulation with $400k$ reached a steady state behavior, which was indicated by the stable pressure history (see Figure A.2) and very similar mass flows, which lead to a constant mass difference and also the visual observation did not show signs of flooding in any part of the model.

5.1.7 Mesh sensitivity - 500k cells

Simulations in this section: G14 according to Table 3.2

The simulation with $500k$ was very similar to the one with $400k$, both in mass flow and pressure parameters and the therefore no further cell size reduction was performed.

5.1.8 Mesh sensitivity conclusion

The results of the mesh sensitivity analysis are visualized in Figure 5.4 and the exact values are in Table A.1 attached in the appendix.

The simulations with $80k$, $150k$, and $300k$ were not stable simulations, indicated by their pressure history, mass flow rates and visual observation. The simulation with $400k$ and $500k$ cells do have a mass flow difference between the AR, ULS and FR mass flow. Those differences occur because of the fluctuating particle flow in the FR column. The particles partially accumulate and drop down through the column. Therefore, the FR mass flow rate depends heavily on the averaging time period, but the stable mass difference indicates, that the overall mass flow of the FR is the same as the AR and ULS.

Therefore, the AR mass flow was chosen to indicate the particle circulation and the FR and ULS mass flow only do have a secondary role in a stable simulation. The results are visualized in Figure 5.4. Averaging of the mass flow and pressure parameters was done from $20s$ to $30s$. The simulation with $80k$ was averaged between $10s$ to $15s$ because flooding occurred very early and the state of interest is the circulating and not the flooded state. This state was also visible in the visual observation and is indicated by Figure A.2s.

(a) Mesh size $80k$ at $15s$

(b) Mesh size $80k$ at $30s$

(c) Mesh size $150k$ at $30s$

(d) Mesh size $300k$ at $30s$

(e) Mesh size $400k$ at $30s$

(f) Mesh size $500k$ at $30s$
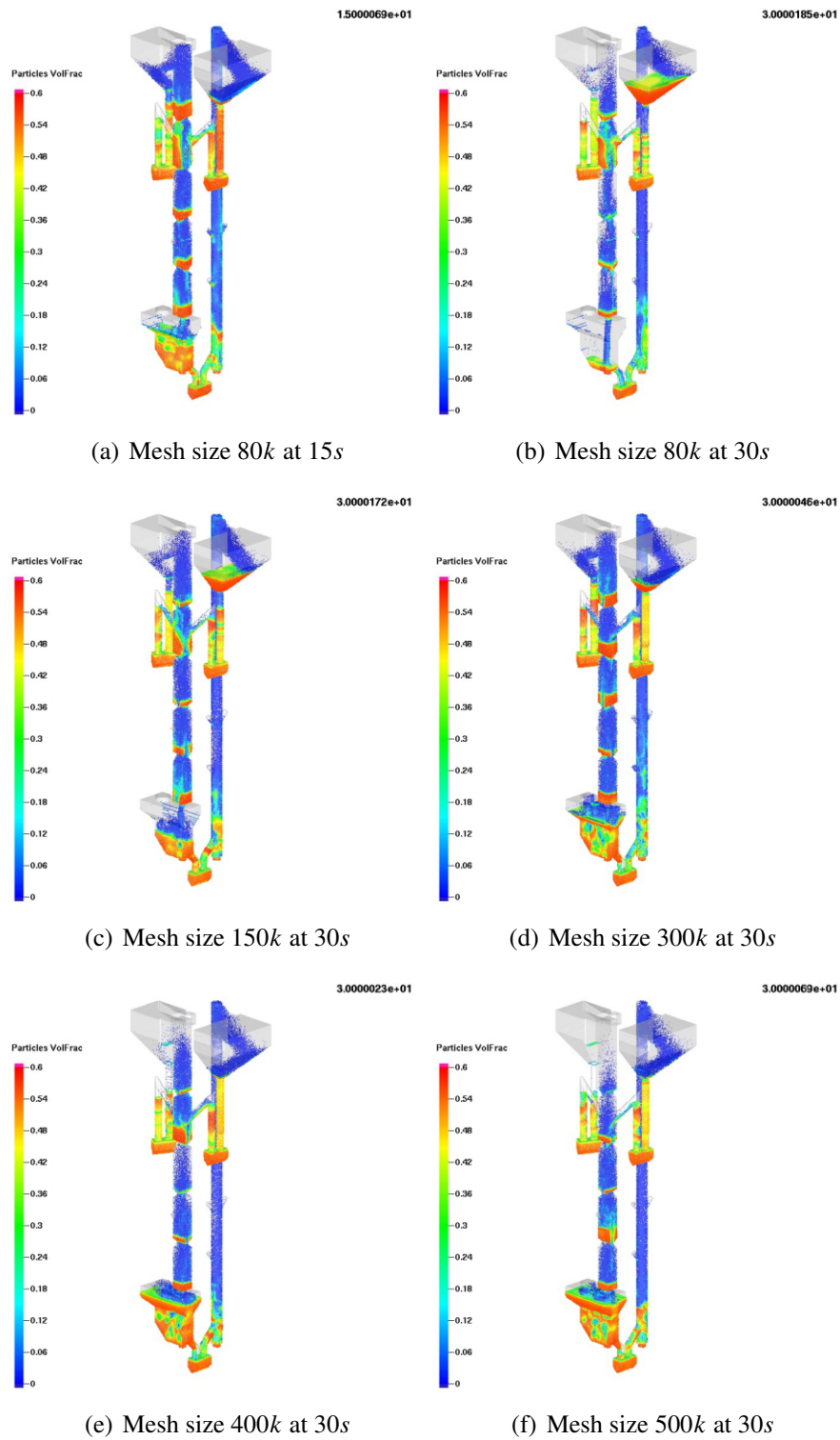
Figure 5.3: Mesh sensitivity - overview
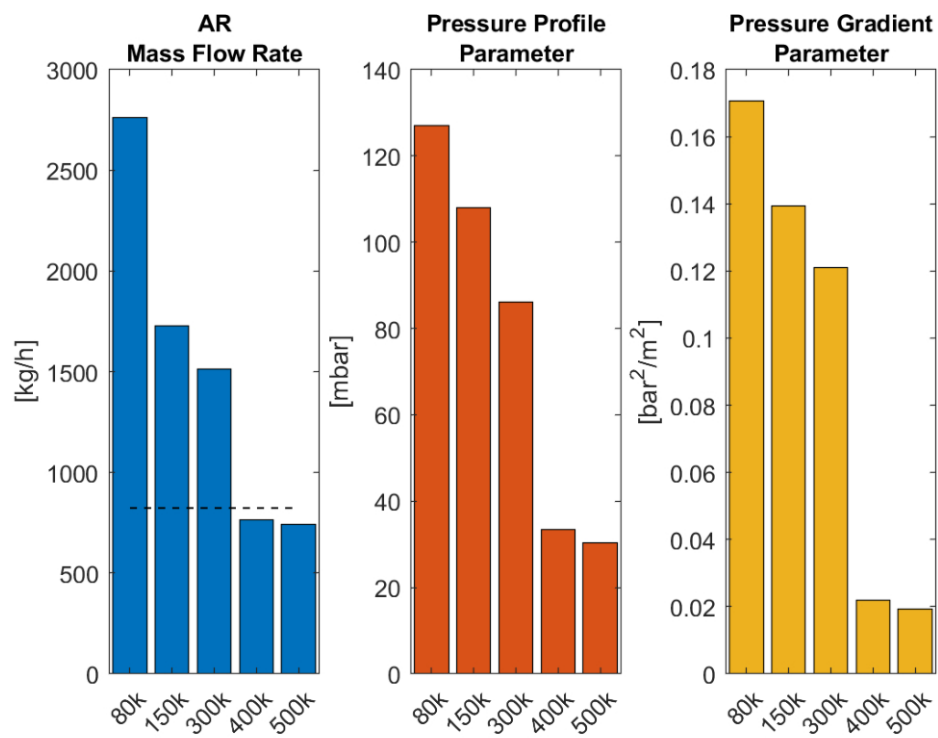
Figure 5.4: Mesh sensitivity result comparison

Based on the investigation in this chapter one can state:

A mesh with 500k real cells is appropriate for the simulations

5.2 u_{mf} and fluidization

In advance of Section 5.3.3 the fluidization of the bed material will be discussed with different P_S values. Simulation *G9* of Section 5.3.3 with $P_S = 30$ seemed promising but the bed material circulation rate was too small compared to the target value. The circulation rate will be smaller if the fluidization of the LLS is not sufficient. Therefore, the fluidization of the particles and consequently the fluidization of the loop seal were investigated in this section. The potential to improve the overall performance of the simulation by modifying the loop seal fluidization rate is discussed in Section 5.3.4. At the beginning the minimum fluidization velocity, u_{mf}, was evaluated and subsequently if fluidization is guaranteed in the loop seals.

5.2.1 Minimum fluidization velocity

The u_{mf} was determined in a simulation and compared to the values calculated by Martincovic [52]. The u_{mf} in the simulation turned out to be higher than the value mentioned by Martinovic.

5.2.1.1 Setup for u_{mf}

The u_{mf} was measured using a cuboid, designed with Autodesk, with a square base and a side length of $150mm$, and a height of $800mm$. The cuboid was filled $80mm$ with close-packed bronze bed material. The superficial velocity was varied between $0\frac{m}{s}$ to $0.15\frac{m}{s}$. The expected pressure drop was $4kPa$ as described by Eq. 5.1.

$$
\begin{aligned}
\Delta p &= \rho_{p,bulk} * h_{\text{umf box}} * g \\
&= 5100\frac{kg}{m^3} * 0.08m * 9.81\frac{m}{s^2} \\
&= 4002.5 Pa
\end{aligned}
\tag{5.1}
$$
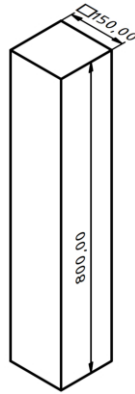
Figure 5.5: Minimum fluidization - geometry

The boundary conditions consisted of a flow boundary with a defined superficial velocity at the bottom and a pressure boundary at the top. The flow was incrementally reduced, starting with a high velocity for high fluidization. The pressure drop over the bed was calculated. The pressure was recorded close to the inlet and outlet by applying transient data points in the middle of the cross-section and the pressure difference over the bed as a function of the superficial velocity was plotted.

The velocity was always kept constant for $10s$. The first $5s$ were the time for the system to reach fluidization at its respective velocity and the following $5s$ were used to obtain an averaged pressure value. The total simulation time was $430s$ with a superficial velocity gradually being reduced from $0.15^m/_s$ to $0^m/_s$. The simulation was conducted with the three different drag laws and varied P_S values.

The u_{mf} and its profile were slightly dependent on the P_S value but heavily influenced by the different drag laws applied. The plots of the simulations are attached in the appendix (Figure A.8 to Figure A.10) and an overview of the calculated u_{mf} values is given in Table 5.2.

Table 5.2: u_{mf} from simulation

Drag Law	Ganser			WYE		EMMS	
$P_S\,[Pa]$	1	30	50	1	30	1	30
$u_{mf}\,\left[\frac{m}{s}\right]$	0.042	0.039	0.037	0.033	0.027	0.017	0.017

Martinovic calculated a u_{mf} of $0.022^m/_s$, using dimensionless numbers [52].

Based on the investigation in this chapter one can state:

The u_{mf} value differs significantly in simulations with the Ganser or WYE drag law from the actual value.

5.2.1.2 Estimation for fluidization in loop seals

To estimate if the loop seals are fluidized sufficiently the section with the lowest fluidization rate will be inspected. The lowest fluidization rate will be achieved at the smallest superficial velocity. The superficial velocity in the loop seal was calculated based on the set air mass flow and the cross-sectional area of the loop seal. The superficial velocity will be the smallest at the largest cross-sectional area. The largest cross-sectional area is the rectangular area of the loop seal as depicted in Figure 5.6 with an area of $A = 0.005304m^2$ with given dimensions.
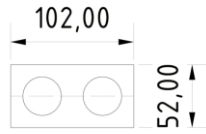
Figure 5.6: Loop seal - top view

The velocity was calculated with the properties listed in Table 5.3.

Table 5.3: Loop seal fluidization estimation - air properties

$$\rho_{air,N} = 1.276\frac{kg}{m^3} \quad \Big| \quad \rho_{air} = 1.177\frac{kg}{m^3} \quad \Big| \quad \dot{V}_{normal} = 0.8\frac{Nm^3}{h} \quad \Big| \quad \dot{V}_{changed} = 1.4\frac{Nm^3}{h}$$

where:

$\rho_{air,N}$	=	air density at $101325Pa$ and $273.15K$
ρ_{air}	=	air density at $101325Pa$ and $300K$
$\dot{V}_{normal}$	=	air volume flow with normal fluidization rate
$\dot{V}_{changed}$	=	air volume flow with increased fluidization rate

$$u_{normal} = \frac{\dot{V}_{normal}}{A} = \frac{0.8\frac{Nm^3}{h} * \frac{1h}{3600s} * \frac{1.276\frac{kg}{m^3}}{1.177\frac{kg}{m^3}}}{0.005304m^2} = 0.04542\frac{m}{s} \tag{5.2}$$

The u_{mf} value obtained from simulation in Figure A.8a is $0.039^{m}/_{s}$, which is about 1.77 times bigger than the mentioned u_{mf} of $0.022^{m}/_{s}$ in Martinovic's Thesis [52].

The fluidization rate in the ULS and LLS in the real case is $0.8^{Nm^3}/_h$. This is equal to a superficial velocity of $0.045^{m}/_{s}$ (see Eq. 5.2), assuming a constant distribution over its area. Eq. 5.2 indicates that the fluidization rate in the loop seal is close to the u_{mf} value of the simulations with Ganser and WYE, and therefore eventually will not be fluidized in all sections of the loop seal in those simulations.

Therefore, an approach of increasing the fluidization rate in the loop seal was used by increasing the value from $0.8^{Nm^3/h}$ to $1.4^{Nm^3/h}$, which is equal to a rise of 75%, the approximate increase of the u_{mf} in the simulation of Figure A.8a. This results in a superficial velocity of $0.07949^{m/s}$ as described in Eq. 5.3. The air flow and respective velocities of the normal case, a case with air flow increased by 1.75 and one increased by 2.5 are listed in Table 5.4.

$$u_{changed} = \frac{\dot{V}_{changed}}{A} = \frac{1.4\frac{Nm^3}{h} * \frac{1h}{3600s} * \frac{1.276\frac{kg}{m^3}}{1.177\frac{kg}{m^3}}}{0.005304m^2} = 0.07949\frac{m}{s} \qquad (5.3)$$

Table 5.4: Fluidization rate alteration - overview

Loop Seal	Air Injection [Nm^3/h]			Superficial Velocity [m/s]		
	normal	increased by 1.75	increased by 2.5	normal	increased by 1.75	increased by 2.5
ULS	0.80	1.40	2.0	0.04542	0.07949	0.11355
LLS	0.80	1.40	2.0	0.04542	0.07949	0.11355
ILS	0.60	1.05	1.5	0.03407	0.05962	0.08516

5.3 Finding the best case

Simulations in this section: E1, G2, G3, W1, W2 according to Table 3.2

The best fit compared to the real cold flow model was found by a step-by-step approach. The drag law, P_S, geometry, and fluidization rates were varied. Because of the mesh sensitivity concluding that a mesh size of $500k$ is sufficient, only simulations with this mesh size will be taken in regard, except three simulations designated to compare the drag laws, to indicate trends and characteristics.

5.3.1 Choosing the drag law

This section is focusing on to find the appropriate drag model for the simulations by testing the EMMS, Ganser, and WYE drag law. The drag law had a substantial influence on the simulation. The appropriate drag law was determined by conducting various simulations. First, three simulations, only differing in the drag law, with $300k$ cells were realized. Based on those results two of those laws were investigated with a finer mesh of $500k$ cells. The results in the mesh sensitivity analysis verified that the mesh resolution is sufficient with $500k$ real cells (see Section 5.1). In the last step the different drag laws were compared with each other using an improved case to verify the choice of the drag law (see Section 5.3.4.2).

The initial particle distribution of the $300k$ and the $500k$ simulation varied, but the simulation with the same cell number only differed by the drag law. Because of the poor performance of the EMMS drag law with $300k$, it was not conducted again with the same settings and $500k$ cells but only with improved settings as already mentioned for comparison.

5.3.1.1 300k simulation

Simulations in this section: E1, G2, W1 according to Table 3.2

The simulations in this section were initialized with particle initial conditions as pictured in Figure 3.8b.

Snapshots of the simulation with different drag laws are depicted in Figure 5.7.

(a) EMMS

(b) Ganser

(c) WYE
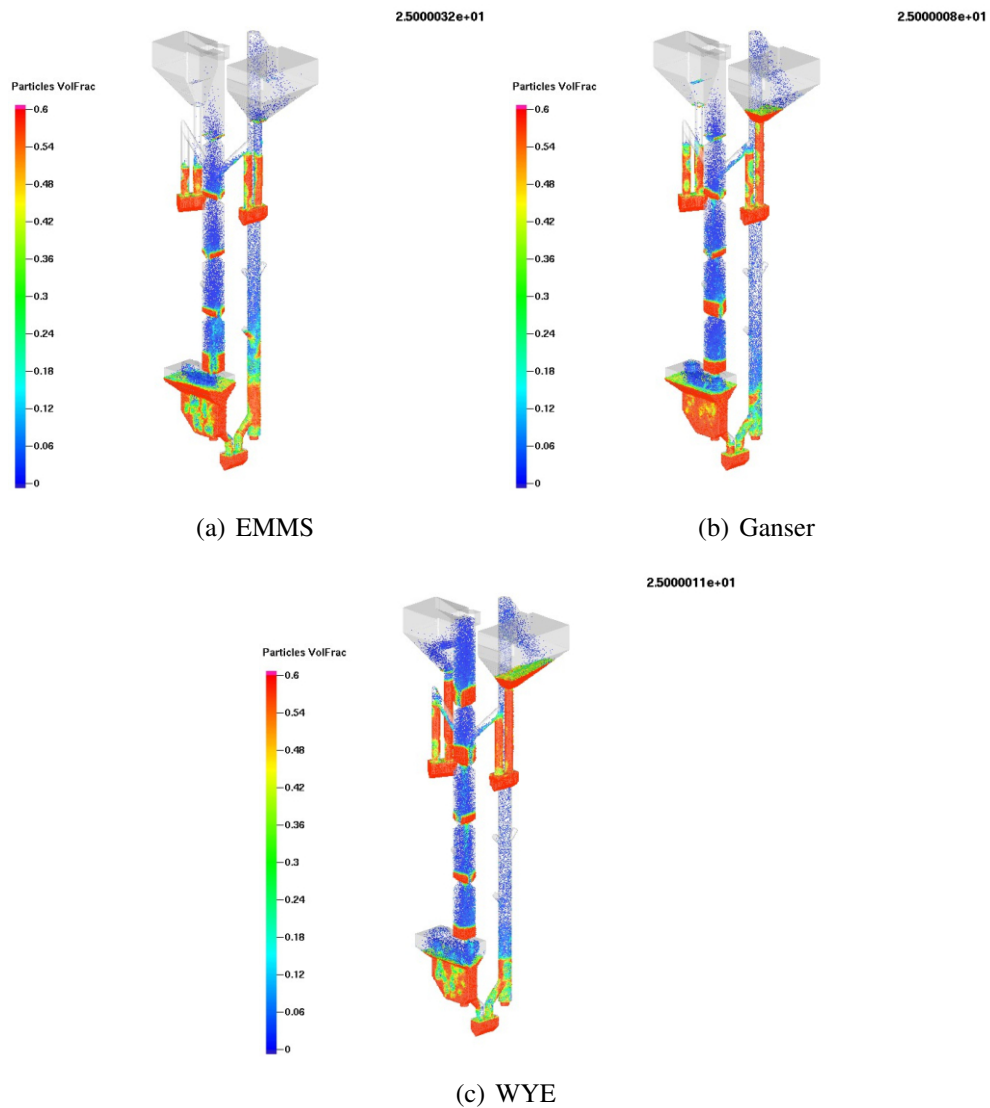
Figure 5.7: Snapshots at 25*s* with different drag laws - 300k

EMMS

Simulations in this section: E1 according to Table 3.2

The EMMS drag law results in the simulation showed very small AR and ULS mass flow rates. The pressure profile in the AR reactor seems to be very accurate in most parts of the column, but as the pressure gradients suggest the distribution in the column is off. Therefore, it seems that the EMMS drag law is not appropriate for further simulations, but was tested with improved settings in Section 5.3.4.2.

(a) Mass difference

(b) Total mass

(c) Pressure profile

(d) Pressure gradient
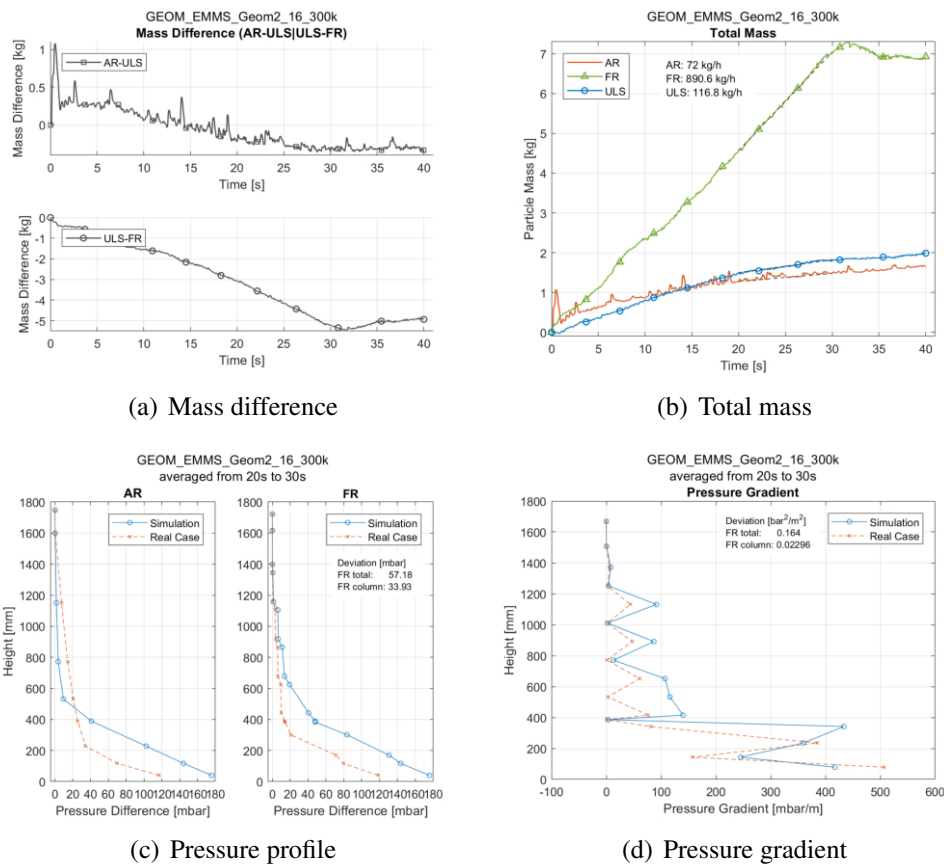
Figure 5.8: Simulation 300k EMMS - *E1*

Ganser

Simulations in this section: G2 according to Table 3.2

The results of the simulation with the Ganser drag law showed converging particle mass flow rates in the AR, FR, and ULS and a stable FR column. No increasing trend of particle mass difference in the FR column and AR SEP can be witnessed and the particle distribution seems promising.

(a) Mass difference

(b) Total mass

(c) Pressure profile

(d) Pressure gradient
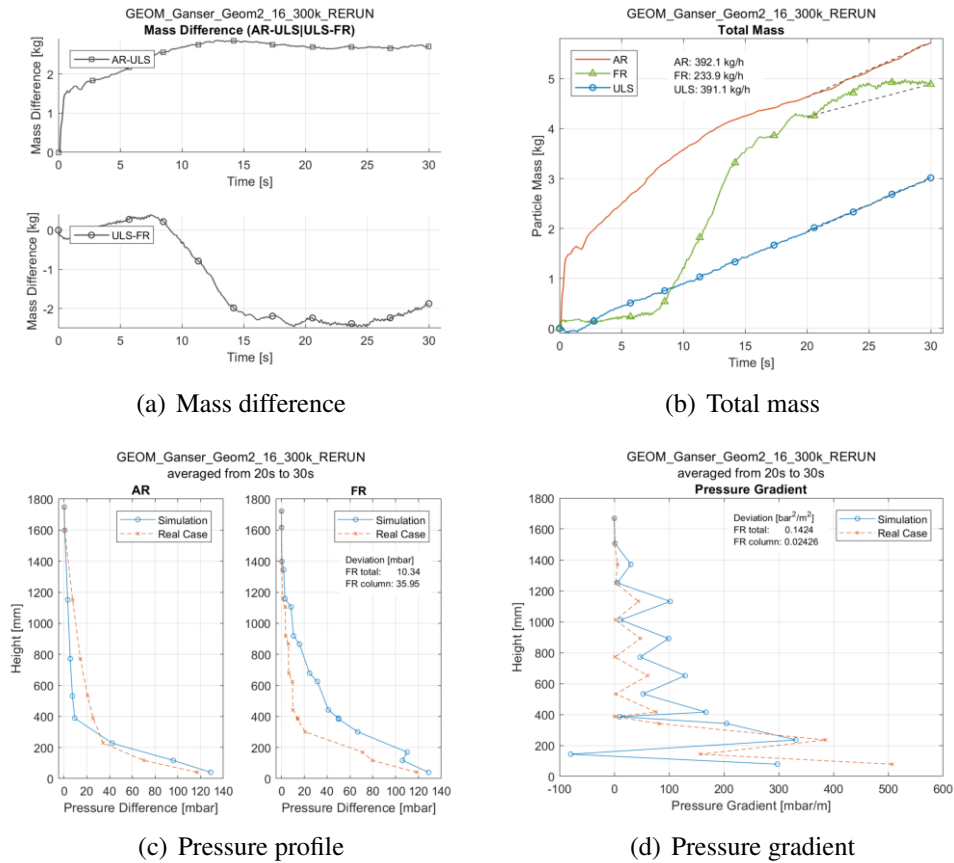
Figure 5.9: Simulation 300k Ganser - *G2*

WYE

Simulations in this section: W1 according to Table 3.2

The simulation with WYE resulted in a bigger mass flow compared to the simulation with Ganser but also flooding of the AR SEP occurred, which can be seen in Figure 5.10 and by visual observation (see Figure 5.7a). Furthermore, the column was filled with more bed material resulting in worse pressure parameters, compared to the simulation with Ganser, but the mass flow of the FR column is steady. The particle mass difference of the FR and ULS in Figure 5.10a shows a prompt increase of particles in the FR an after 15*s* a continuous decrease. At this time, it is inconclusive if the negative trend would continue but overall the mass flows in the system are not steady.

(a) Mass difference   (b) Total mass

(c) Pressure profile   (d) Pressure gradient
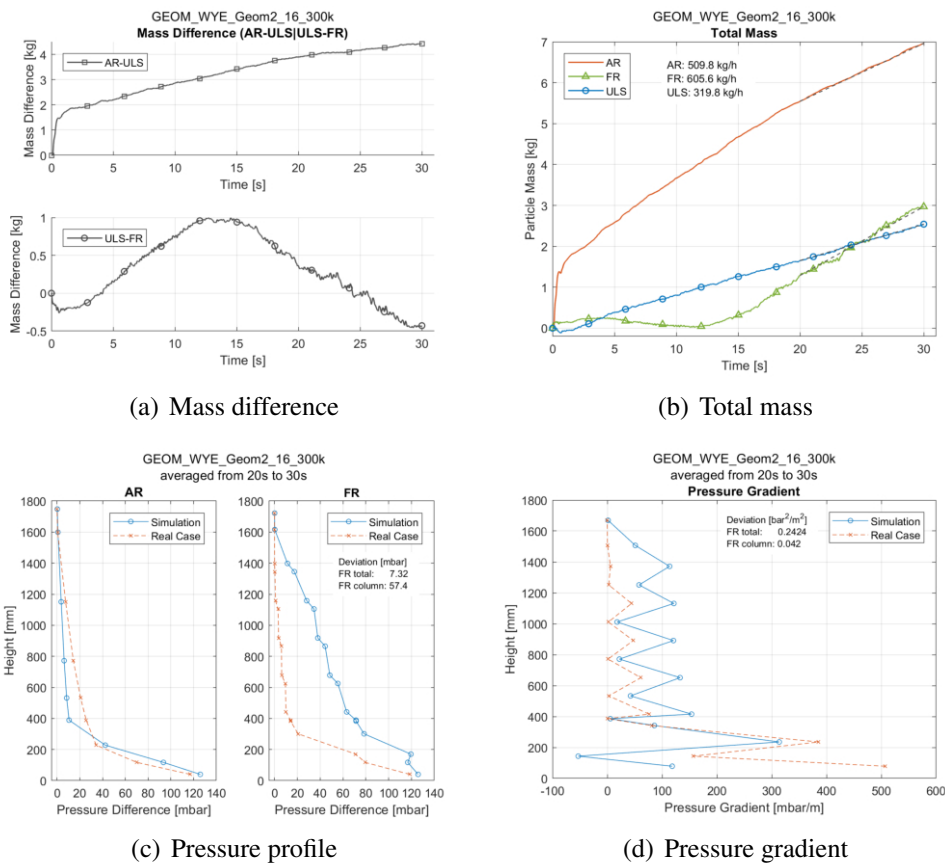
Figure 5.10: Simulation 300k WYE - *W1*

Conclusion of 300k simulation

The results of the simulation with $300k$ real cells are visualized in Figure 5.11 and the exact values are in Table A.2 attached in the appendix.
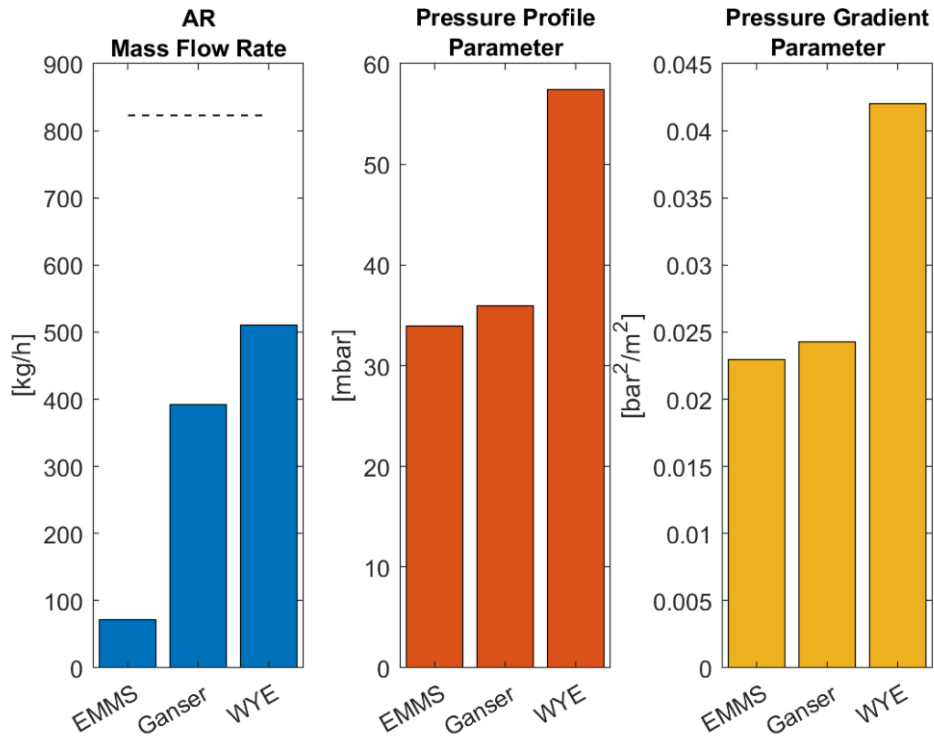
Figure 5.11: Drag law (300k) - result comparison

The conclusion of the $300k$ simulation was that both Ganser and WYE are promising options and EMMS is expected to produce poor results in this setup. Simulations with Ganser produced better results in the FR column, which are essential for the particle distribution while those with WYE already produced a decent mass flow but with faster flooding and worse distribution in the FR column. Therefore, Ganser and WYE were tested with a finer mesh again.

5.3.1.2 500k simulation

Simulations in this section: G3, W2 according to Table 3.2

The Ganser and WYE drag laws were tested with a mesh of $500k$ real cells and with an initial particle distribution as depicted in Figure 3.8a.

The $500k$ simulations were monitored in their progress according to the total mass flow and if necessary their simulation time increased to reach a steady state. The simulation with Ganser was run for a total of $60s$ because it was also used for comparison in Section *"P_S set to 1"* and therefore continued for additional $20s$. The simulation with WYE was run for $40s$ and the parameters were compared at time step $40s$.

(a) Ganser at $40s$ (b) WYE at $40s$
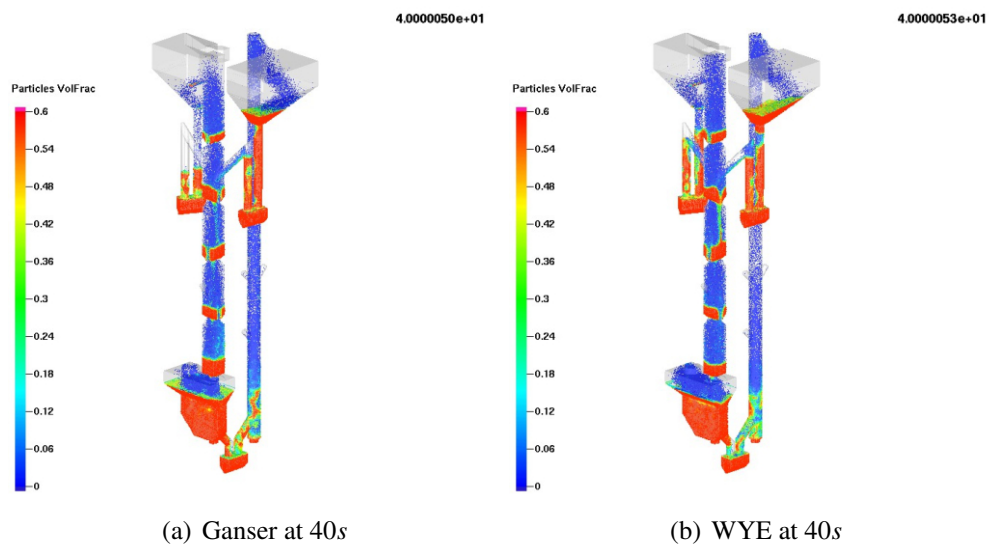
Figure 5.12: Snapshots at $40s$ with different drag laws - 500k

Ganser

Simulations in this section: G3 according to Table 3.2

The simulation with Ganser has a steady FR column after 30*s*. After 10*s* the mass flow rates in the system seemed to be steady but started to fluctuate at time step 20*s* again. Overall the simulation is not steady due to a low mass flow rate in the ULS, which leads consequently to flooding of the AR SEP, but indicated a stable FR column. Furthermore, the upper part of the column is clearly overfilled with particles, also indicated in the pressure gradient diagram.

(a) Mass difference

(b) Total mass

(c) Pressure profile

(d) Pressure gradient
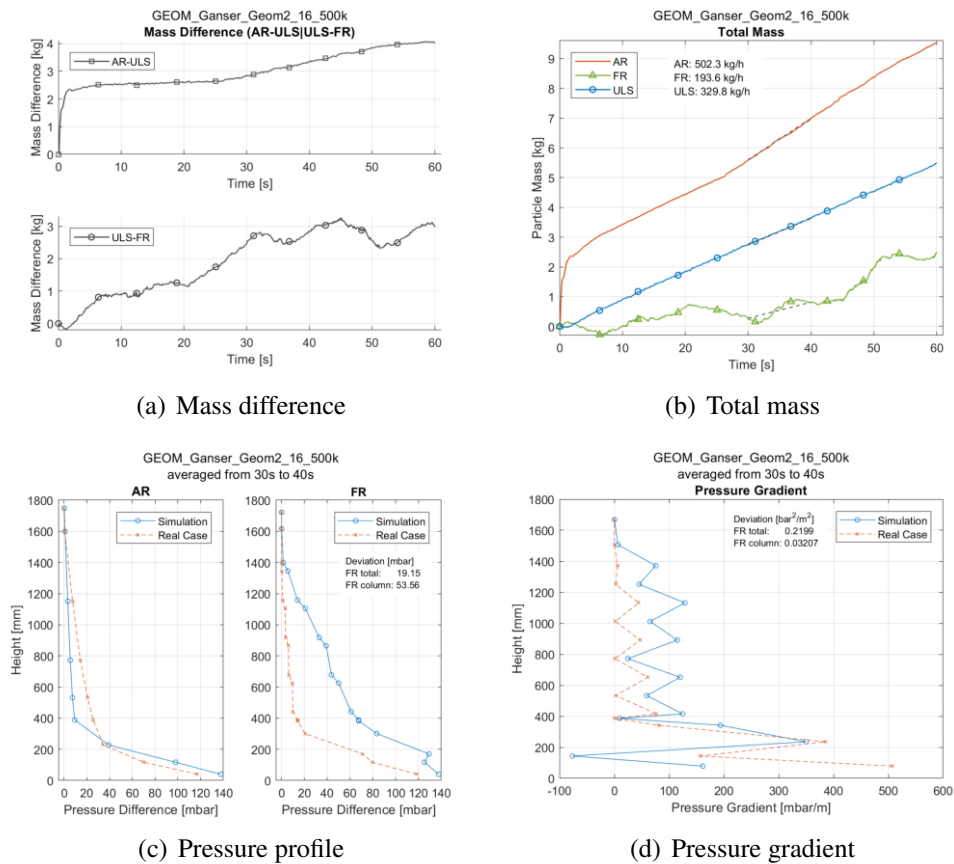
Figure 5.13: Simulation 500k Ganser - *G3*

WYE

Simulations in this section: W2 according to Table 3.2

The simulation using WYE as a drag law showed a negative mass flow rate of the FR column at the beginning of the simulation. This means that particles were transported from the bubbling bed into the FR column itself. This trend continued for about 25*s* until the FR column mass flow rate seemed to become stable. The AR SEP was steadily flooded with bed material, because of the bigger AR mass flow rate compared to the ULS mass flow rate. This trend is also depicted in Figure 5.12. Additionally, the most upper compartment of the FR column was filled with too much bed material indicated by the pressure gradient and the visual observation itself.

(a) Mass difference

(b) Total mass

(c) Pressure profile

(d) Pressure gradient
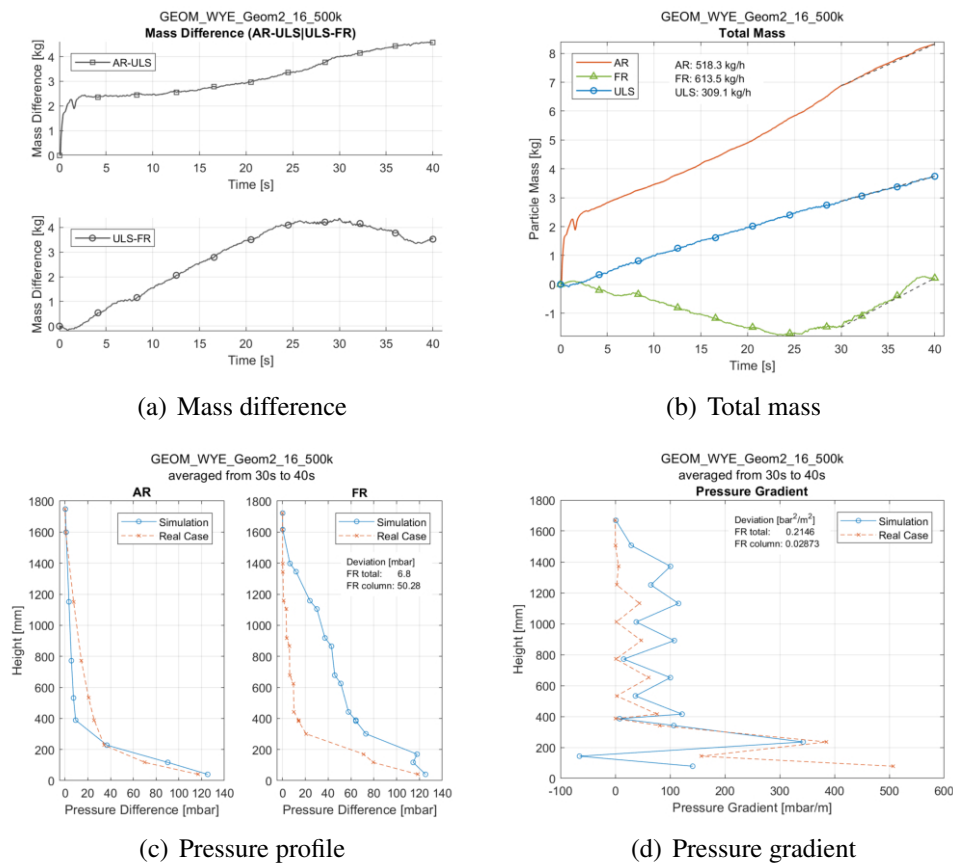
Figure 5.14: Simulation 500k WYE - *W2*

Conclusion of 500k simulation

The results of the simulation with $500k$ real cells are visualized in Figure 5.15 and the exact values are in Table A.3 attached in the appendix.
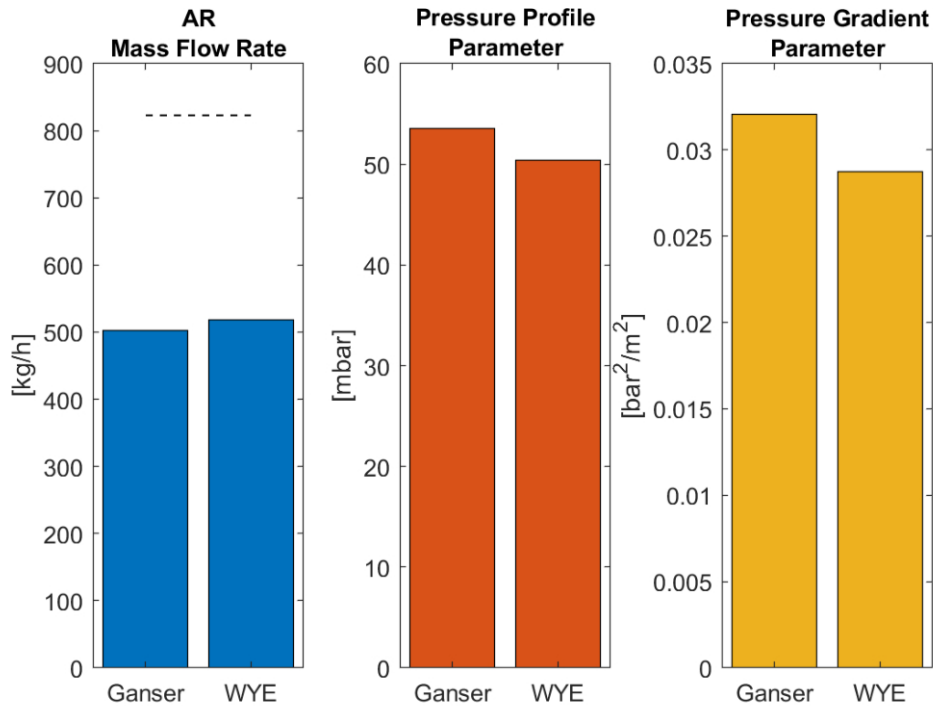
Figure 5.15: Drag law (500k) - result comparison

Both drag laws produced similar results and for the continuing simulations the Ganser drag law was favored. Even though WYE scored slightly better on the defined parameters, other characteristics indicated that Ganser is the better option. Especially the faster flooding of the AR SEP due to the greater differences of AR and ULS mass flow and the slightly more loaded upper part of the FR column were a deciding factor to favor Ganser at first glance. Additionally, the averaging times are very short and therefore the parameters can vary e.g. the Ganser simulation evaluated at $60s$ would lead to slightly better parameters as seen in Section 5.3.3.1.

Based on the investigation in this chapter one can state:

Ganser is the best suited drag law and will be used for further simulations

5.3.2 Altering the geometry

Simulations in this section: G3, G4, G5 according to Table 3.2

In this section alterations of the geometry are investigated, like FR gap and pipe diameter.

In the previous simulation (simulation G3) in Section 5.3.1.2 too many particles were distributed in the FR column, as indicated by the pressure gradient in Figure 5.13d, and also the AR SEP started to flood (see Figure 5.13a. In this section the geometry of the model was slightly altered in an attempt to improve the predicted simulation results. The FR gap in the column was increased so less particles would remain in the FR column. The pipe diameter connecting the AR SEP and ULS in one case, and all connecting pipes with a diameter of $32mm$ in the other case, were subject to alteration to allow larger particle mass flows and prevent flooding of the AR SEP.

Simulation *G3* is a simulation without any alteration of the geometry. This simulation can be found in Section 5.3.1 with the set grid size of $500k$. The results indicate that the FR columns bed heights are too high. Therefore, the FR gap was increased from $16mm$ to $18mm$, respectively to $20mm$, so particles could drop down more easily.

Table 5.5: Varying geometry - results overview

FR Gap	Mass Flow			Pressure Parameters in FR Column		Pipe diameter increased from $32mm$ to $40mm$
	AR $\left[\frac{kg}{h}\right]$	FR $\left[\frac{kg}{h}\right]$	ULS $\left[\frac{kg}{h}\right]$	P_{PP} [$mbar$]	P_{PG} $\left[\frac{bar^2}{m^2}\right]$	
16	502.3	193.6	329.8	53.56	0.03207	-
18	346.0	81.6	368.1	39.04	0.02449	ULS to AR
20	477.4	438.2	400.7	36.11	0.01719	all

5.3.2.1 FR Gap 18mm with ULS pipe enlarged from 32mm to 40mm

Simulations in this section: G4 according to Table 3.2

Simulation *G4* has a diameter of the pipe connecting the AR SEP and ULS of 40*mm* instead of 32*mm* and was an attempt of the previous simulation to reduce flooding in the AR SEP as shown in Figure 5.13a in Section 5.3.1.2. The simulation with increased FR gap and pipe diameter was initialized using the operating conditions of simulation *G3* at 30*s*.

At the end the FR mass flow stagnates but all simulations showed a certain degree of fluctuation in the FR mass flow rates. The smaller FR flow was assumed to be only temporarily reduced and to recover again. The AR mass flow was reduced, compared to the simulation without geometric adaption but is steady. This adjustment seemed to improve the overall performance of the particle mass flow rates leading to a steady state, while improving the distribution of particles in the FR column.

(a) Mass difference

(b) Total mass

(c) Pressure profile

(d) Pressure gradient
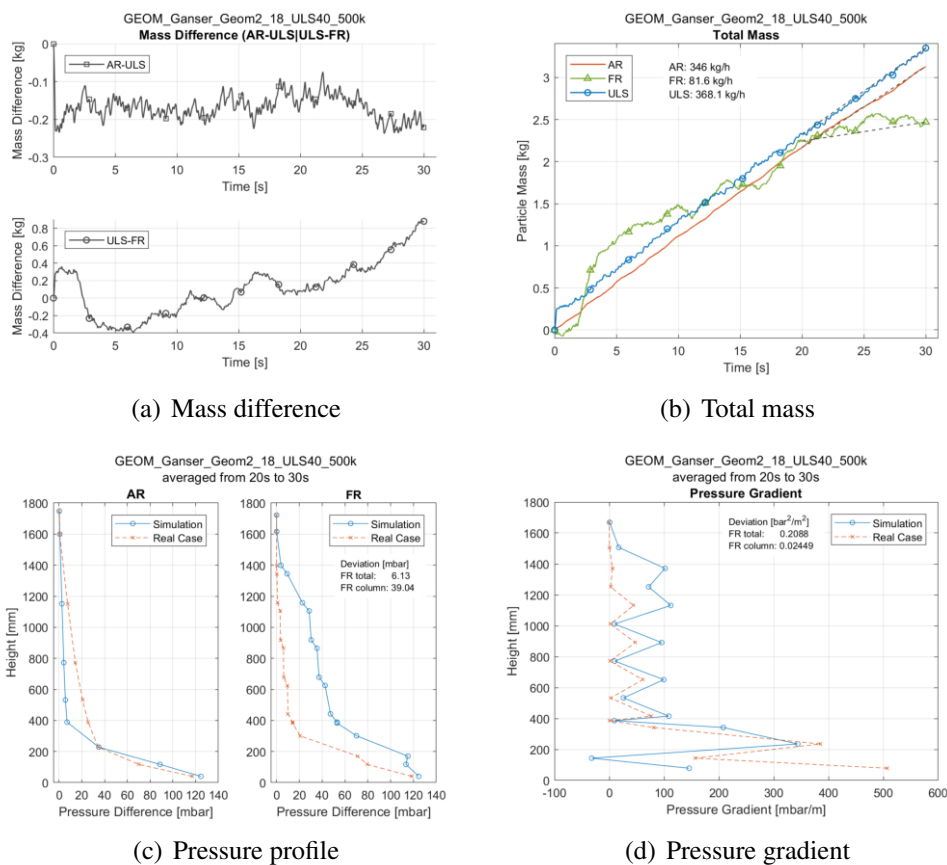
Figure 5.16: FR Gap 18mm and enlarged ULS pipe diameter - *G4*

5.3.2.2 FR Gap 20mm with all pipes enlarged from 32mm to 40mm

Simulations in this section: G5 according to Table 3.2

Additionally, the whole geometry was enlarged by increasing all pipe diameters from 32*mm* to 40*mm* and increasing the FR gap to 20*mm*. This measure improved the overall performance of the simulation even more. This measure was already altering the model so extensively, that only the simulation with 18*mm* FR gap space and 40*mm* of ULS-pipe diameter was chosen for further improvement and the simulation was only run for 15*s* to see a trend.

(a) Mass difference

(b) Total mass

(c) Pressure profile

(d) Pressure gradient
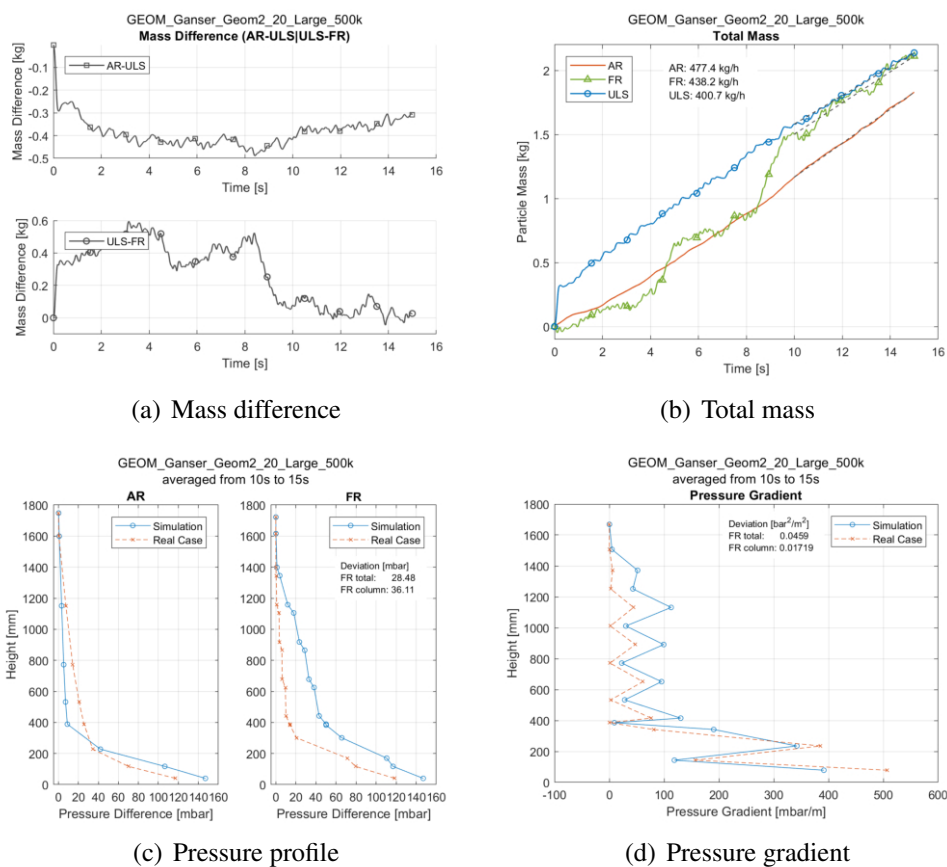
Figure 5.17: FR Gap 20mm and enlarged pipe diameters - *G5*

5.3.2.3 Conclusion of altered Geometry

The altered geometry showed significant improvement. The AR SEP did not flood anymore and the deviations in the pressure gradient and pressure profile were reduced. Nevertheless, the particle circulation rate target values were not reached and additional adjustments were needed.

5.3.3 Varying P_S

Simulations in this section: G3, G4, G9, G14, G17, G18, G22, G23, G24, G25 according to Table 3.2

In this section the P_S value was varied and simulations were conducted with altered and normal geometry .

The P_S constant is used to calculate the particle normal stress. The P_S constant's unit is Pa and will hereafter be listed abbreviated without its unit (e.g. $P_S = 30Pa$ is written as $P_S = 30$). The particle normal stress is only important near close-pack and has little effect in a diluted system. Eq. 2.50 describes the calculation of particle normal stress and illustrates the linear dependency to the P_S value. The higher the P_S value is set the bigger the particle stress value gets and therefore the harder it is for particles to reach close-pack. Therefore, increasing the P_S value will lead to loser packed bed material if they approach close-pack, as it does not influence a diluted system. Especially the FR bubbling bed, FR column and loop seals do have a high particle volume fraction and will be affected by this setting.

The influence of the increased P_S values is clearly visible by comparing the snapshots of the simulation depicted in Figure 5.18. The color bar in Figure 5.18 indicates the particle volume fraction and with increased P_S the color changes from red, indicating a value near close-pack to a more orange color, indicating a not so dense packed system. Also, the pipes and loop seals seem to be better fluidized by following the same trend of an increased fluid volume fraction.

The variation of P_S led to improvements in the particle distribution, pressure profile, and mass flow rates. The different P_S values were tested with and without altered geometry, labeled in Figure 5.18 as *altered* or *normal*. The altered geometry had an increased FR column gap size, and the pipe diameter connecting the ULS and AR SEP was increased from $32mm$ to $40mm$.

The simulations in this section with a P_S value ranging from $P_S = 30$ to $P_S = 100$ were initialized with the same initial conditions. To achieve uniform initial conditions the simulation *G23* was conducted for a total of $60s$. The conditions of this simulation at $30s$ was used as initial conditions for the other simulations. Therefore, all simulations were conducted for a total of $30s$ with initial conditions of *G23* at time step $30s$. The initial conditions for simulations *G3* and *G4* with $P_S = 1$ were different and will be discussed in the respective section.

(a) $P_S = 1$ - normal   (b) $P_S = 1$ - altered   (c) $P_S = 30$ - normal   (d) $P_S = 30$ - altered

(e) $P_S = 50$ - normal   (f) $P_S = 50$ - altered   (g) $P_S = 65$ - normal   (h) $P_S = 65$ - altered

(i) $P_S = 100$ - normal   (j) $P_S = 100$ - altered
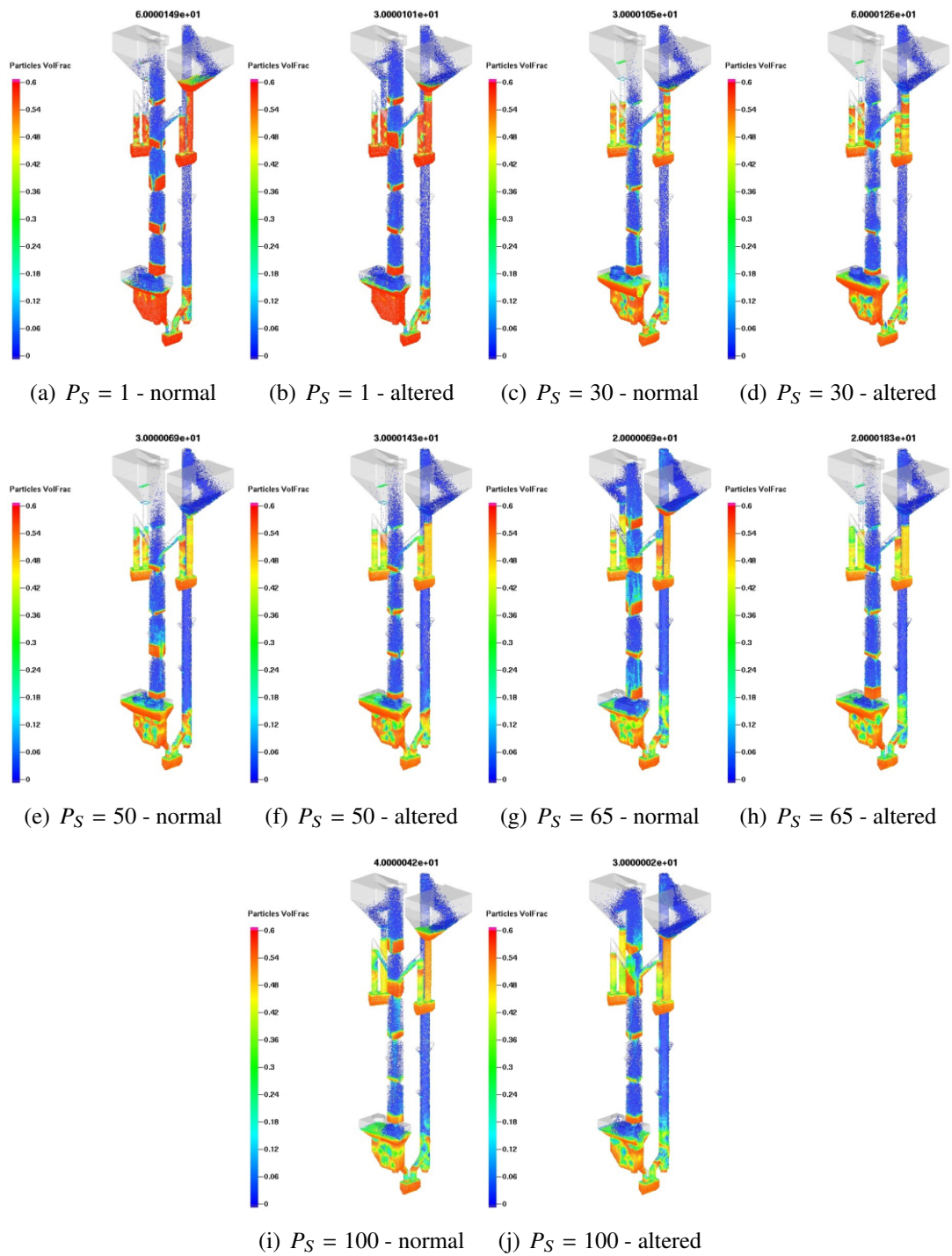
Figure 5.18: Snapshots of animation from P_S alteration - overview

5.3.3.1 P_S set to 1

Simulations in this section: G3, G4 according to Table 3.2

The initial conditions of the simulations with $P_S = 1$ are not based on simulation *G23*, because the simulation with normal geometry (*G3*) is the same simulation as in Section 5.3.2 but was evaluated at $60s$ and therefore not redone. Simulation *G4* has the altered geometry, was also conducted in Section 5.3.2, and was initialized using the conditions of simulation *G3* at $30s$. The simulation with altered geometry had a better performance.

(a) Total mass

(b) Pressure gradient
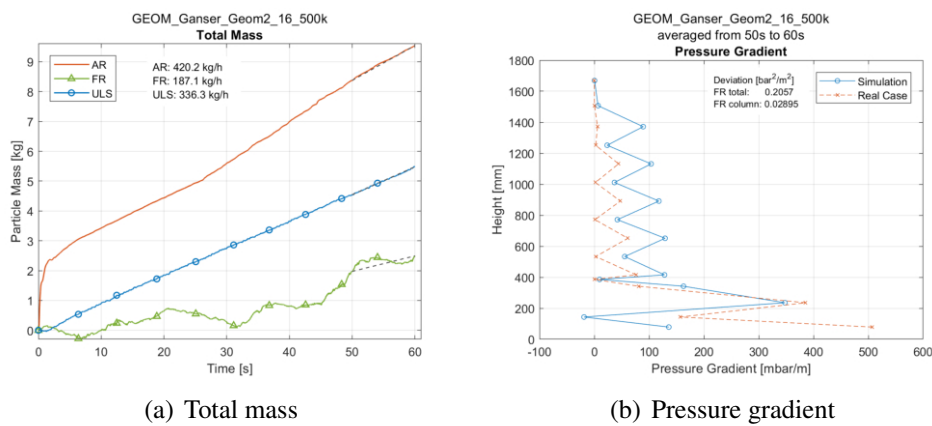
Figure 5.19: $P_S = 1$ without altered geometry - *G3*

(a) Total mass

(b) Pressure gradient
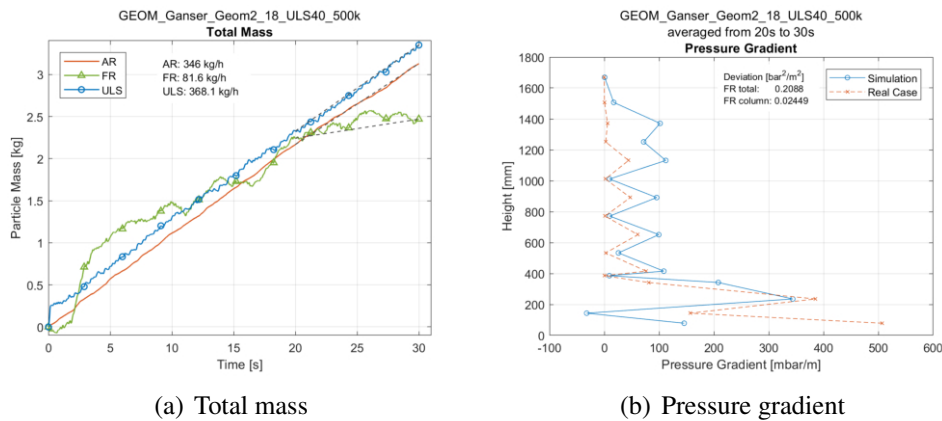
Figure 5.20: $P_S = 1$ with altered geometry - *G4*

5.3.3.2 P_S set to 30

Simulations in this section: G9, G23 according to Table 3.2

Both simulations do have an improved particle mass flow and pressure paramters compared to the simulations *G3* and *G4* with $P_S = 1$, and are stable. The simulation with enlarged geometry gives slightly better results but also the simulation without any geometrical alteration achieves a good performance.

(a) Total mass (b) Pressure gradient
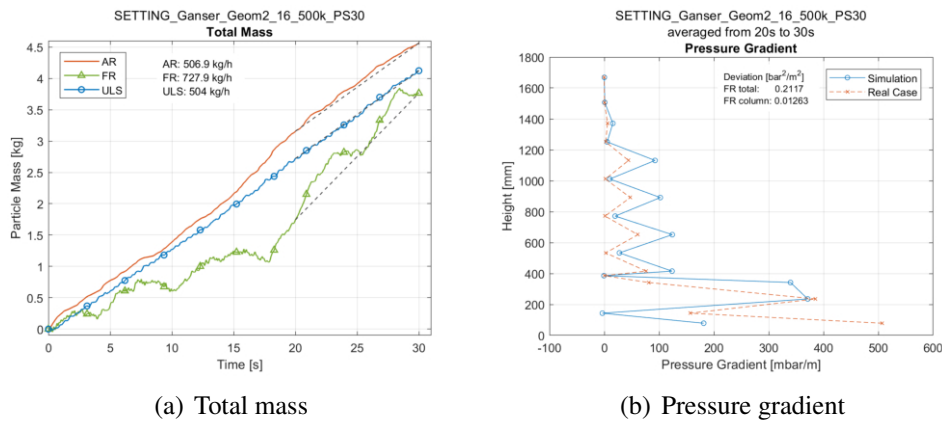
Figure 5.21: $P_S = 30$ without altered geometry - *G9*

(a) Total mass (b) Pressure gradient
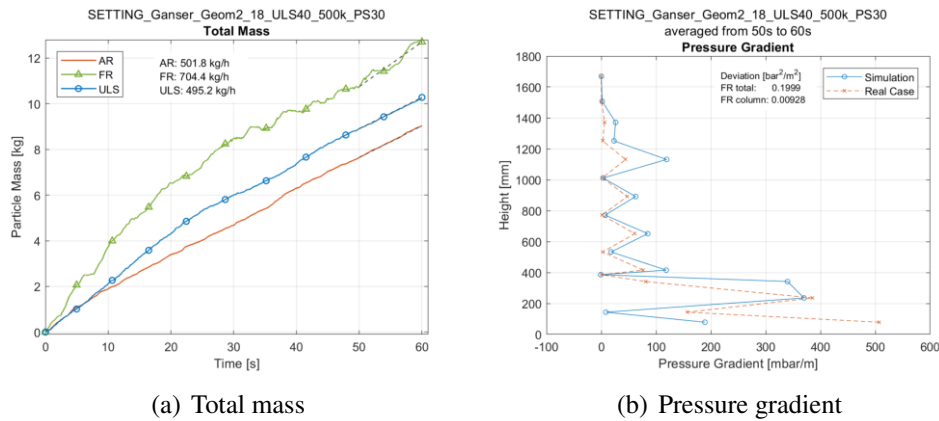
Figure 5.22: $P_S = 30$ with altered geometry - *G23*

5.3.3.3 P_S set to 50

Simulations in this section: G14, G24 according to Table 3.2

The simulations improvements are very similar to the ones with $P_S = 30$. The mass flow increased even further while being stable in both AR SEP and FR column. The simulations with and without altered geometry were very similar in terms of mass flow and pressure parameters.

| (a) Total mass | (b) Pressure gradient |
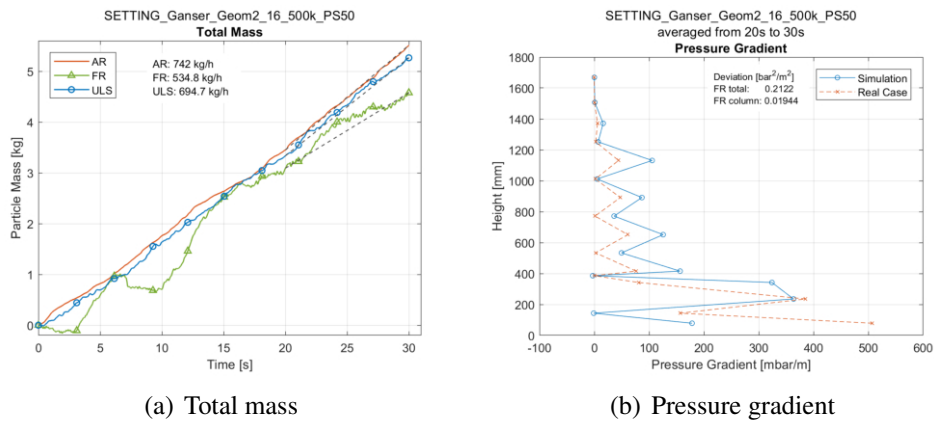
Figure 5.23: $P_S = 50$ without altered geometry - *G14*

| (a) Total mass | (b) Pressure gradient |
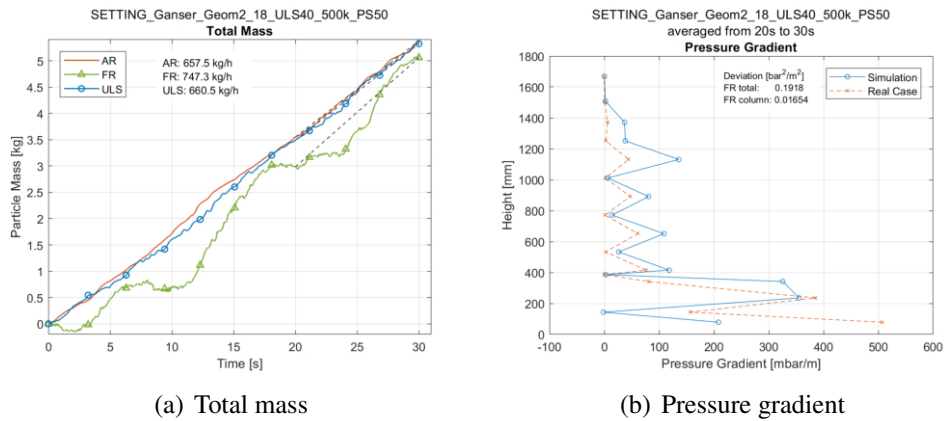
Figure 5.24: $P_S = 50$ with altered geometry - *G24*

5.3.3.4 P_S set to 100

Simulations in this section: G18, G22 according to Table 3.2

The simulation with non-altered geometry was already conducted with a different particle distribution as initial conditions (see Figure 3.8b) and not rerun based on the observations made. The simulation was run for additional $10s$ and was assumed to be steady. In both cases the mass flow rates were comparable to each other and therefore the system was stable, but the mass flow rates were overpredicted and additionally the pressure parameters scored worse compared to the simulations with P_S set to 30 or 50.

(a) Total mass   (b) Pressure gradient
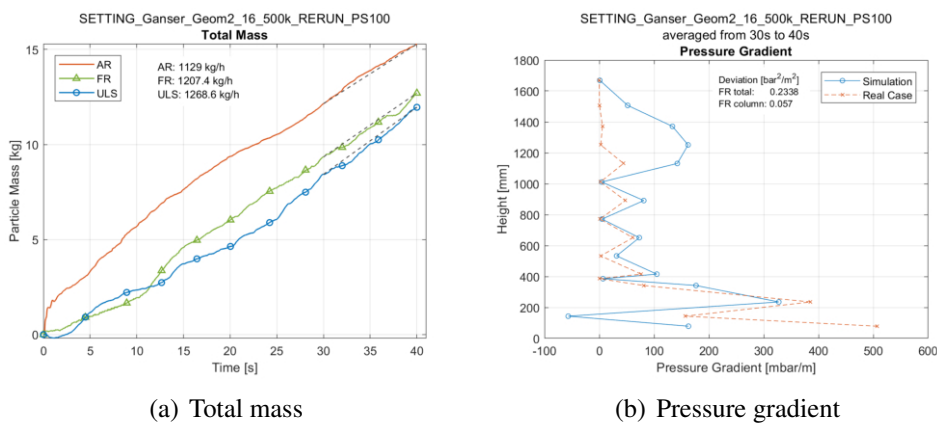
Figure 5.25: $P_S = 100$ without altered geometry - *G18*

(a) Total mass   (b) Pressure gradient
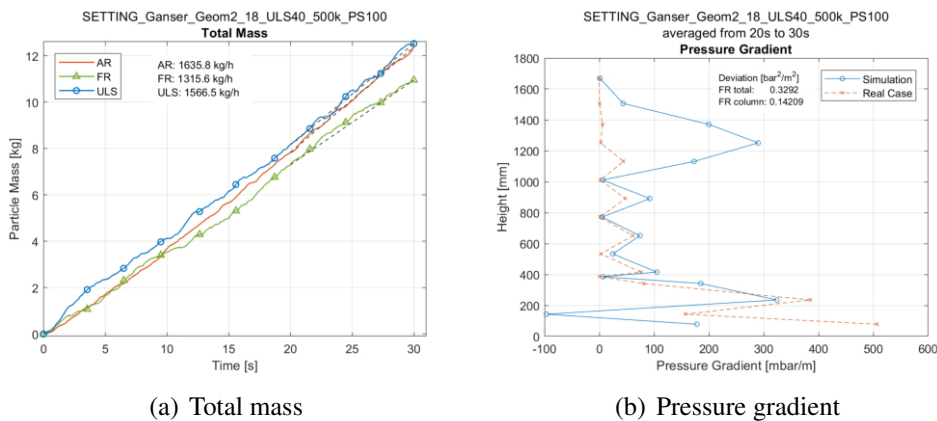
Figure 5.26: $P_S = 100$ with altered geometry - *G22*

5.3.3.5 Conclusion of varying P_S

The results of the simulations with varying P_S values are visualized in Figure 5.27 and the exact values are attached in the appendix in Table A.4.
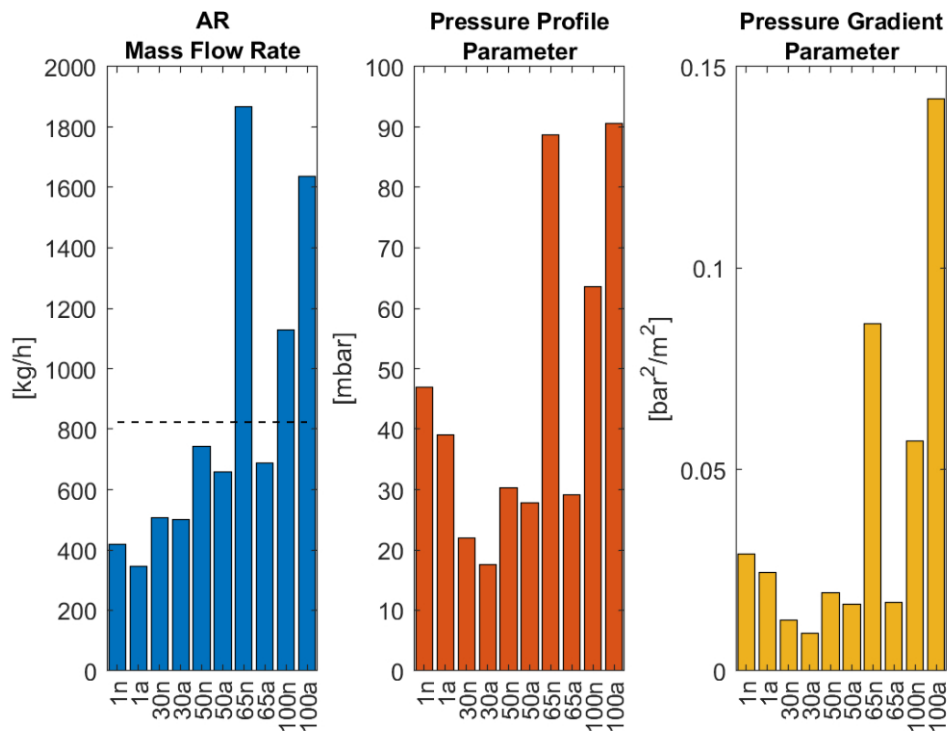
Figure 5.27: P_S variation - results comparison

The abbreviations in Figure 5.27 are explained briefly. The number indicates the P_S value while the letter "n" means normal geometry and "a" altered geometry.

The simulation with $P_S = 30$ and $P_S = 50$ showed significant improvements compared to the cases with $P_S = 1$. The altered particle stress led to smaller bed heights in the column, resulting in better pressure profile parameters. Furthermore, the systems were stable and had increased particle mass flow rates. As listed in Table A.4 the simulation with $P_S = 30$ scores the best pressure parameter results, while also maintaining a reasonable mass flow. $P_S = 50$ produces even more accurate mass flow rates close to the target value but the pressure parameters were worse compared to simulation with $P_S = 30$. The mass flow rate can be influenced by loop seal fluidization and therefore $P_S = 30$ was chosen to be tested under conditions with increased loop seal fluidization rates (see Section 5.3.4). While the altered geometry produced partly better results, the following adjustments were studied on the normal geometry. The non-altered geometry approach was favored because of comparable good results and less modifications.

Based on the investigation in this chapter one can state:

A P_S value of 30 and 50 improves the simulations significantly.

5.3.4 Loop seal fluidization

Simulations in this section: E2, E3, G1, G10, G13, W3, W4 according to Table 3.2

Previous simulations led to the conclusion that the simulation with the Ganser drag law does not achieve the measured circulation rates and $P_S = 30$ led to good results but too low bed material circulation rates. Therefore, the air injection was increased in the loop seals to ensure sufficient fluidization as discussed in Section 5.2.

The loop seal fluidization rate was increased by the factor 1.75, and in one case by 2.5, in every loop seal to investigate its influence on the bed material circulation rate.

The influence of regular and altered loop seal fluidization rates was tested in simulation *G1* (see Figure 5.28). The simulation had altered geometry, $P_S = 1$, and was conducted for $20s$. The first $10s$ of the simulation were conducted with regular, and the second half with increased loop seal fluidization rates.
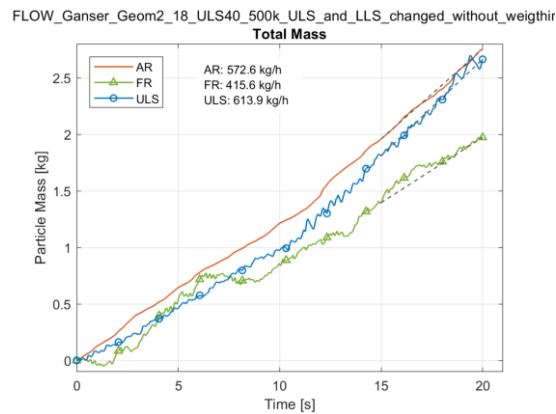
Figure 5.28: Altered geometry and increasing loop seal fluidization rate - *G1*

A clear trend of increased particle mass flow can be seen with higher fluidization rates in Figure 5.28. This indicates that there is still a big dependence of the circulation rate of the bed material from the loop seal fluidization. Martinovic [52] investigated this dependency too and concluded that only minor changes occur in the particle circulation rate of the real cold flow model with LLS fluidization rates increased over $0.8^{Nm^3}/_h$. Overall the AR mass flow rate was clearly increased and approached the target value but did not reach it. Therefore, a combination of both increased loop seal fluidization rates and increased P_S value was tested subsequently.

5.3.4.1 Increased loop seal fluidization with $P_S = 30$

Simulations in this section: G10, G13 according to Table 3.2

The simulation without the increased loop seal fluidization rates was already conducted and is depicted in Figure 5.21. The same set-up of the simulation was used but with increased loop seal fluidization rates. The loop seal fluidization rate was increased by a factor of 1.75 (see Table 5.4).

(a) Mass difference

(b) Total mass

(c) Pressure profile

(d) Pressure gradient
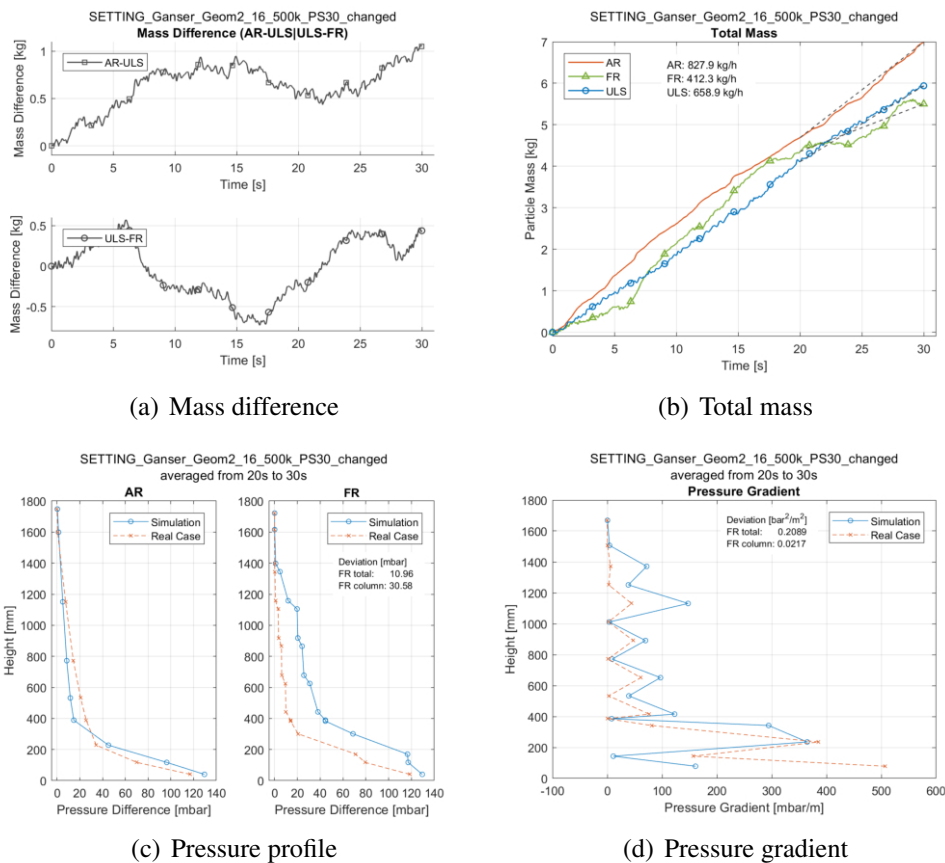
Figure 5.29: $P_S = 30$ and loop seal fluidization rates increased 1.75 times - *G10*

As Figure 5.29 indicates the increased loop seal fluidization rates led to the best results so far. Fluctuations of the AR, FR and ULS mass flows are still present but the mass difference over the test period remains quite stable. For comparison the respective mass flow rates averaged between $10s$ to $20s$ would be $AR = 748.2^{kg}/h$, $FR = 800.5^{kg}/h$ and $ULS = 812.8^{kg}/h$. Because of the fluctuation and the relative short simulation duration the absolute values can vary, but the overall observation leads to the conclusion that the target value of $823^{kg}/h$ is almost achieved with that simulation.

To investigate the dependence of the mass flow from the loop seal fluidization even

further the fluidization rates were increased from the normal value by a factor of 2.5 and the simulation was rerun.

(a) Mass difference

(b) Total mass

(c) Pressure profile

(d) Pressure gradient
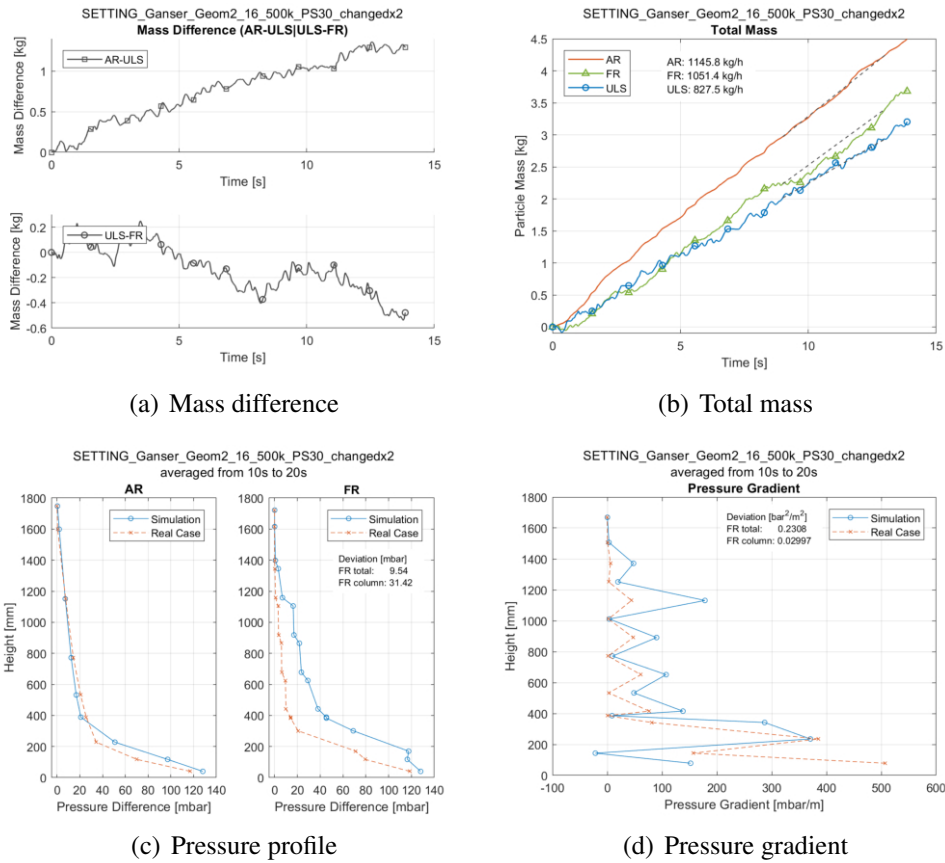
Figure 5.30: $P_S = 30$ and loop seal fluidization rates increased 2.5 times - *G13*

The simulation with even higher fluidization rates shows on the one hand that the simulation becomes unstable and is still heavily dependent on the fluidization and on the other hand that the ULS mass flow rate seems to be a bottleneck, of the overall mass flow, close to the target value of $823^{kg}/_h$.

5.3.4.2 Comparison with the other drag laws

Simulations in this section: E2, E3, W3, W4 according to Table 3.2

The simulations in Section 5.3.3 and Section 5.3.4 were conducted using the Ganser drag law. For comparison the simulations with improved settings were redone using the EMMS and WYE drag law in this section.

The results in this section indicated that the simulations with WYE and EMMS could be improved by adjusting the P_S value and increasing the loop seal fluidization rates but that the circulation rates were not satisfying as listed in Table A.5

The graphs for *E2*, *E3*, *W3* and *W4* are attached in the appendix (Figure A.22 to Figure A.25).

The initial condition and conditions of the simulation with $P_S = 30$ and increased loop seal fluidization rate after 20s are depicted in Figure 5.31.

(a) Initial conditon

(b) EMMS

(c) Ganser

(d) WYE
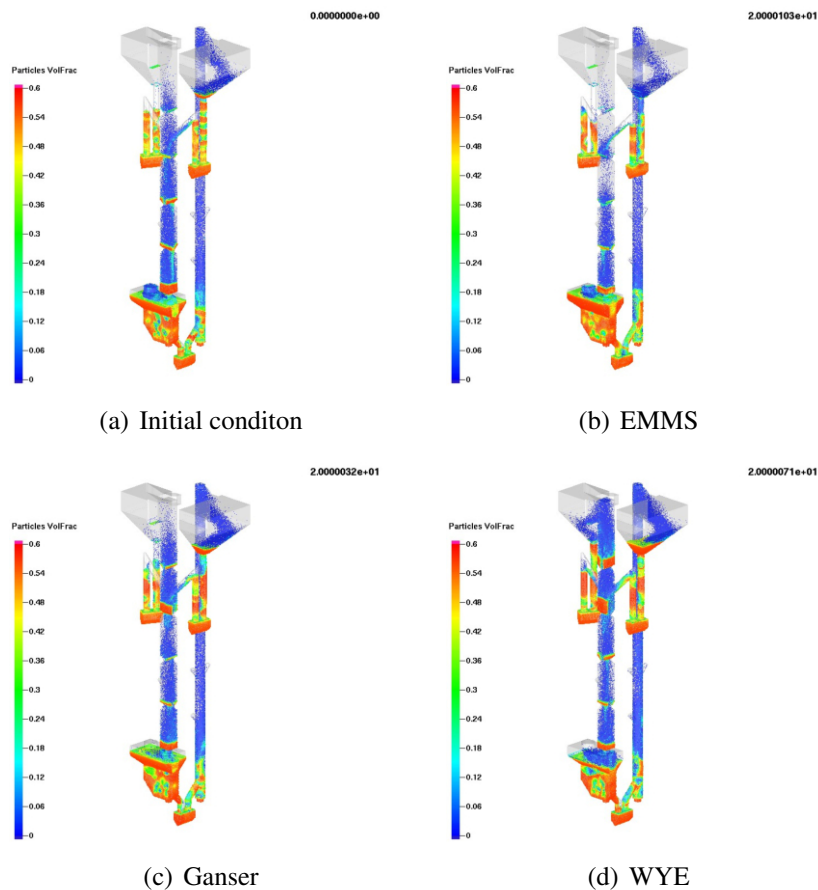
Figure 5.31: Drag law comparison at 20s

5.3.4.3 Conclusion of increased loop seal fluidization rates with different drag laws

The simulation with Ganser as the drag law calculated a steady state with particle circulation rates close to the target value. The simulations with WYE were still not stable, because of the difference of the AR and ULS mass flow rates (see Figure 5.32).

(a) Normal - *W3*   (b) Increased - *W4*
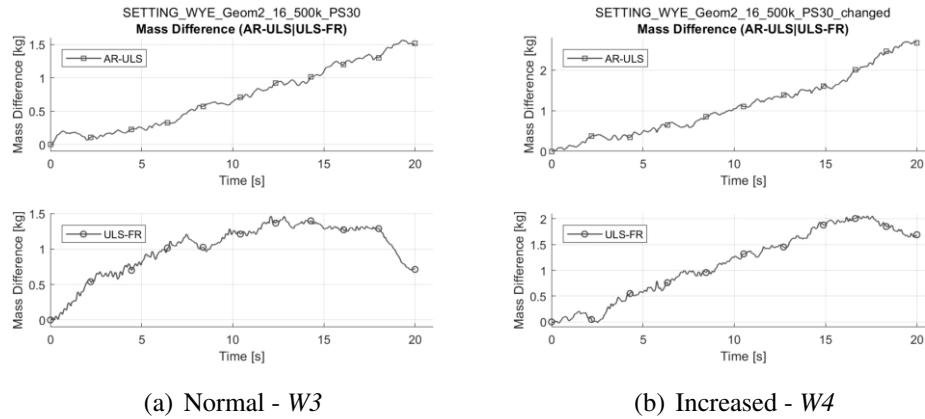
Figure 5.32: $P_S = 30$, WYE, normal and increased loop seal fluidization rate

The EMMS drag law predicted the particle circulation rates still too small but stable. The large FR mass flow rate in the simulation with changed fluidization listed in Table A.5 is due to the fact that the simulation was initialized with a filled column. The ULS and AR mass flow were smaller and as a result the FR column emptied itself. Because of the poor performance it was not waited until the mass flows became steady and therefore it was stopped after $20s$.

Ganser had the best performance, compared to EMMS and WYE. The simulation *G10* showed a significant improvement compared to simulation *G9*. Furthermore, in comparison with simulation *G1* the importance of the increased P_S value is noticeable, as the increased loop seal fluidization rate solely did not achieve particle circulation rates close to the target value of $823^{kg}/h$. The increased loop seal fluidization rate is a good tool to control the circulation rate of the bed material.

The results of the simulations are depicted in Figure 5.33. The abbreviations in the figure are explained briefly. The letter "g", "w" and "e" indicates the drag law (Ganser, WYE or EMMS). The following number stands for the P_S value. The suffix "n", "a" or "b" indicates the loop seal fluidization, where "n" is normal loop seal fluidization rate, "a" increased by 1.75 and "b" increased by 2.5. For example "g30b" is the simulation with the Ganser drag law, $P_S = 30$ and loop seal fluidization rates increased by 2.5.
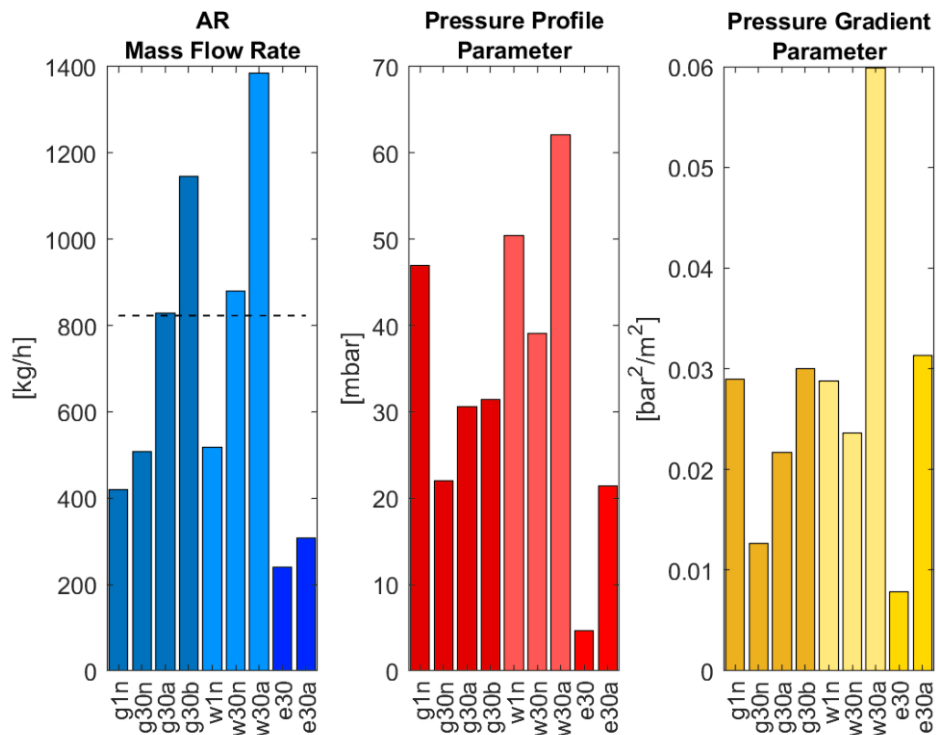
Figure 5.33: Overview with different P_S, drag law and loop seal fluidization rates

The values of the simulations compared in Figure 5.33 are attached in the appendix in Table A.5. The simulations with Ganser and an adjusted P_S value were stable and improved with increased loop seal fluidization rates. The WYE drag law predicted an AR mass flow larger than the ULS mass flow rate in all tested cases. This led to flooding of the AR SEP and an unsteady state. The EMMS mass flow underestimated the mass flows generally with all adjustments. Those trends were similar to the ones observed in Section 5.3.1. Therefore, Ganser proved to be the best fit for the simulations and the WYE and EMMS drag laws were not considered further.

Based on the investigation in this chapter one can state:

An increased loop seal fluidization rate with Ganser and P_S = 30 improves the performance significantly. The EMMS and WYE drag laws are also with improved settings inappropriate.

5.4 Best cases applied on other operating points

Simulations in this section: G10, G11, G12, G14, G15, G16 according to Table 3.2

After validating one operating point, the improved settings were tested for different operating points. The case with $P_S = 50$, and the case with $P_S = 30$ and increased fluidization were used to investigate different operating points at different AR fluidization rates. Therefore, cases, beside the former case with an AR fluidization rate of $24^{Nm^3}/_h$, with $16^{Nm^3}/_h$ and $20^{Nm^3}/_h$ AR fluidization rates were simulated and compared with the results of Martinovic [52].

5.4.1 $P_S = 30$ and increased loop seal fluidization rates

In this section, increased loop seal fluidization rates by factor 1.75 were applied with $P_S = 30$.

5.4.1.1 AR $16^{Nm^3}/_h$

Simulations in this section: G11 according to Table 3.2

The AR fluidization rate was set to $16^{Nm^3}/_h$. The simulation was initialized using a previous simulation (*G10*). The simulation was very unstable at the beginning, but after roughly $40s$ started to become stable.

The pressure profiles indicate a large number of particles in the upper part of the FR column. The overall mass flow shows the right trend by a decreasing mass flow rate with decreasing AR fluidization rate. The target value in Martinovic's thesis [52] was $302^{kg}/_h$. The value in this simulation was $379.9^{kg}/_h$ and therefore overpredicted.

(a) Mass difference

(b) Total mass

(c) Pressure profile

(d) Pressure gradient
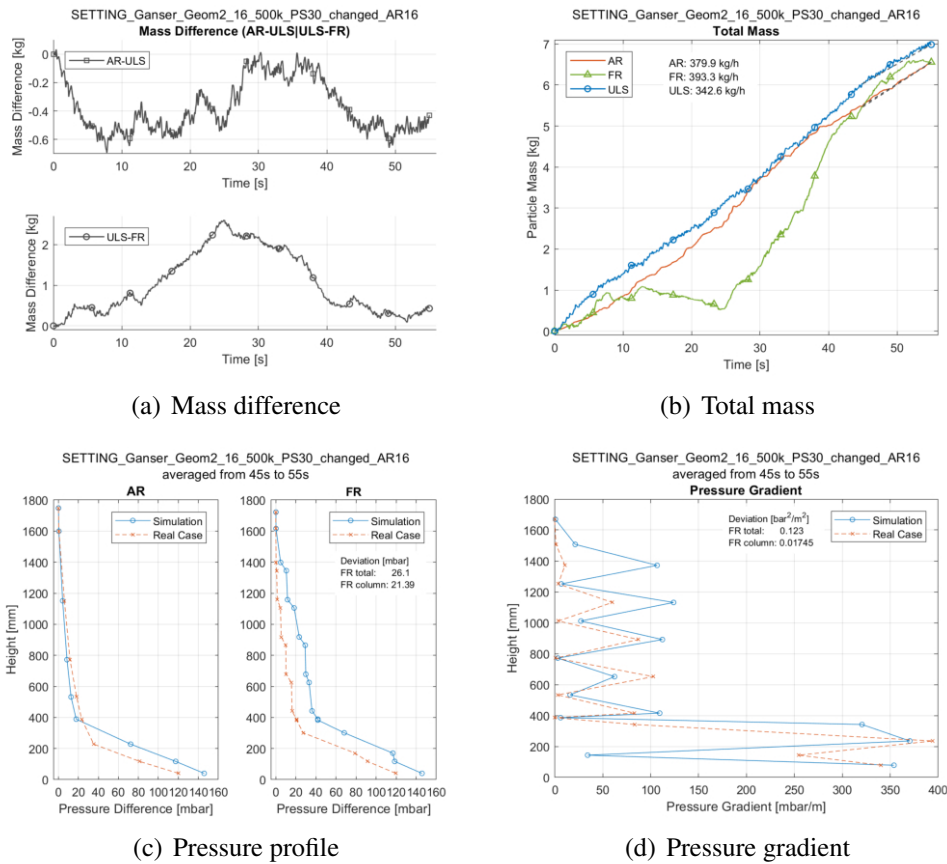
Figure 5.34: $P_S = 30$, increased loop seal and $16^{Nm^3}/_h$ AR fluidization rate - *G11*

5.4.1.2 AR $20^{Nm^3}/_h$

Simulations in this section: G12 according to Table 3.2

The simulation was initialized using a previous simulation (*G10*) and the AR fluidization rate was set to $20^{Nm^3}/_h$. The simulation was stable after approximately $30s$ but the pressure profiles still indicates that the upper part of the column is overloaded. The trend of a decreasing mass flow rate with decreasing AR fluidization rates is shown and the target value in Martinovic's thesis [52] was $504^{kg}/_h$. The value in this simulation was $601.6^{kg}/_h$ and therefore overpredicted.

(a) Mass difference

(b) Total mass

(c) Pressure profile

(d) Pressure gradient
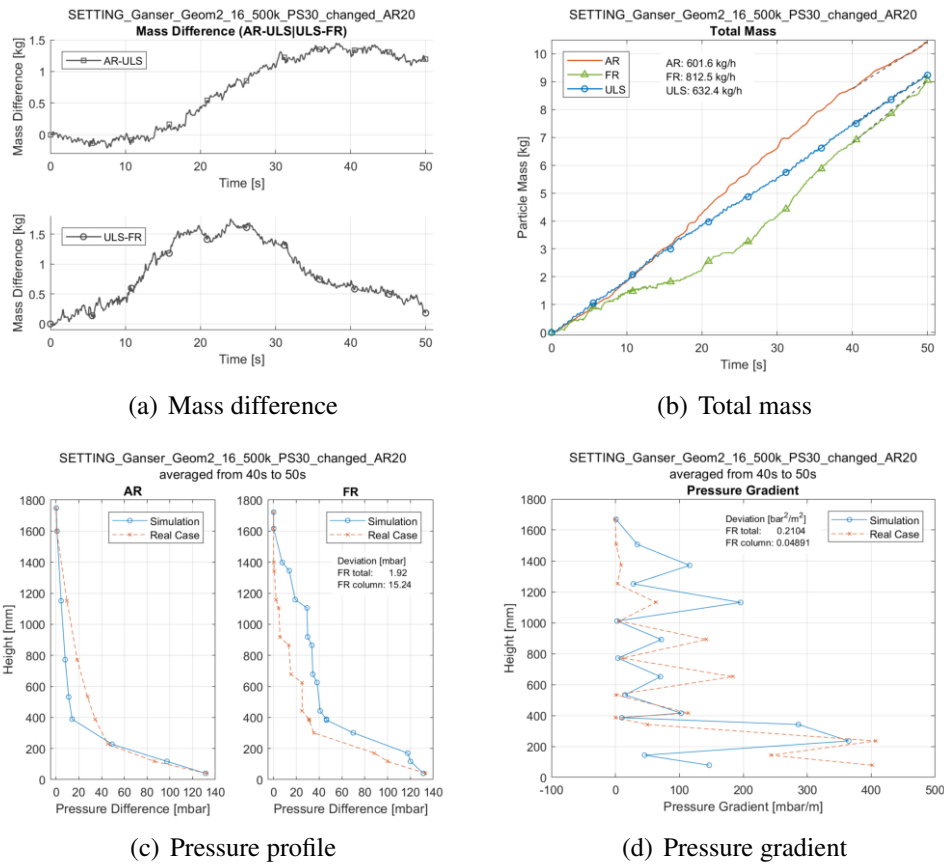
Figure 5.35: $P_S = 30$, increased loop seal and $20^{Nm^3}/_h$ AR fluidization - *G12*

5.4.2 $P_S = 50$ and normal loop seal fluidization rates

In this section, normal loop seal fluidization rates were applied with $P_S = 50$.

5.4.2.1 AR $16^{Nm^3}/_h$

Simulations in this section: G15 according to Table 3.2

The simulation was initialized using a previous simulation (*G11*) from Section 5.4.1.1 and the AR fluidization rate was set to $16^{Nm^3}/_h$. Because of the good initial conditions, the simulation was steady after approximately $15s$. The pressure profile is very close to the real value and the trend of a decreasing mass flow rate with decreasing AR fluidization is shown. The target value in Martinovic's thesis [52] was $302^{kg}/_h$ and slightly underpredicted with a value of $275.8^{kg}/_h$.

(a) Mass difference

(b) Total mass

(c) Pressure profile

(d) Pressure gradient
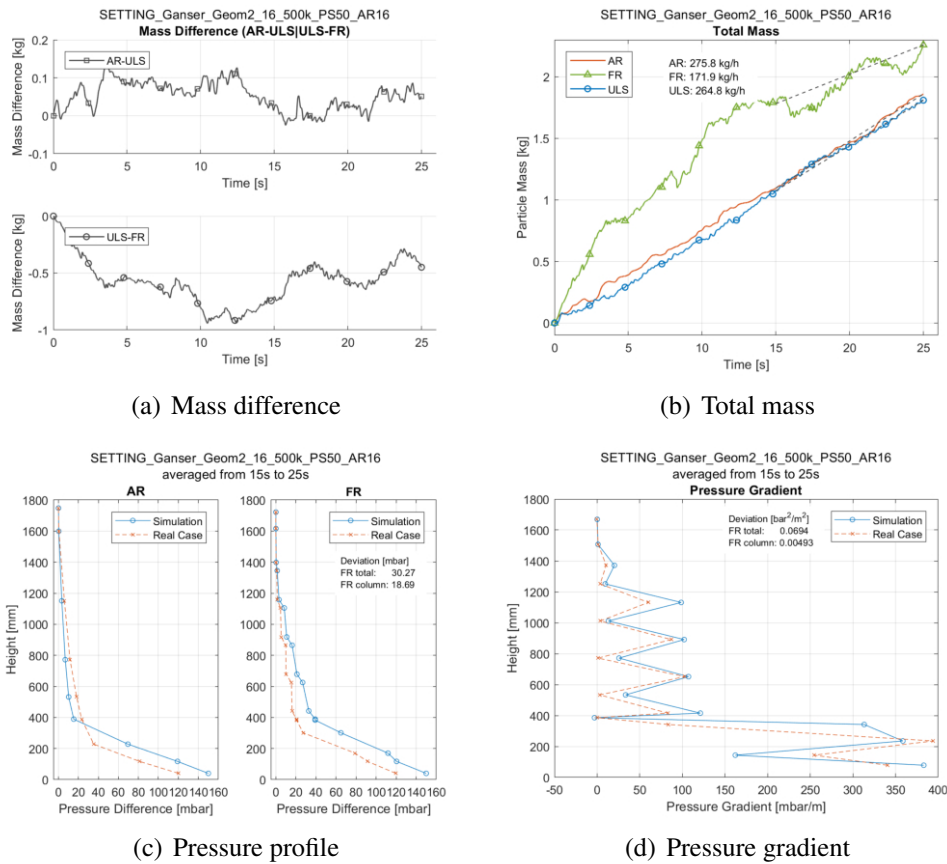
Figure 5.36: $P_S = 50$, normal loop seal and increased $16^{Nm^3}/h$ AR fluidization - *G15*

5.4.2.2 AR $20^{Nm^3}/h$

Simulations in this section: G16 according to Table 3.2

The simulation was initialized using a previous simulation (*G12*) from Section 5.4.1.2, the AR fluidization rate was set to $20^{Nm^3}/h$, and was steady after approximately $10s$. The pressure profile indicates that the number of particles is too large in the upper part and too small in the lower part of the FR column. The most upper part of the FR column fluctuated in mass over time. With longer simulation time a better particle distribution could eventually be achieved. The particle circulation rate of $504^{kg}/h$ of Martinovic's studies [52] was slightly overpredicted with a value of $540.1^{kg}/h$.

(a) Mass difference

(b) Total mass

(c) Pressure profile

(d) Pressure gradient
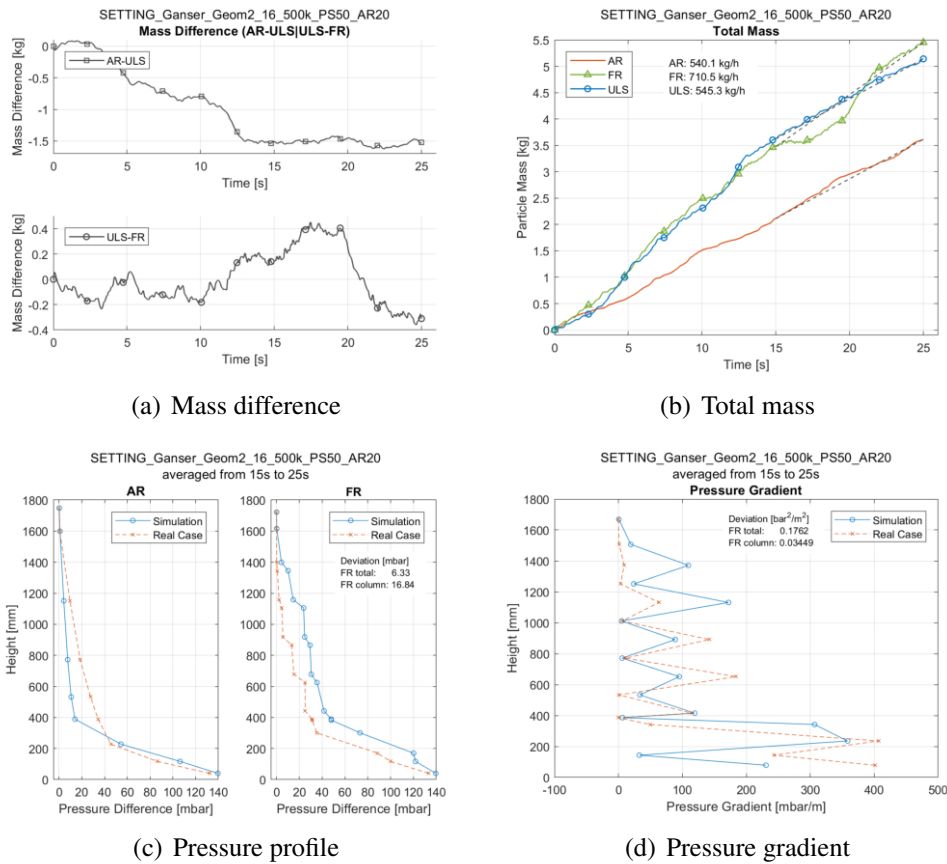
Figure 5.37: $P_S = 50$, normal loop seal and increased $20^{Nm^3}/h$ AR fluidization - *G16*

5.4.3 Conclusion of testing other operating points

The results of the simulation of different operating points are visualized in Figure 5.38. The actual values of the simulation are listed in Table A.6 and attached in the appendix.

In Figure 5.38 the cases with $P_S = 30$ and altered loop seal fluidization rates are labeled with "a" while the cases with $P_S = 50$ and non-altered loop seal fluidization rates are labeled with "b". The AR fluidization rate is indicated by the prefixed number. Therefore, "16a" means: AR fluidization rate of $16^{Nm^3}/h$ with $P_S = 30$ and altered loop seal fluidization rates.
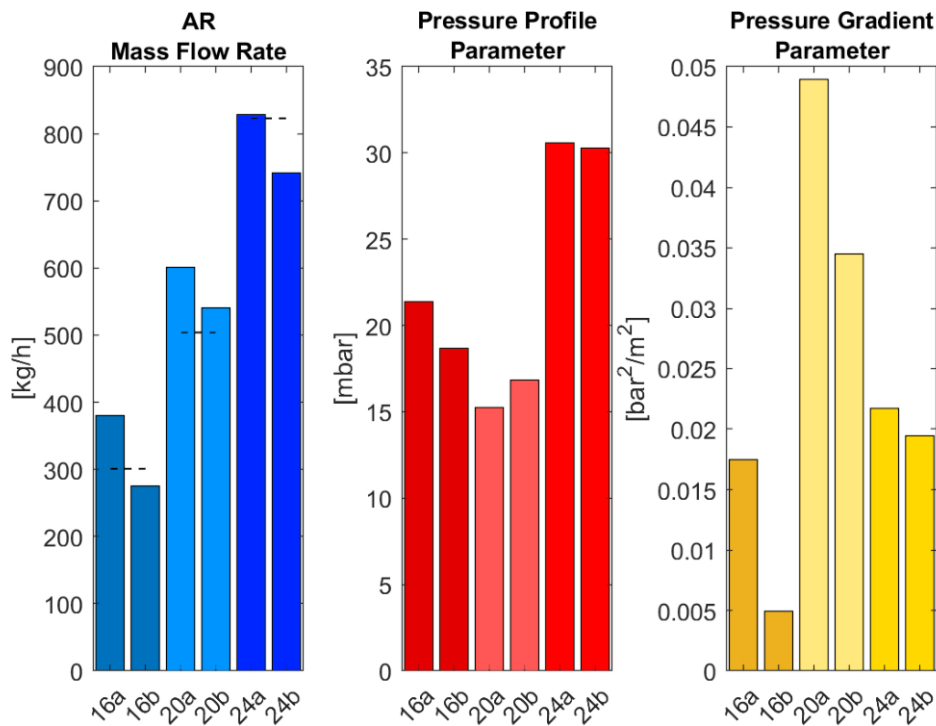
Figure 5.38: AR fluidization - overview

The simulation with altered loop seal fluidization rates and $P_S = 30$ predicts larger mass flow rates compared to the cases with normal loop seal fluidization rates and $P_S = 50$. The pressure difference over the FR column is in both cases very similar. The biggest difference can be seen in particle distribution in the column represented as the pressure gradient. The pressure gradient deviation visualized in Figure 5.38 indicates what can be observed in the pressure gradients plots, that the cases with $P_S = 50$ are much closer to the real values of the cold flow model than those with $P_S = 30$ and increased loop seal fluidization rates.

In this paragraph the settings with $P_S = 30$ and increased loop seal fluidization rates will be referred to as case *"A"*, while the settings with with $P_S = 50$ and normal loop seal fluidization rates will be referred to as case *"B"*. The particle circulations rates of the simulation are compared to the measured circulation rates by Martinovic [52].
The simulation with an AR fluidization rate of $16^{Nm^3}/_h$ was overpredicted with case A by 26% and underpredicted with case B by 9%.
The simulation with an AR fluidization rate of $20^{Nm^3}/_h$ was overpredicted with case A by 19% and overpredicted with case B by 7%.
The simulation with an AR fluidization rate of $24^{Nm^3}/_h$ was overpredicted with case A by 1% and underpredicted with case B by 10%.

Overall the simulation with $P_S = 50$ and regular loop seal fluidization had a better performance due to the pressure parameters and sufficient mass flow rates. The simulations with $P_S = 30$ and increased loop seal fluidization rates tended to overpredict the mass flow rates and accumulated too many particles in the upper part of the FR column.
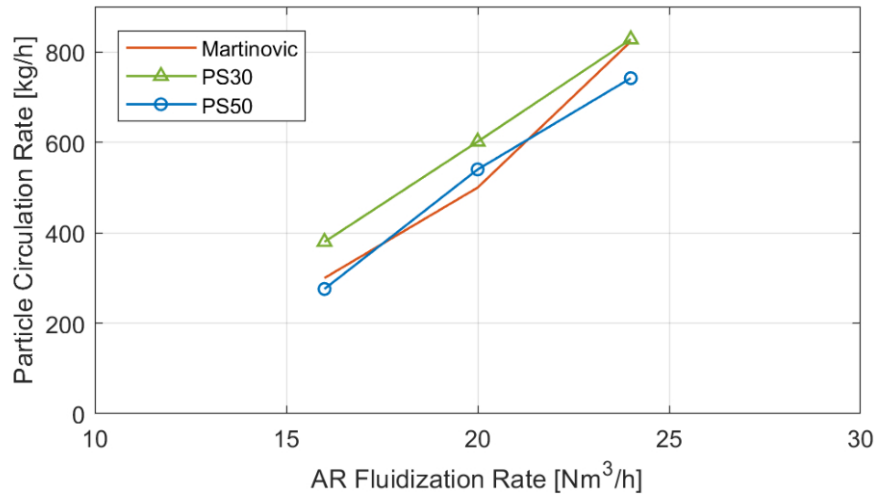
Figure 5.39: Circulation rate over AR fluidization rate

The dependence of the particle circulation rate from the AR fluidization rate of the real case and the simulated cases is depicted in Figure 5.39. Figure 5.39 shows the clear trend of increasing particle circulation rates with increased AR fluidization rates.

Based on the investigation in this chapter one can state:

The best results on various operating points are calculated with a P_S value of 50.

5.4.4 Outlook

Simulations in this section: G20, G21, G26 according to Table 3.2

The influence of the geometry was investigated a little bit further by increasing the gap space to examine its impact. For comparison simulations were conducted with 18*mm* FR gap space and with (P_S = 30) or without (P_S = 50) altered loop seal fluidization rates. Additionally, a simulation with 20*mm* FR gap space, with altered loop seal fluidization rates and P_S = 30 was conducted.

The simulation with P_S = 30 and increased loop seal fluidization rates predicted the best results in this study with a FR gap of 18*mm*, for the initial operating point. Increasing the gap even further led to overprediction of the mass flow rates and unstable conditions. The respective graphs are attached in the appendix (see Figure A.26 to Figure A.28). The simulation with the least alteration, only increasing the P_S value to 50 and an increased gap space to 18*mm*, underpredicted the mass flow rates, while achieving only slightly better pressure parameters compared to the simulation with normal geometry (*G14*). Therefore, the simulation with P_S = 50 predicts better results without geometrical modifications.

Therefore, the FR gap does clearly have a significant influence on the predicted results. A combination of adjusted P_S value with improved loop seal fluidization rates and adapted geometry could eventually achieve even better results in future studies.

Table 5.6: Outlook - results overview

		Mass Flow			Pressure Parameters in FR Column		Loop seal fluidization increased by 1.75
FR Gap	P_S $[Pa]$	AR $\left[\frac{kg}{h}\right]$	FR $\left[\frac{kg}{h}\right]$	ULS $\left[\frac{kg}{h}\right]$	P_{PP} $[mbar]$	P_{PG} $\left[\frac{bar^2}{m^2}\right]$	
18	30	821.4	911.8	816.5	17.19	0.00943	Yes
20	30	1086.5	1049.4	785.1	37.27	0.01949	Yes
18	50	609.0	644.0	744.3	25.7	0.01506	No

6 Discussion and summary

6.1 Problems

This section is for further discussion of results and problems witnessed during the simulation.

6.1.1 FR pressure profile

The pressure profile in the FR column differed from the measured values of the real experiment. The slope was either very steep or even going into the other direction than expected. Those observations are illustrated using simulation *G14* as an example. This trend was experienced in all simulations in different extent.

Figure 6.1a shows the pressure profile and the transient data points (#19 and #20 of Table 4.4) of interest circled, and with arrows indicating the location. Between those two points the reduced pressure difference of roughly 10*mbar* are contradictory to the measured values in the real cold flow model. The blue line represents the results predicted by simulation and the orange dashed line the real values of the real experiment.

Figure 6.1b shows the section of interest with the transient data points marked as white dots. Without the adjusted pressure limits both transient data points are in the green range of the color bar. With adjusted limits a region with higher pressure in the FR bubbling bed becomes visible with the transient data point located at its edge to lower pressure levels.

The cut-planes on Figure 6.1c-e also show the region with increased pressure. The high-pressure values in contradiction to the experiment could be a combination of generally higher measured pressure results in the simulation and a slightly misplaced transient data point, which does not match the real location exactly or is placed to near to the region of increasing pressure.

The zone of high pressure in the bottom part of the FR is clearly outlined and slight variations of location could lead to variations of 10*mbar* or more.

(a) Pressure Profile   (b) Adjusted limits

(c) xz-Plane and yz-Plane   (d) xz-Plane   (e) yz-Plane
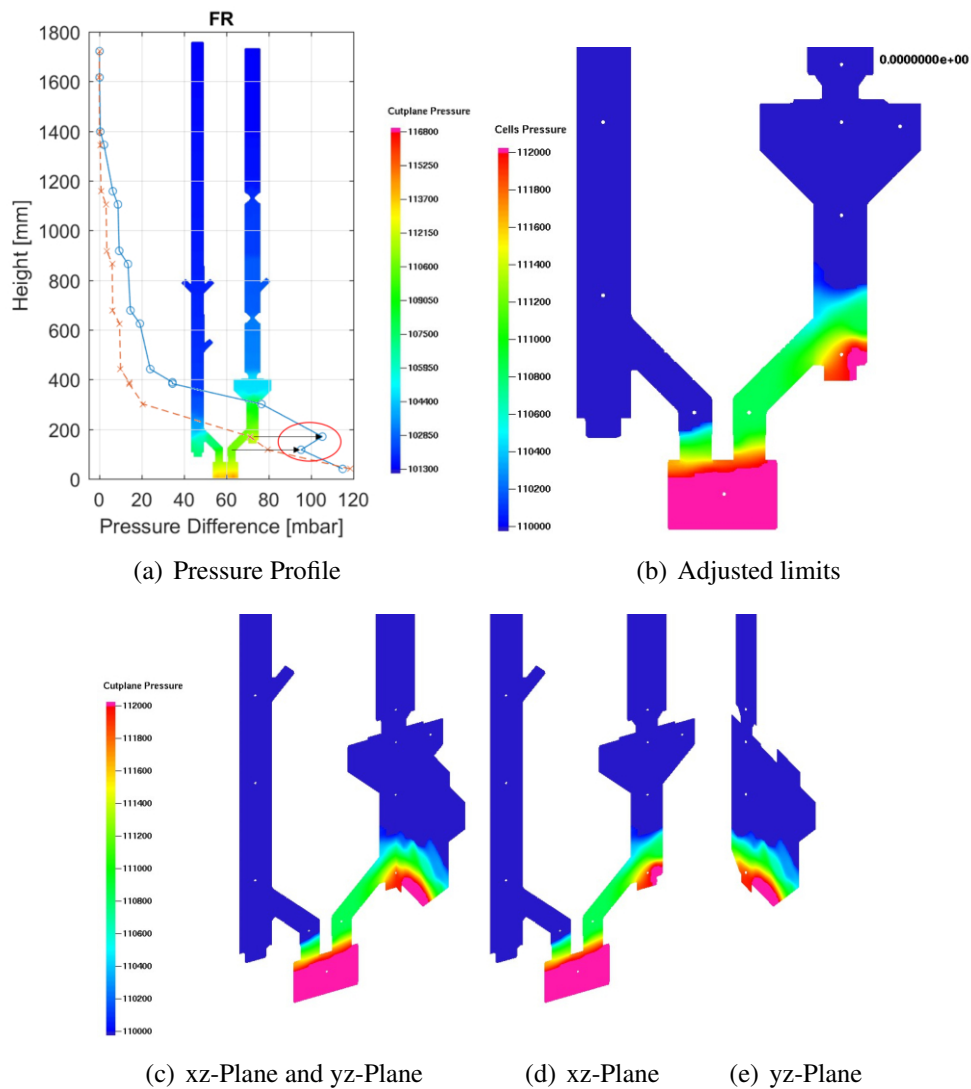
Figure 6.1: Pressure profile with misleading slope

6.1.2 EMMS drag law

The constants of the EMMS drag law were created using a certain model. An explanation for the bad results could be found by looking at the conditions this specific model was based on. The constants for the EMMS-Yang-2004 model, were generated for the following conditions: atmospheric pressure, $54\mu m$, particle density of $930^{kg}/_{m^3}$, fluid superficial velocity of $1.52\frac{m}{s}$ and solids flux of $14.3^{kg}/_{m^2s}$ [5]. The particle density and solid mass flux are significantly larger. The particle density is $8800^{kg}/_{m^3}$ while solid mass flux can be estimated for $823^{kg}/_h$ and a diameter of $52mm$ in the AR to roughly $\sim 107^{kg}/_{m^2s}$.

6.2 Summary

The goal of this work was to simulate a novel cold flow model for a biomass steam gasification process. The cold flow model was already used for several experiments and is located at TU Wien. Based on the data gained in the experiments mentioned earlier the simulation was modeled to predict defined operating points.

At the beginning of this work a literature research was conducted. In the literature research the three drag laws were rated as suitable for the simulation: the EMMS, the WYE and the Ganser drag law. First, a mesh sensitivity analysis was performed in which a mesh size of $500k$ cells was determined to be sufficient. In the next step, three different drag laws were tested and the Ganser drag law turned out to be the best option. Because of an unstable FR column and flooding of the AR SEP the geometry of the model was altered but ultimately the non-altered geometry was used, because the altered geometry was not necessary, based on the findings in this thesis. The particle normal stress was influenced by increasing the P_S value, a parameter for calculating of the particle normal stress, in order to reduce the number of particles in the FR column. A P_S value set to 30 and 50 significantly improved the performance compared to previous simulations. The mass flow rates of the simulation with $P_S = 30$ was still too low therefore the fluidization rates in the loop seals were increased to ensure that the loop seals were not the bottleneck of the particle mass flow. The target operating point was predicted better with increased loop seal fluidization rates than without. Both, $P_S = 30$ with increased loop seal fluidization rates, and $P_S = 50$ without increased loop seal fluidization rates were used to simulate other operating points. It turned out that overall the simulation with $P_S = 50$ and normal loop seal fluidization rates predicted the operating points better than the simulation with $P_S = 30$ and increased loop seal fluidization rates. Therefore, a mesh size of $500k$ real cells, Ganser as a drag law and P_S value of 50 were the best settings for the simulations and are also recommended for further investigations.

6.3 Results

In this thesis the simulation with default settings from early stages (e.g. simulation *G3*) was improved significantly and the settings were even transferable to other operating points. The research questions are repeated and subsequently answered with the findings of this thesis in this section.

How do the different settings in the CPFD software influence the particle behavior?

The most important settings for the simulations are the drag law and the P_S constant. Especially the particle normal stress played a significant role to achieve a steady state behavior, reduce bed heights in the FR column, and reach proper bed material circulation rates. Additionally the loop seal fluidization rate was inspected.

The Ganser drag law achieved the best performance of all tested drag laws. WYE seems to overestimate the drag force in the riser, leading to increased particle recirculation rates, as already experienced by Adkins et al. and Liu et al. [48, 53], compared to Ganser, which results in unsteady behavior due to diverging mass flows. The EMMS drag law underpredicted the circulation rate. The pressure values measured in the FR column were generally smaller than those of Ganser and WYE. That resulted in partially better (E1, E3) and in one case a worse (E2) pressure profile and gradients using the EMMS drag law compared to Ganser. The overall performance with EMMS was not sufficient.

The increased P_S value influenced the bed heights in the FR column and the mass flow in the system. Depending on the simulation this led to pressure profiles closer to the real case and increased particle circulation rates approaching the target value of $823^{kg}/_h$ in the initial case. Increasing the P_S too much led to accumulation of particles in the upper part of the FR column and therefore a behavior not comparable to the real case.

The loop seal fluidization rate influenced the particle mass flow rates noticeable. In contrast to the real case, the particle circulation rate in the simulation was increased significantly with raised LLS fluidization rates over $0.8^{Nm^3}/_h$. Additionally, the assumption to increase the loop seal fluidization rate by the same factor as the u_{mf} is underpredicted is most likely a coincidence. A u_{mf} value of the same magnitude was achieved with $P_S = 30$ as with $P_S = 50$ but the latter achieved sufficient circulation rates without increased loop seal fluidization rates. Nevertheless, good results were achieved by adjusting the loop seal fluidization rates and even different operating points were predicted well.

What measures lead to the best performance compared to the real cold flow model at a specific operating point? Do the optimal settings predict reliable results at different operating points in the same system?

On the one hand very good results, compared to simulations without adjustments, were achieved with the settings P_S = 30 in combination with increased air flow in the loop seals to ensure proper fluidization and on the other hand increasing only the P_S to 50 without altering the loop seal fluidization rates. Both scenarios showed promising results with three different operating points predicted sufficiently.

The cases with P_S = 50 and regular loop seal fluidization rates are favored over the other cases because of the non-altered operating conditions, better pressure profiles and smaller deviation of the particle circulation rate over all cases. Therefore, it is possible to achieve a good performance by adjusting the P_S value without geometrical modifications or altering the conditions.

As a result, the setup with only an adjusted P_S value to $50Pa$ is the best case in this thesis and is also recommended as the starting point for further investigation and optimization of the process.

Appendix

Transient data plots

Simulations in this section: all (E1 to W4)
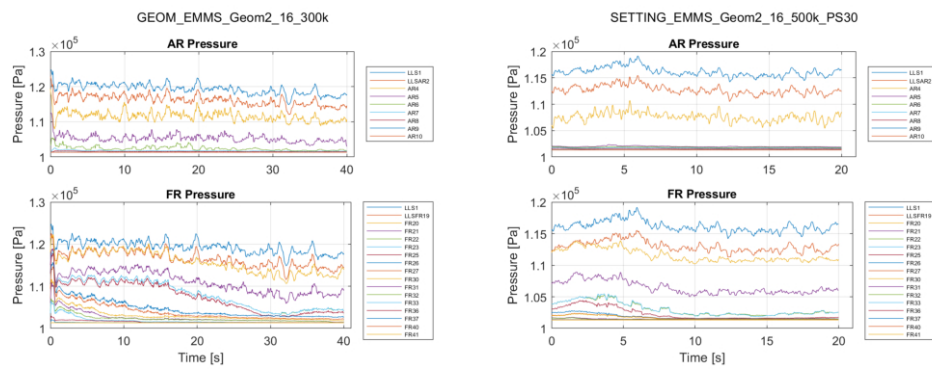
(a) E1

(b) E2
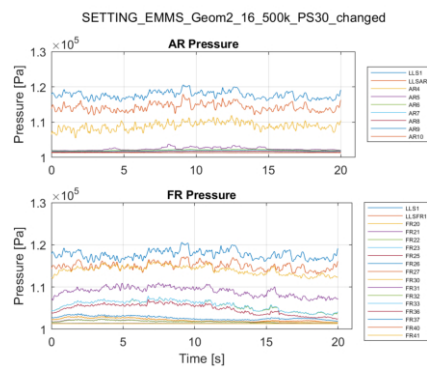
(c) E3

Figure A.1: Transient data plots - EMMS
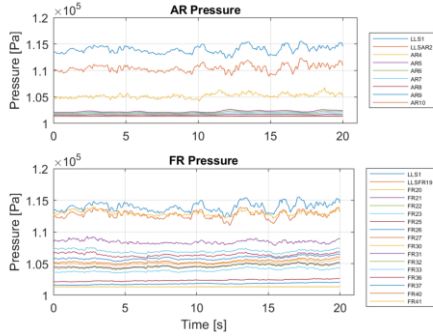
(a) G1

(b) G2

(c) G3

(d) G4

(e) G5
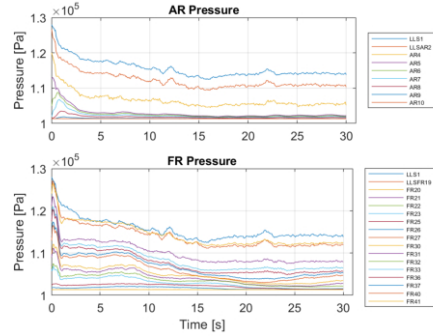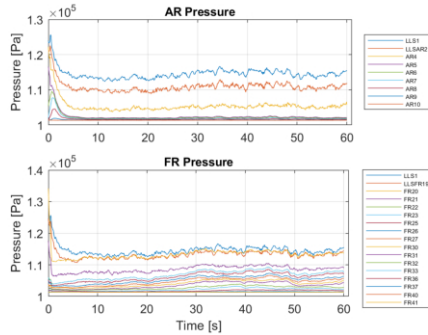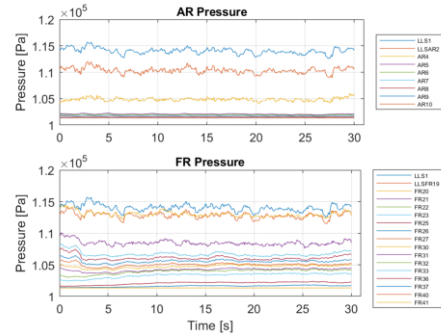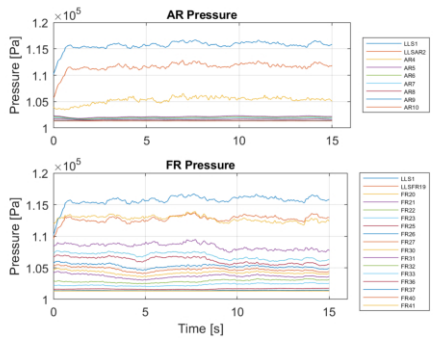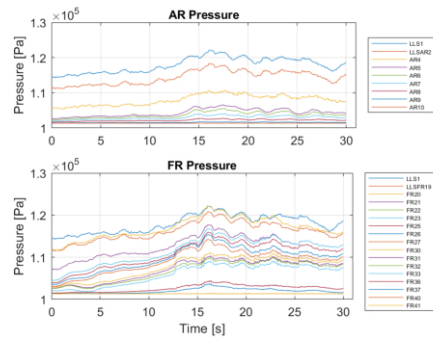
(f) G6
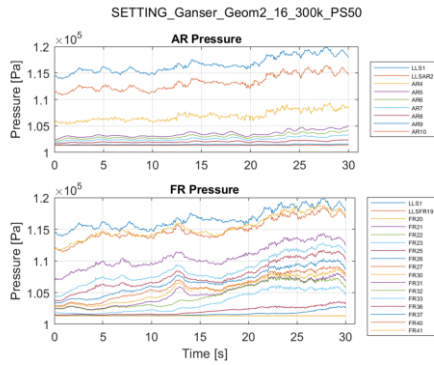
(g) G7
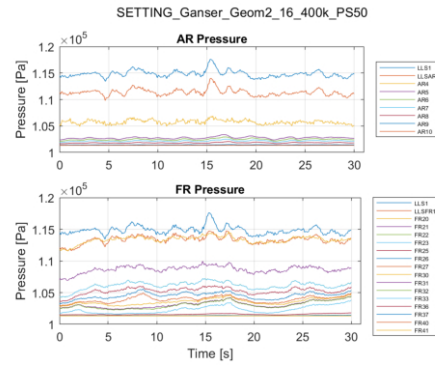
(h) G8
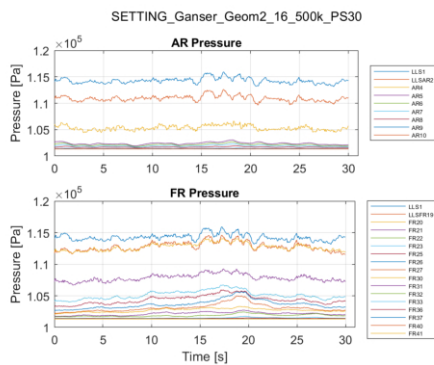
(i) G9
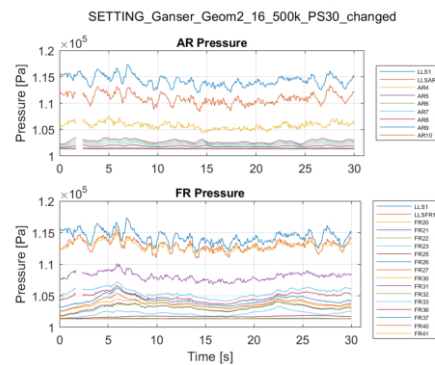
(j) G10
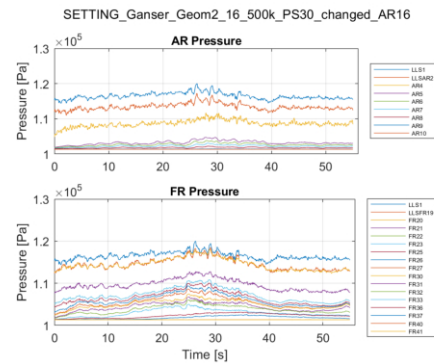
(k) G11
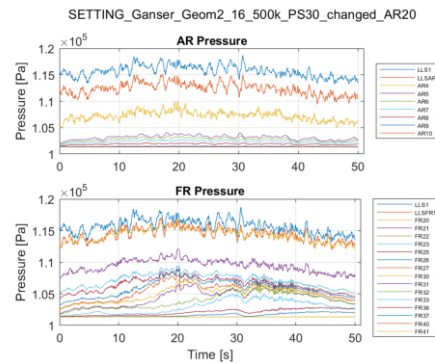
(l) G12
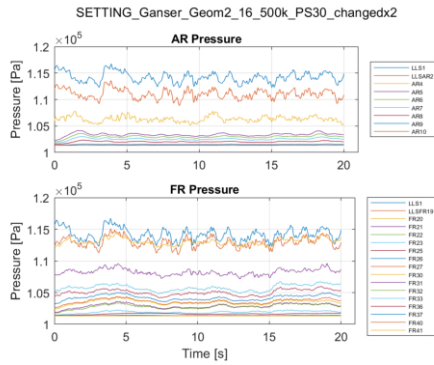
(m) G13
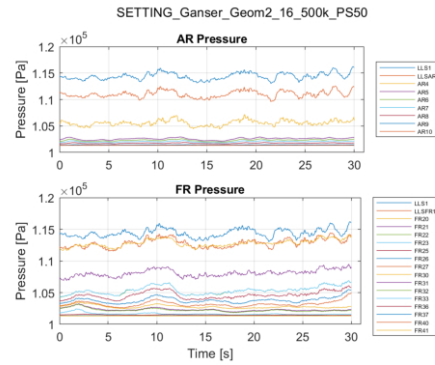
(n) G14
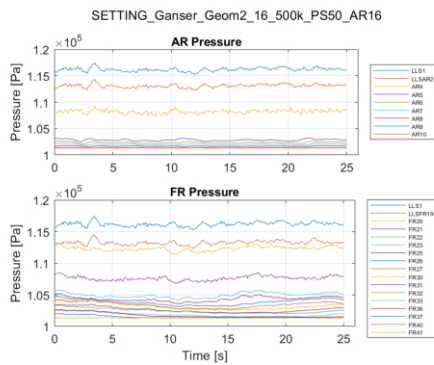
(o) G15
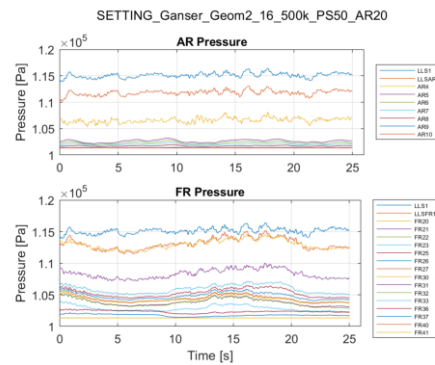
(p) G16
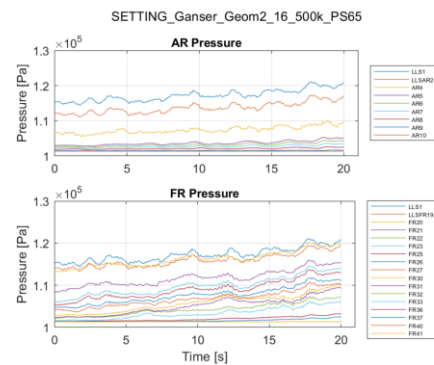
(q) G17
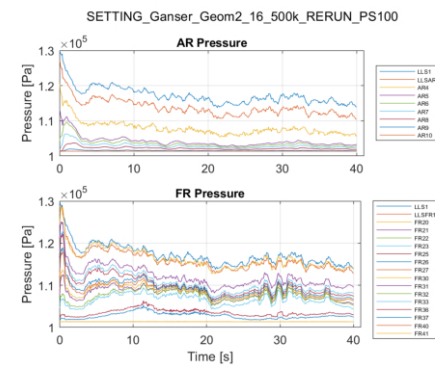
(r) G18
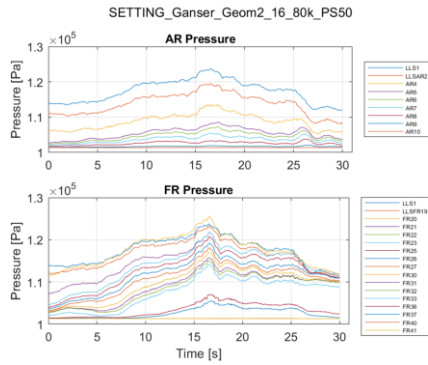
(s) G19
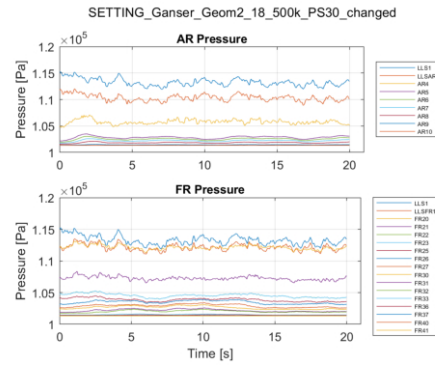
(t) G20
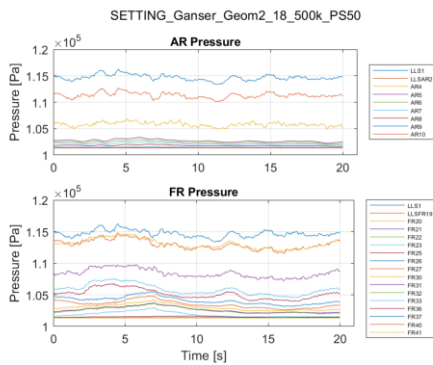
(u) G21

(v) G22

(w) G23

(x) G24

(y) G25 (z) G26
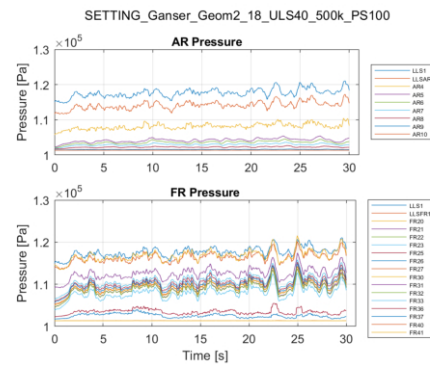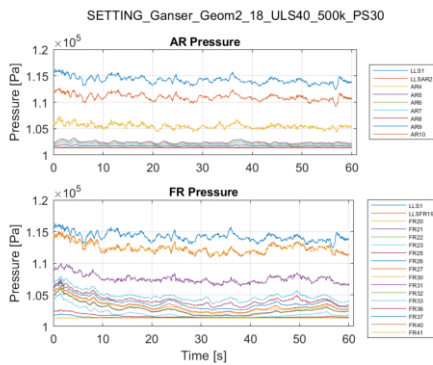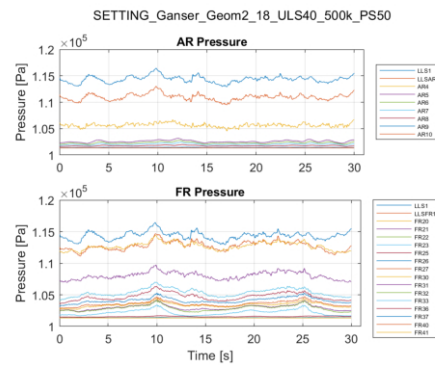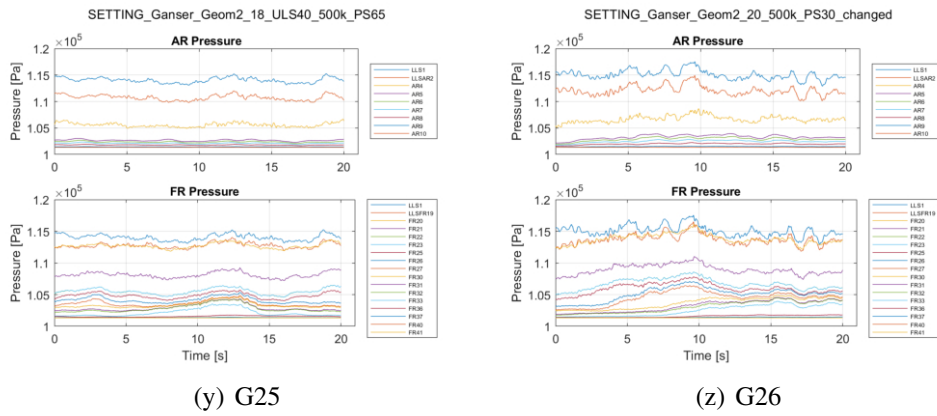
Figure A.2: Transient data plots - Ganser

(a) W1 (b) W2

(c) W3 (d) W4
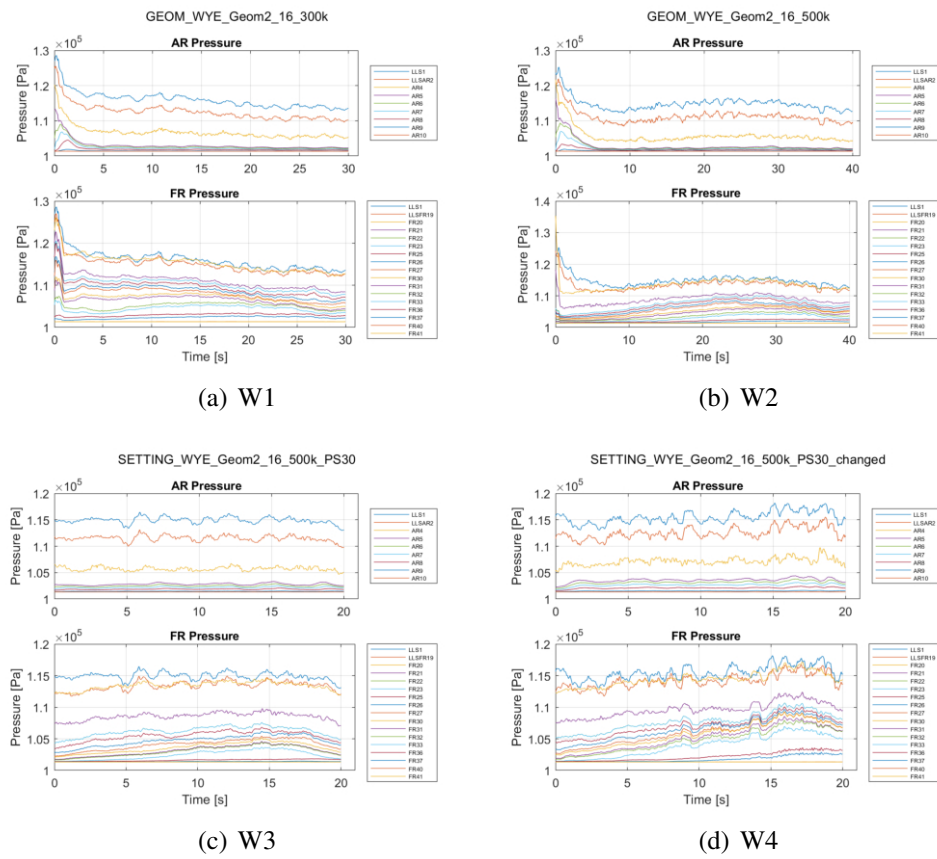
Figure A.3: Transient data plots - WYE

Mesh sensitivity

Simulations in this section: G6, G7, G8, G19

(a) Mass difference

(b) Total mass

(c) Pressure profile

(d) Pressure gradient
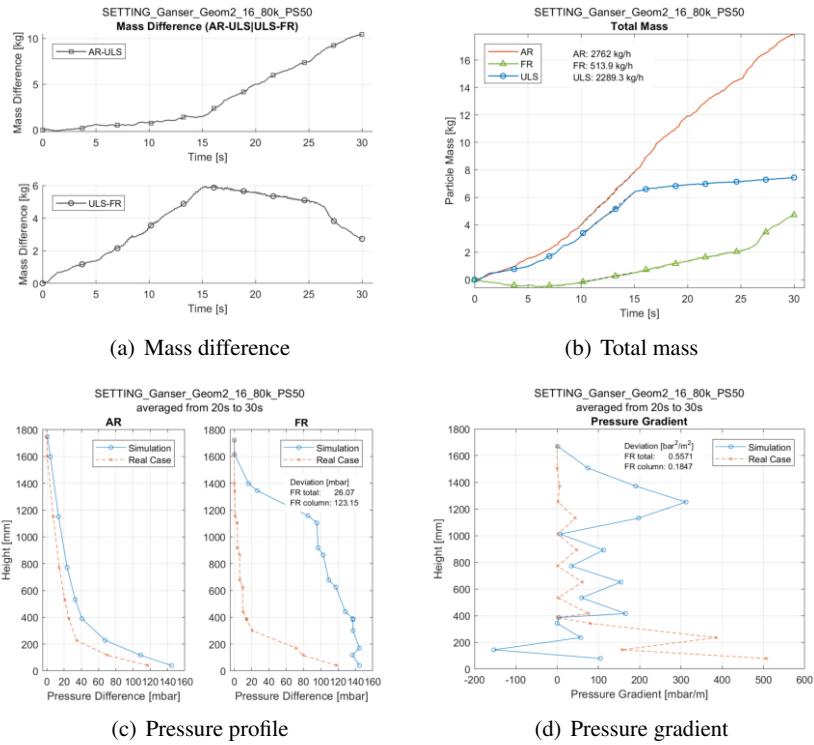
Figure A.4: Mesh sensitivity 80*k* - *G19*

(a) Mass difference

(b) Total mass

(c) Pressure profile

(d) Pressure gradient
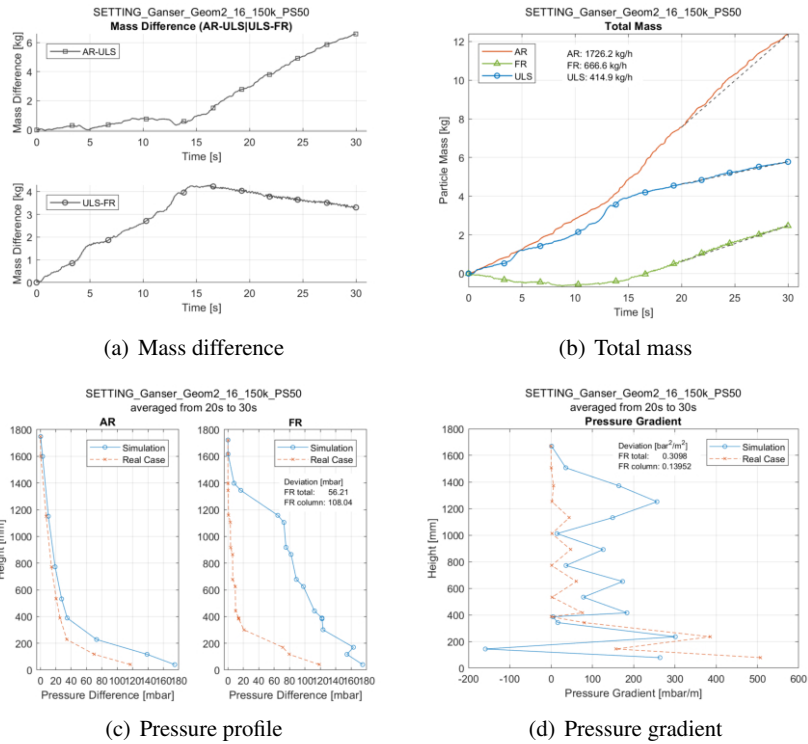
Figure A.5: Mesh sensitivity 150*k* - *G6*

(a) Mass difference

(b) Total mass

(c) Pressure profile

(d) Pressure gradient
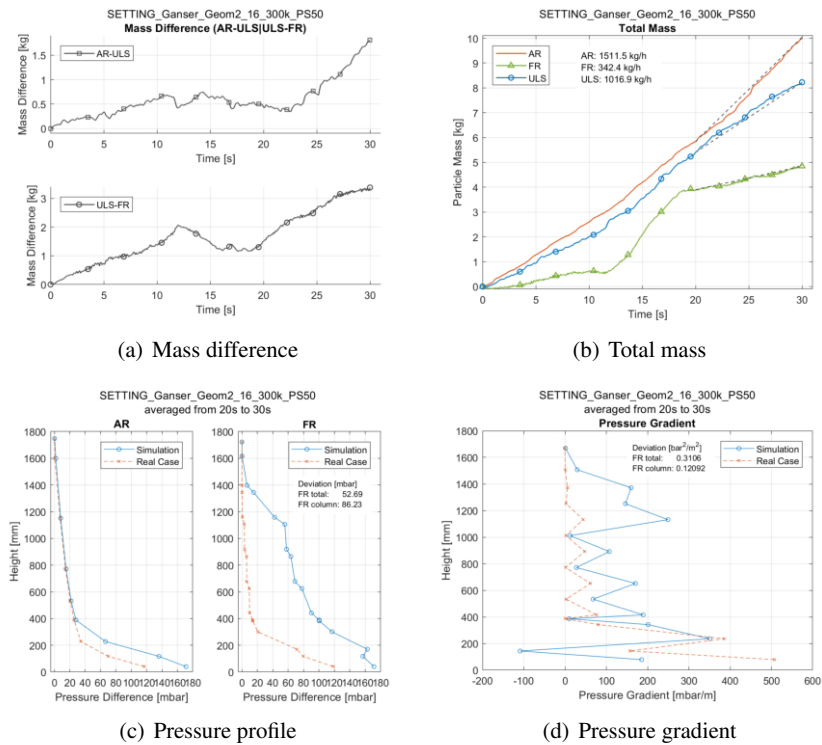
Figure A.6: Mesh sensitivity 300*k* - *G7*
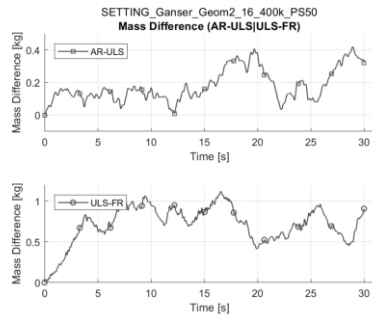
(a) Mass difference
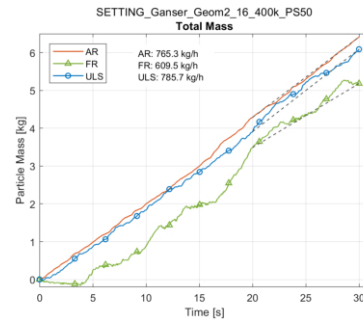
(b) Total mass
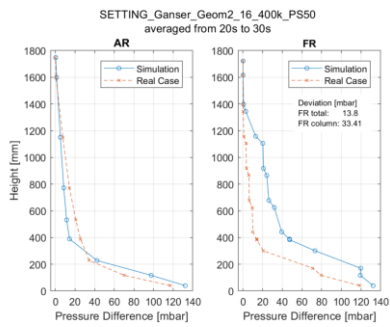
(c) Pressure profile
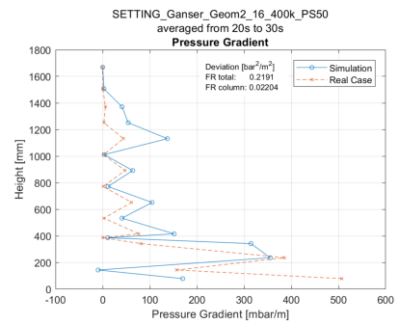
(d) Pressure gradient

Figure A.7: Mesh sensitivity 400*k* - *G8*

Mesh sensitivity results

Table A.1: Mesh sensitivity - results overview

| cell number | Mass Flow | | | Pressure Parameters in FR Column | | Time for averaging | |
	AR $\left[\frac{kg}{h}\right]$	FR $\left[\frac{kg}{h}\right]$	ULS $\left[\frac{kg}{h}\right]$	Pressure Profile [$mbar$]	Pressure Gradient $\left[\frac{bar^2}{m^2}\right]$	Start [s]	End [s]
80k	2762.0	513.9	2289.3	127.08	0.17068	10	15
150k	1726.2	666.6	414.9	108.04	0.13952	20	30
300k	1511.5	342.4	1016.9	86.23	0.12092	20	30
400k	765.3	609.5	785.7	33.41	0.02204	20	30
500k	742.0	534.8	694.7	30.28	0.01944	20	30

Pressure difference over velocity - u_{mf}
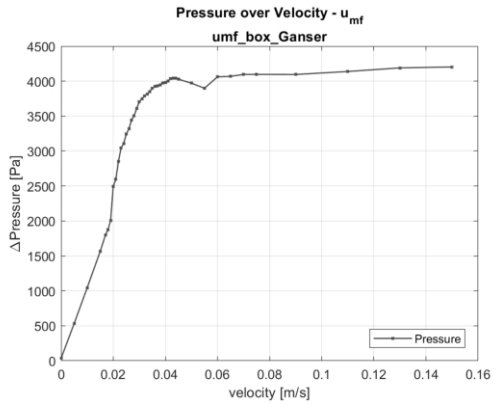
(a) u_{mf} with $P_S = 1Pa$
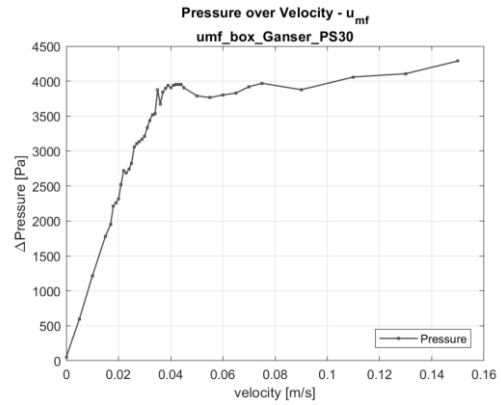
(b) u_{mf} with $P_S = 30Pa$
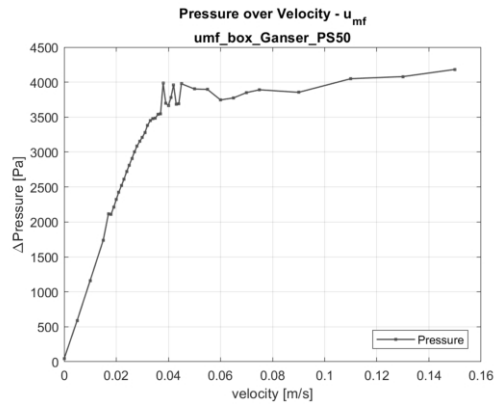
(c) u_{mf} with $P_S = 50Pa$

Figure A.8: Minimum fluidization velocity - Ganser

(a) u_{mf} with $P_S = 1Pa$

(b) u_{mf} with $P_S = 30Pa$
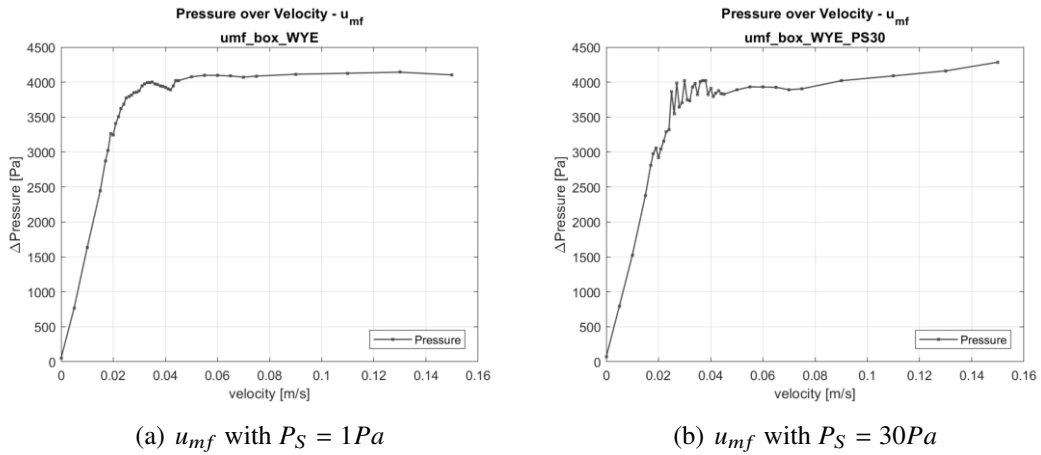
Figure A.9: Minimum fluidization velocity - WYE

(a) u_{mf} with $P_S = 1Pa$

(b) u_{mf} with $P_S = 30Pa$
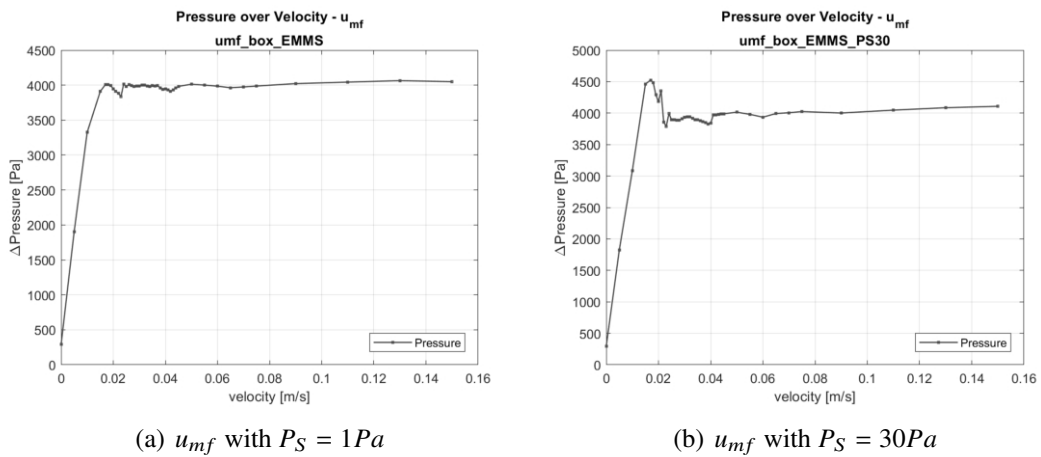
Figure A.10: Minimum fluidization velocity - EMMS

Choosing the drag law

300k

Table A.2: 300k - results overview

Drag Law	Mass Flow			Pressure Parameters in FR Column	
	AR $\left[\frac{kg}{h}\right]$	FR $\left[\frac{kg}{h}\right]$	ULS $\left[\frac{kg}{h}\right]$	P_{PP} [$mbar$]	P_{PG} $\left[\frac{bar^2}{m^2}\right]$
EMMS	72.0	890.6	116.8	33.93	0.02296
Ganser	392.1	233.9	391.1	35.95	0.02426
WYE	509.8	605.6	319.8	57.40	0.04200

500k

Table A.3: 500k - results overview

Drag Law	Mass Flow			Pressure Parameters in FR Column	
	AR $\left[\frac{kg}{h}\right]$	FR $\left[\frac{kg}{h}\right]$	ULS $\left[\frac{kg}{h}\right]$	P_{PP} [$mbar$]	P_{PG} $\left[\frac{bar^2}{m^2}\right]$
Ganser	502.3	193.6	329.8	53.56	0.03207
WYE	518.3	613.5	309.1	50.38	0.02873

Varying P_S

Table A.4: PS variation - result overview

P_S [Pa]	Geometry	Mass Flow			Pressure Parameters in FR Column	
		AR $\left[\frac{kg}{h}\right]$	FR $\left[\frac{kg}{h}\right]$	ULS $\left[\frac{kg}{h}\right]$	P_{PP} [mbar]	P_{PG} $\left[\frac{bar^2}{m^2}\right]$
1	normal	420.2	187.1	336.3	46.94	0.02895
	altered	346.0	81.6	368.1	39.04	0.02449
30	normal	506.9	727.9	504.0	22.04	0.01263
	altered	501.8	704.4	495.2	17.60	0.00928
50	normal	742.0	534.8	694.7	30.28	0.01944
	altered	657.5	747.3	660.5	27.79	0.01654
65	normal	1866.2	662.9	1271.8	88.73	0.08610
	altered	687.4	644.1	722.7	29.11	0.01695
100	normal	1129.0	1207.4	1268.6	63.57	0.05700
	altered	1635.8	1315.6	1566.5	90.58	0.14209

P_S set to 65

Simulations in this section: G17, G25

The simulation with non-altered geometry seems to be the one outlier in this section with altered P_S values, based on the diverging mass flow rates and the big P_{PG} parameter. The latter is mainly because of the poor performance in the upper part of the FR column. The P_{PG} value is calculated summing up the squared deviation of the pressure gradient and as pictured in Figure A.11b the deviation is significant resulting in an even bigger impact when squared. The mass balance of the AR SEP improved due to converging AR and ULS particle mass flow rates but the mass flow rates are too high, while the FR mass flow is significantly lower and closer to the target value of $823^{kg}/_h$.

The simulation with altered geometry follows the trend, that the altered geometry scores better results while increasing the mass flow with bigger P_S values.

(a) Total mass
(b) Pressure gradient
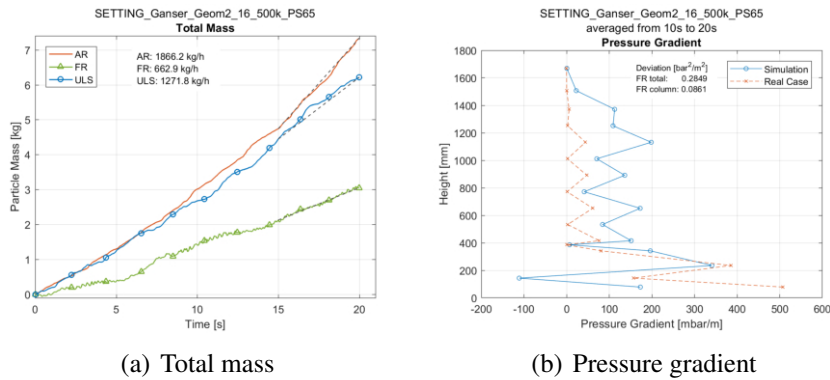
Figure A.11: $P_S = 65$ without altered geometry - *G17*

(a) Total mass
(b) Pressure gradient
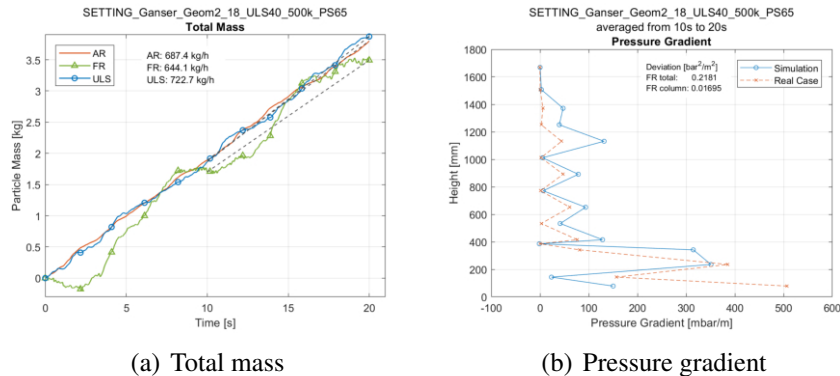
Figure A.12: $P_S = 65$ with altered geometry - *G25*

Varying P_S additional graphs

Simulations in this section: G9, G14, G17, G18, G22, G23, G24, G25
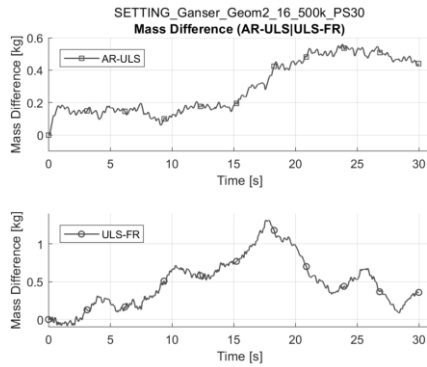
(a) Mass difference
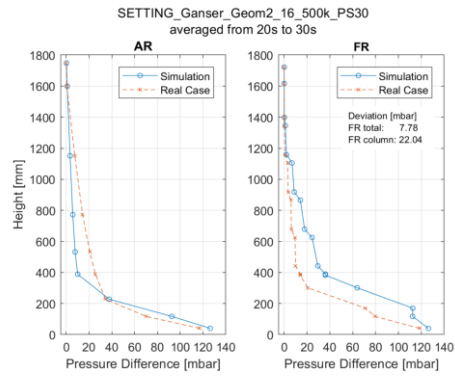
(b) Pressure profile

Figure A.13: $P_S = 30$ without altered geometry - *G9*
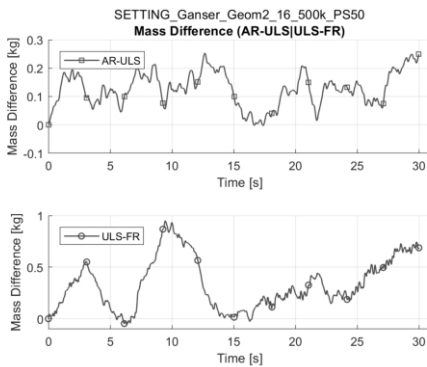
(a) Mass difference
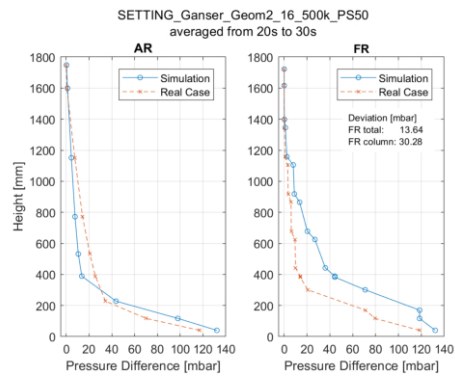
(b) Pressure profile

Figure A.14: $P_S = 50$ without altered geometry - *G14*
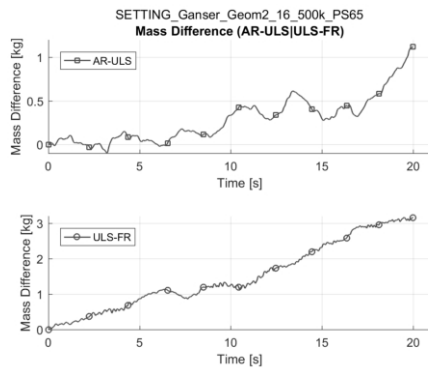
(a) Mass difference
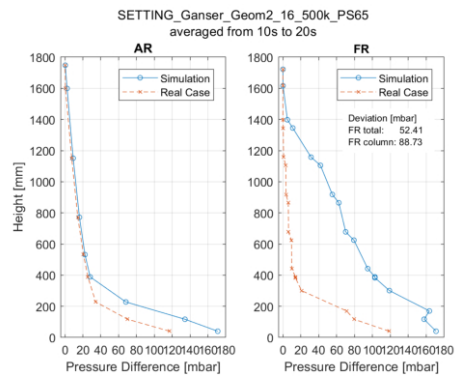
(b) Pressure profile

Figure A.15: $P_S = 65$ without altered geometry - *G17*
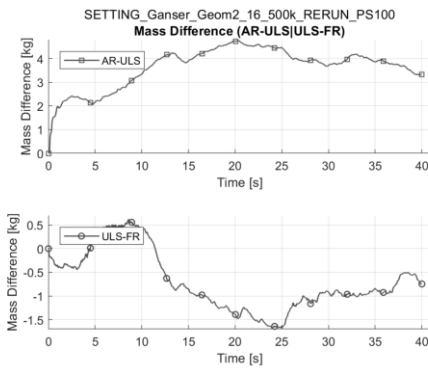
(a) Mass difference
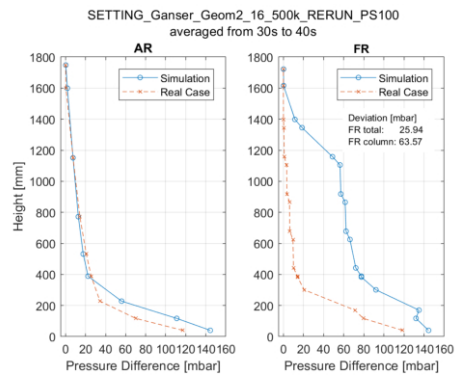
(b) Pressure profile

Figure A.16: $P_S = 100$ without altered geometry - *G18*
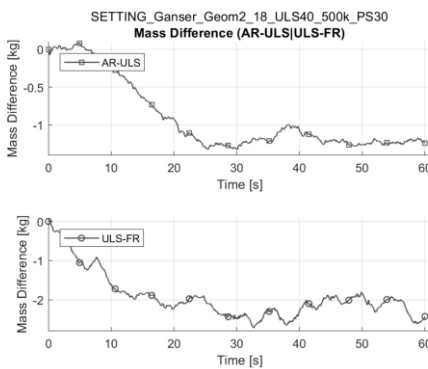
(a) Mass difference
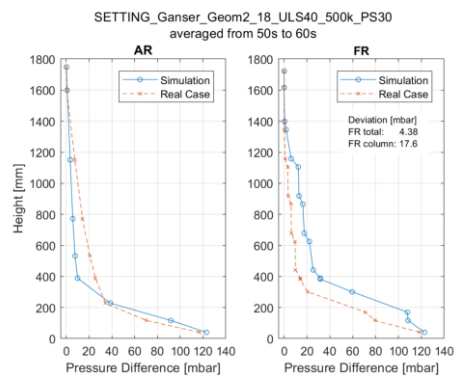
(b) Pressure profile

Figure A.17: $P_S = 30$ with altered geometry - *G23*

(a) Mass difference

(b) Pressure profile
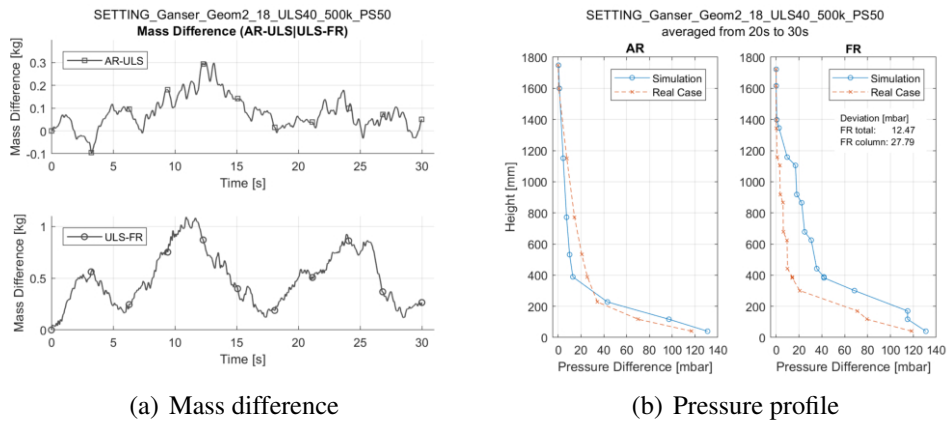
Figure A.18: P_S = 50 with altered geometry - *G24*

(a) Mass difference

(b) Pressure profile
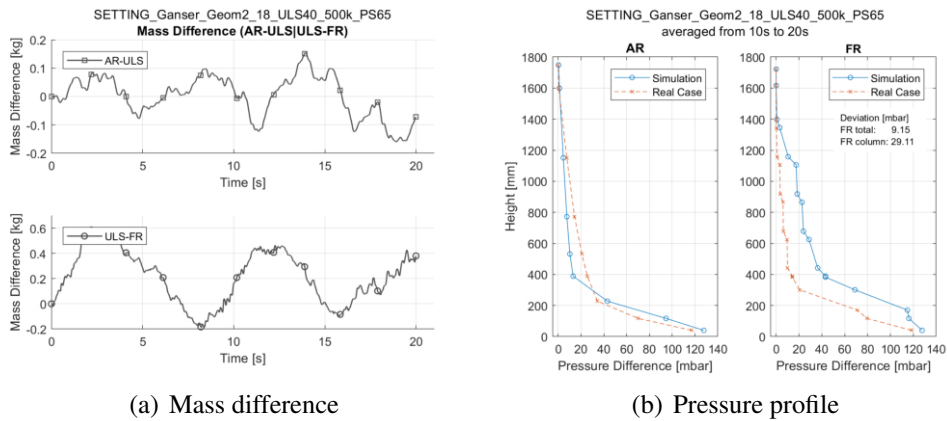
Figure A.19: P_S = 65 with altered geometry - *G25*

(a) Mass difference

(b) Pressure profile
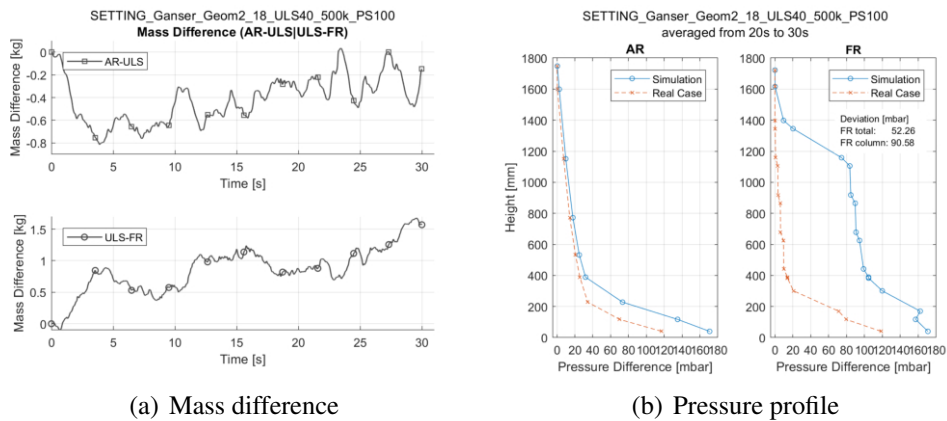
Figure A.20: P_S = 100 with altered geometry - *G22*

Loop seal fluidization

Simulations in this section: G1

(a) Mass difference

(b) Total mass

(c) Pressure Profile

(d) Pressure Gradient
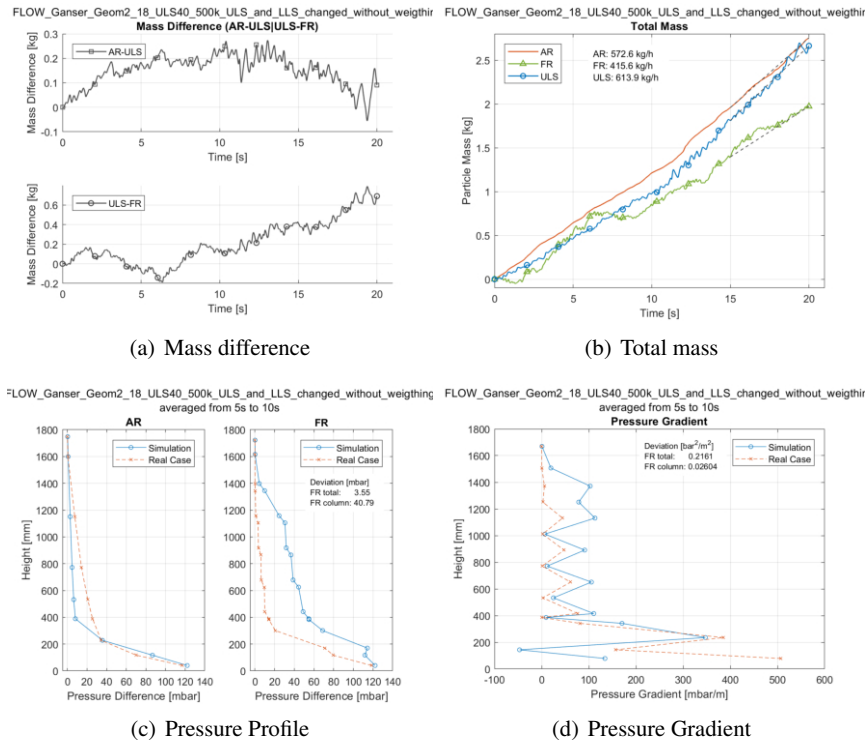
Figure A.21: Loop seal fluidization varied, altered Geometry - *G1*

Table A.5: Overview with different P_S, drag law and loop seal fluidization

Drag Law	P_S [Pa]	Loop seal fluidization	Mass Flow			Pressure Parameters in FR Column	
			AR $\left[\frac{kg}{h}\right]$	FR $\left[\frac{kg}{h}\right]$	ULS $\left[\frac{kg}{h}\right]$	P_{PP} [mbar]	P_{PG} $\left[\frac{bar^2}{m^2}\right]$
Ganser	1	normal	420.2	187.1	336.3	46.94	0.02895
Ganser	30	normal	506.9	727.9	504.0	22.04	0.01263
Ganser	30	increased by 1.75	827.9	412.3	658.9	30.58	0.02170
Ganser	30	increased by 2.5	1145.8	1051.4	827.5	31.42	0.02997
WYE	1	normal	518.3	613.5	309.1	50.38	0.02873
WYE	30	normal	878.9	750.4	563.4	39.09	0.02357
WYE	30	increased by 1.75	1385.1	646.5	803.3	62.12	0.05991
EMMS	30	normal	240.2	198.8	237.3	4.64	0.00788
EMMS	30	increased by 1.75	307.7	780.3	334.7	21.42	0.03132

Varying drag law

Simulations in this section: E2, E3, W3, W4
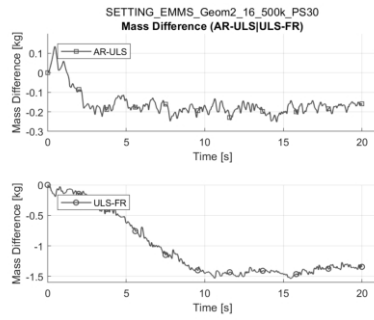
(a) Mass difference
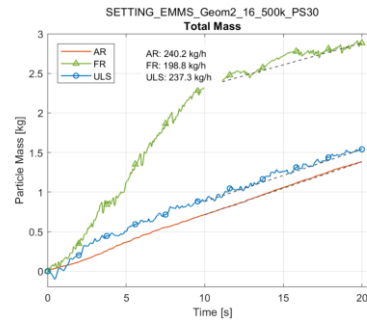
(b) Total mass
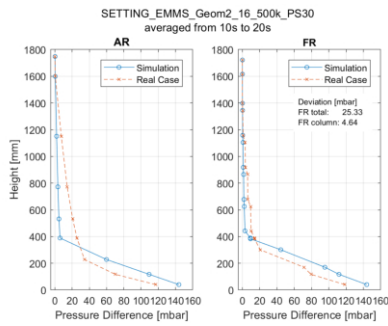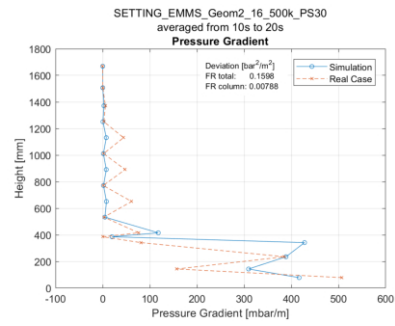
(c) Pressure profile

(d) Pressure gradient

Figure A.22: EMMS drag law, normal fluidization with $P_S = 30$ - *E2*

(a) Mass difference

(b) Total mass

(c) Pressure profile

(d) Pressure gradient
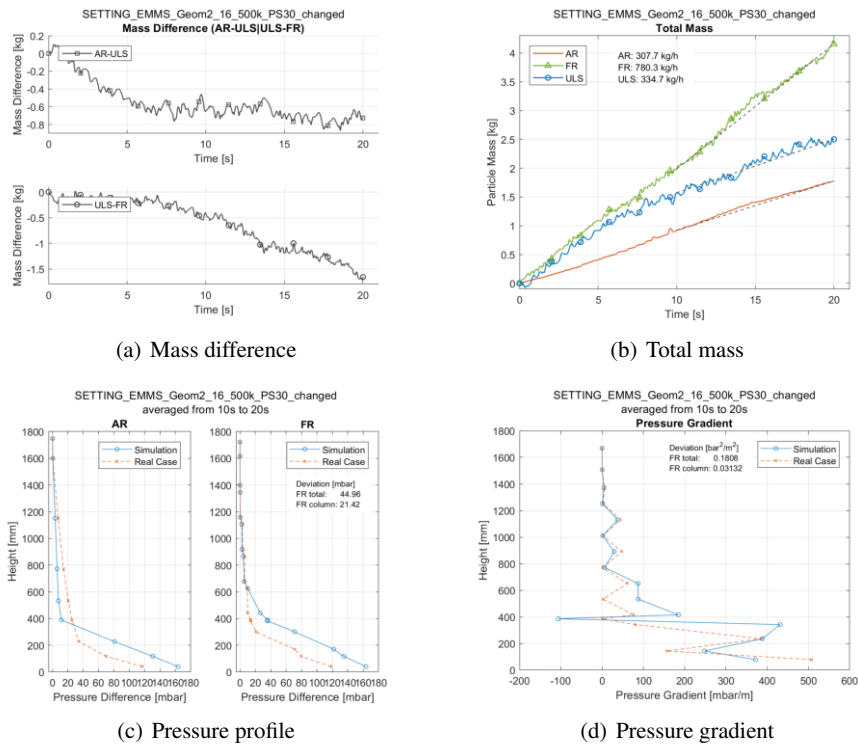
Figure A.23: EMMS drag law, increased fluidization with P_S = 30 - *E3*

(a) Mass difference

(b) Total mass

(c) Pressure profile

(d) Pressure gradient
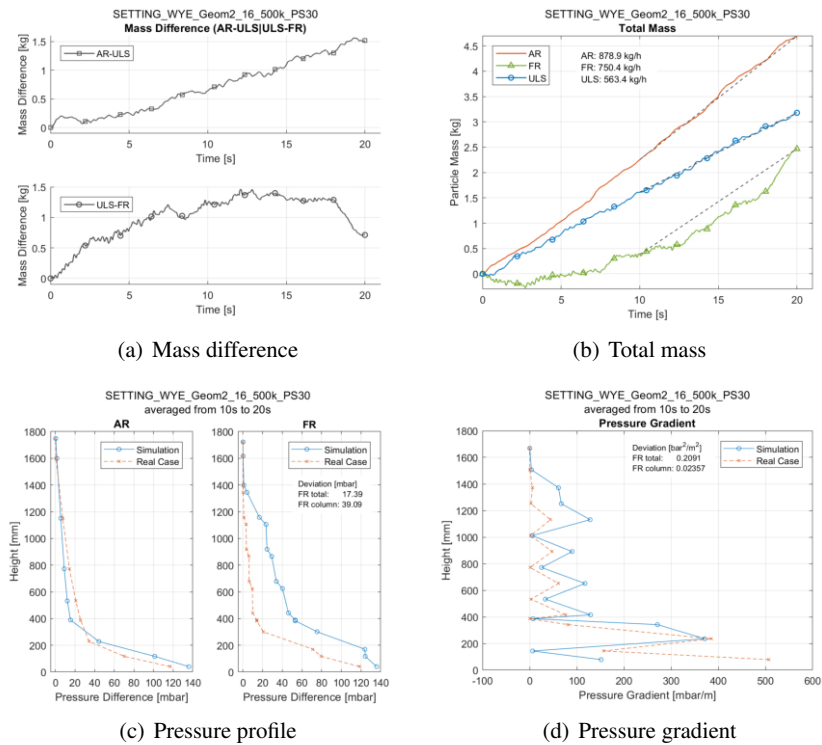
Figure A.24: WYE drag law, normal fluidization with P_S = 30 - *W3*
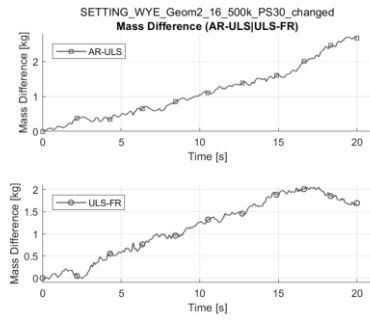
(a) Mass difference
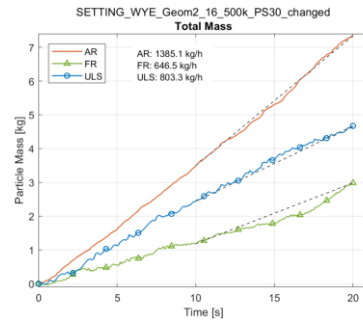
(b) Total mass
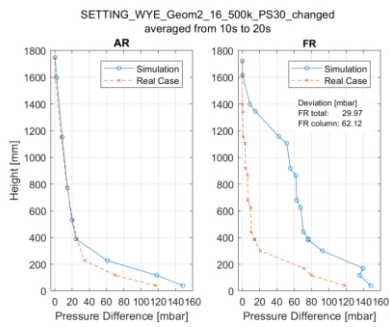
(c) Pressure profile
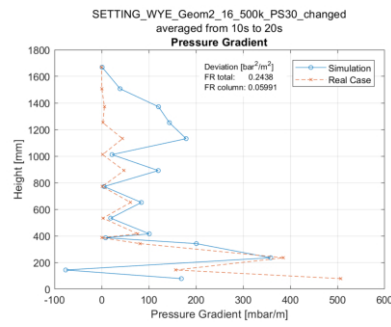
(d) Pressure gradient

Figure A.25: WYE drag law, increased fluidization with $P_S = 30$ - *W4*

AR fluidization - different operating points

Table A.6: AR fluidization - overview

AR Fluidization $\left[\frac{Nm^3}{h}\right]$	P_S [Pa]	Mass Flow			Pressure Parameters in FR Column		Loop seal fluidization increased 1.75 times
		AR $\left[\frac{kg}{h}\right]$	FR $\left[\frac{kg}{h}\right]$	ULS $\left[\frac{kg}{h}\right]$	P_{PP} [mbar]	P_{PG} $\left[\frac{bar^2}{m^2}\right]$	
16	30	379.9	393.3	342.6	21.39	0.01745	Yes
	50	275.8	171.9	264.8	18.69	0.00493	No
20	30	601.6	812.5	632.4	15.24	0.04891	Yes
	50	540.1	710.5	545.3	16.84	0.03449	No
24	30	827.9	412.3	658.9	30.58	0.02170	Yes
	50	742.0	534.8	694.7	30.28	0.01944	No

Outlook

Simulations in this section: G20, G21, G26

(a) Mass difference

(b) Total mass

(c) Pressure profile

(d) Pressure gradient
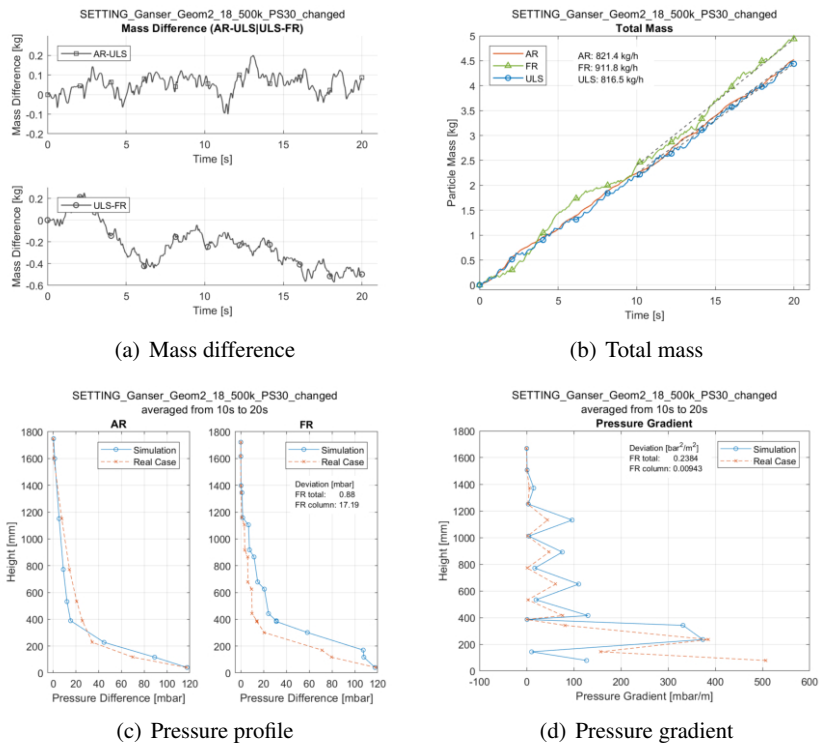
Figure A.26: P_S = 30, increased loop seal fluidization, and FR gap 18*mm* - *G20*

(a) Mass difference

(b) Total mass

(c) Pressure profile

(d) Pressure gradient
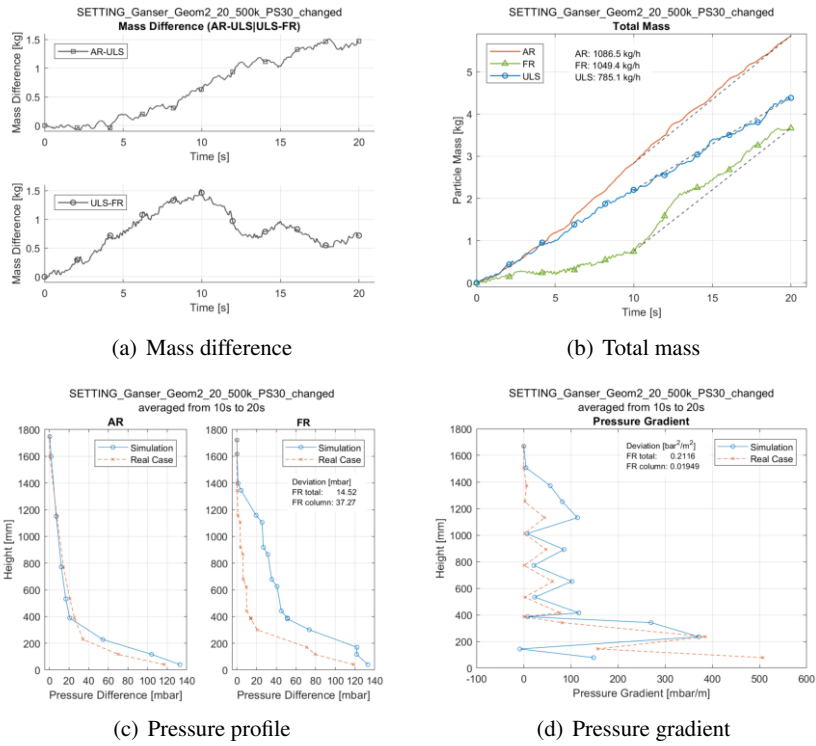
Figure A.27: $P_S = 30$, increased loop seal fluidization, and FR gap 20*mm* - *G26*

(a) Mass difference

(b) Total mass

(c) Pressure profile

(d) Pressure gradient
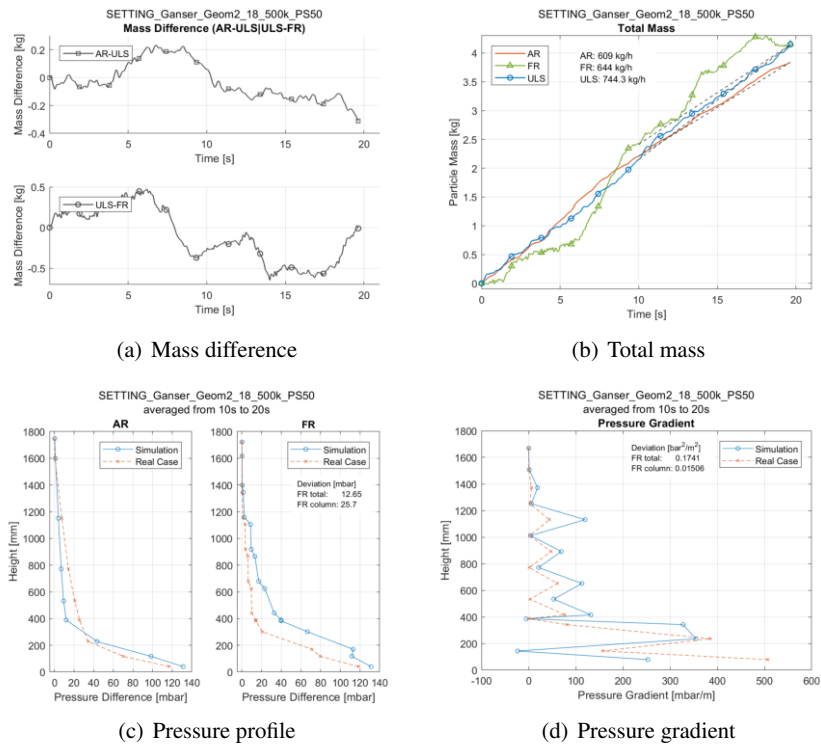
Figure A.28: $P_S = 50$, normal loop seal fluidization, and FR gap 18*mm* - *G21*

Nomenclature

symbol	meaning	SI unit
$\boldsymbol{a}_p$	particle acceleration	m/s^2
A_p	surface area of particle	m^2
C_d	drag coefficient	-
C_s	Smagorinsky constant	-
D	drag function	$1/s$
d_{sv}	Sauter diameter	m
d_p^*	dimensionless particle diameter	-
$\boldsymbol{F}$	momentum exchange rate	N/m^3
$\boldsymbol{F}_b$	buoyancy force	N
$\boldsymbol{F}_d$	drag force	N
$\boldsymbol{F}_g$	gravity force	N
$\boldsymbol{g}$	gravitational acceleration	m/s^2
$M_{-1,3}$	-1st momentum of $q_3(x)$	$1/m$
m_p	mass of particle	kg
p	fluid pressure	Pa
P_S	constant for τ_p	Pa
$q_3(x)$	volume distribution density	-
R	universal gas constant	$J/mol*K$
Re_p	particle Reynolds number	-
S_{ij}	strain rate tensor	$1/s$
S_V	volume specific area	$1/m$
t	time	s
Δt	time step	s
$\boldsymbol{u}_f$	fluid velocity	m/s
$\boldsymbol{u}_p$	particle velocity	m/s
u_t	terminal velocity of particle	m/s
u_0^*	dimensionless superficial velocity	m/s
V_p	volume of particle	m^3
$\boldsymbol{x}$	particle position	m
Δx_{cell}	cell dimension	m
x_i	spatial variable	m
x_p	particle size	m

Greek letters

symbol	meaning	SI unit
Δ	filter length scale	m
ε_p	particle volume fraction	-
ε_f	fluid volume fraction	-
ε_{cp}	particle volume fraction at close pack	-
μ_f	dynamic viscosity of fluid	$kg/m*s$
μ_t	turbulent viscosity of fluid	$kg/m*s$
∇	nabla operator	m^{-1}
ρ_f	fluid density	kg/m^3
ρ_p	density of particle	kg/m^3
τ_p	particle normal stress	N/m^2

Abbreviations

abbreviation	meaning
AR	air reactor
BB	bubbling bed
BC	boundary condition
CFB	circulating fluidized bed
CFD	computational fluid dynamics
CPFD	computational particle fluid dynamics
DEM	discrete element method
DNS	direct numerical solution
e.g.	exempli gratia
etc.	et cetera
EMMS	energy-minimization multi- scale (EMMS drag model)
Eq.	equation
FR	fuel reactor
Ganser	non-spherical Ganser (Ganser drag model)
HDPE	high density polyethylene
IC	initial condition
ILS	inner loop seal
LES	large eddy simulation
LLS	lower loop seal
MP-PIC	multi phase particle in cell
PSD	particle size distribution
SEP	separator
SGS	Smagorinsky subgrid scale
ULS	upper loop seal
WYE	Wen-Yu and Ergun (WYE drag model)

List of Figures

List of Tables

Bibliography

[1] J. Tu, G. H. Yeoh, and C. Liu, *Computational fluid dynamics: a practical approach*. Butterworth-Heinemann, 1st ed., 2008.

[2] J. C. Schmid, *Development of a novel dual fluidized bed gasification system for increased fuel flexibility*. PhD thesis, Vienna University of Technology, 2014.

[3] ISO and DIN, "9276-2: Darstellung der Ergebnisse von Partikelgrößenanalysen–Teil 2: Berechnung von mittleren Partikelgrößen/-durchmessern und Momenten aus Partikelgrößenverteilungen," tech. rep., 2018.

[4] H. Brenner, A. Acrivos, J. E. Bailey, L.-s. Fan, D. Kunii, and O. Levenspiel, *Fluidization engineering*, vol. 1. 1994.

[5] CPFD Software LLC., "Barracuda Virtual Reactor User Manual," 2018.

[6] N. Yang, W. Wang, W. Ge, L. Wang, and J. Li, "Simulation of heterogeneous structure in a circulating fluidized-bed riser by combining the two-fluid model with the EMMS approach," *Industrial and Engineering Chemistry Research*, vol. 43, no. 18, pp. 5548–5561, 2004.

[7] R. P. Chhabra, L. Agarwal, and N. K. Sinha, "Drag on non-spherical particles: An evaluation of available methods," *Powder Technology*, vol. 101, no. 3, pp. 288–295, 1999.

[8] C. Y. Wen and Y. H. Yu, "Mechanics of fluidization," *Chemical Engineering Progress, Symposium Series*, vol. 62, no. 1, pp. 100–111, 1966.

[9] S. Ergun, "Fluid flow through packed columns," *Chem. Eng. Prog.*, vol. 48, pp. 89–94, 1952.

[10] C. Y. Wen and Y. H. Yu, "A generalized method for predicting the minimum fluidization velocity," *AIChE Journal*, vol. 12, no. 3, pp. 610–612, 1966.

[11] J. R. Grace and H. Bi, "Introduction to circulating fluidized beds," in *Circulating fluidized beds*, Springer, 1997.

[12] M. Stieß, *Mechanische Verfahrenstechnik-Partikeltechnologie 1*. Springer Berlin Heidelberg, 2008.

[13] VDI Gesellschaft Verfahrenstechnik und Chemieingenieurwesen, *VDI-Wärmeatlas*. 2013.

[14] D. Geldart, "The effect of particle size and size distribution on the behaviour of gas-fluidised beds," *Powder Technology*, vol. 6, no. 4, pp. 201–215, 1972.

[15] D. Geldart, "Types of gas fluidization," *Powder Technology*, vol. 7, no. 5, pp. 285–292, 1973.

[16] H. T. Bi and J. R. Grace, "Flow regime diagrams for gas-solid fluidization and upward transport," *International Journal of Multiphase Flow*, vol. 21, no. 6, pp. 1229–1236, 1995.

[17] J. R. Grace, "Contacting modes and behaviour classi cation of gas solid and other two phase suspensions.," *Canadian Journal of Chemical Engineering*, vol. 64, no. June, pp. 353–363, 1986.

[18] J. D. Anderson Jr., J. Degroote, G. Degrez, E. Dick, R. Grundmann, and J. Vierendeels, *Computational Fluid Dynamics An Introduction*. Springer-Verlag Berlin Heidelberg, 3 ed., 2009.

[19] M. J. Andrews and P. J. O'Rourke, "The multiphase particle-in-cell (MP-PIC) method for dense particulate flows," *International Journal of Multiphase Flow*, vol. 22, no. 2, pp. 379–402, 1996.

[20] H. Kuhlmann, *Strömungsmechanik: eine kompakte Einführung für Physiker und Ingenieure*. Pearson Deutschland GmbH, 2014.

[21] D. M. Snider, S. M. Clark, and P. J. O'Rourke, "Eulerian-Lagrangian method for three-dimensional thermal reacting flow with application to coal gasifiers," *Chemical Engineering Science*, vol. 66, no. 6, pp. 1285–1295, 2011.

[22] M. A. van der Hoef, M. Ye, M. van Sint Annaland, A. T. Andrews, S. Sundaresan, and J. A. M. Kuipers, "Multiscale modeling of gas-fluidized beds," *Advances in chemical engineering*, vol. 31, pp. 65–149, 2006.

[23] S. Kraft, *Investigation of particle mixing in dual fluidized bed gasification systems by means of cold flow modelling and computational methods*. PhD thesis, Vienna University of Technology, 2017.

[24] M. Kodam, B. J. Freireich, M. T. Pretz, and B. A. Stears, "Performance prediction of riser termination devices using Barracuda Virtual Reactor ®," *Powder Technology*, vol. 316, pp. 190–197, 2017.

[25] D. M. Snider, "An Incompressible Three-Dimensional Multiphase Particle-in-Cell Model for Dense Particle Flows," *Journal of Computational Physics*, 2001.

[26] W. K. Ariyaratne, C. Ratnayake, and M. C. Melaaen, "Application of the MP-PIC method for predicting pneumatic conveying characteristics of dilute phase flows," *Powder Technology*, vol. 310, pp. 318–328, 2017.

[27] P. J. O'Rourke and D. M. Snider, "A new blended acceleration model for the particle contact forces induced by an interstitial fluid in dense particle/fluid flows," *Powder Technology*, vol. 256, pp. 39–51, 2014.

[28] S. E. Harris and D. G. Crighton, "Solitons, Solitary Waves, and Voidage Disturbances in Gas-Fluidized Beds," *Journal of Fluid Mechanics*, vol. 266, pp. 243–276, 1994.

[29] D. M. Snider, P. J. ORourke, and M. J. Andrews, "An incompressible two-dimensional multiphase particle-in-cell model for dense particle flows," tech. rep., Los Alamos National Lab., NM (United States), 1997.

[30] Y. Jiang, G. Qiu, and H. Wang, "Modelling and experimental investigation of the full-loop gas – solid fl ow in a circulating fl uidized bed with six cyclone separators," *Chemical Engineering Science*, vol. 109, pp. 85–97, 2014.

[31] F. Fotovat, A. Abbasi, R. J. Spiteri, H. de Lasa, and J. Chaouki, "A CPFD model for a bubbly biomass-sand fluidized bed," *Powder Technology*, vol. 275, pp. 39–50, 2015.

[32] Y. Liang, Y. Zhang, T. Li, and C. Lu, "A critical validation study on CPFD model in simulating gas-solid bubbling fluidized beds," *Powder Technology*, vol. 263, pp. 121–134, 2014.

[33] J. M. Weber, K. J. Layfield, D. T. Van Essendelft, and J. S. Mei, "Fluid bed characterization using electrical capacitance volume tomography (ECVT), compared to CPFD software's barracuda," *Powder Technology*, vol. 250, pp. 138–146, 2013.

[34] L. Zhang, Z. Wang, Q. Wang, H. Qin, and X. Xu, "Simulation of oil shale semi-coke particle cold transportation in a spouted bed using CPFD method," *Powder Technology*, vol. 301, pp. 360–368, 2016.

[35] C. B. Solnordal, V. Kenche, T. D. Hadley, Y. Feng, P. J. Witt, and K. S. Lim, "Simulation of an internally circulating fluidized bed using a multiphase particle-in-cell method," *Powder Technology*, vol. 274, pp. 123–134, 2015.

[36] X. Shi, R. Sun, X. Lan, F. Liu, Y. Zhang, and J. Gao, "CPFD simulation of solids residence time and back-mixing in CFB risers," *Powder Technology*, vol. 271, pp. 16–25, 2015.

[37] X. Shi, Y. Wu, X. Lan, F. Liu, and J. Gao, "Effects of the riser exit geometries on the hydrodynamics and solids back-mixing in CFB risers: 3D simulation using CPFD approach," *Powder Technology*, vol. 284, pp. 130–142, 2015.

[38] S. S. Rodrigues, A. Forret, F. Montjovet, M. Lance, and T. Gauthier, "CFD modeling of riser with Group B particles," *Powder Technology*, vol. 283, pp. 519–529, 2015.

[39] Q. Wang, T. Niemi, J. Peltola, S. Kallio, H. Yang, J. Lu, and L. Wei, "Particle size distribution in CPFD modeling of gas-solid flows in a CFB riser," *Particuology*, 2015.

[40] X. Shi, X. Lan, F. Liu, Y. Zhang, and J. Gao, "Effect of particle size distribution on hydrodynamics and solids back-mixing in CFB risers using CPFD simulation," *Powder Technology*, vol. 266, pp. 135–143, 2014.

[41] C. Chen, J. Werther, S. Heinrich, H. Y. Qi, and E. U. Hartge, "CPFD simulation of circulating fluidized bed risers," *Powder Technology*, vol. 235, pp. 238–247, 2013.

[42] S. Clark, D. M. Snider, and J. Spenik, "CO2 adsorption loop experiment with eulerian-lagrangian simulation," *Powder Technology*, vol. 242, pp. 100–107, 2013.

[43] Q. Wang, H. Yang, P. Wang, J. Lu, Q. Liu, H. Zhang, L. Wei, and M. Zhang, "Application of CPFD method in the simulation of a circulating fluidized bed with a loop seal, part I-Determination of modeling parameters," *Powder Technology*, vol. 253, pp. 814–821, 2014.

[44] M. A. Hamilton, K. J. Whitty, and J. S. Lighty, "Numerical Simulation Comparison of Two Reactor Configurations for Chemical Looping Combustion and Chemical Looping With Oxygen Uncoupling," *Journal of Energy Resources Technology*, vol. 138, no. 4, p. 042213, 2016.

[45] W. S. Amarasinghe, C. K. Jayarathna, B. S. Ahangama, and B. M. E. Moldestad, "Experimental Study and CFD Modelling of Minimum Fluidization Velocity for Geldart A , B and D Particles," vol. 7, no. 3, pp. 152–156, 2017.

[46] Y. Tsuji and Y. Morikawa, "LDV measurements of an air-solid two-phase flow in a horizontal pipe," *Journal of Fluid Mechanics*, vol. 120, pp. 385–409, 1982.

[47] M. Bobek, S. Rowan, J. Yang, J. Weber, F. Shafer, and R. W. Breault, "Analysis of a Vortexing Circulating Fluidized Bed for Process Intensification Via High-G Flows," *Journal of Energy Resources Technology*, vol. 140, no. 6, p. 62003, 2018.

[48] B. D. Adkins, N. Kapur, T. Dudley, S. Webb, and P. Blaser, "Experimental validation of CFD hydrodynamic models for catalytic fast pyrolysis," *Powder Technology*, vol. 316, pp. 725–739, 2017.

[49] F. Li, F. Song, S. Benyahia, W. Wang, and J. Li, "MP-PIC simulation of CFB riser with EMMS-based drag model," *Chemical Engineering Science*, vol. 82, pp. 104–113, 2012.

[50] Q. Ma, F. Lei, X. Xu, and Y. Xiao, "Three-dimensional full-loop simulation of a high-density CFB with standpipe aeration experiments," *Powder Technology*, vol. 320, pp. 574–585, 2017.

[51] S. Kraft, F. Kirnbauer, and H. Hofbauer, "Influence of drag laws on pressure and bed material recirculation rate in a cold flow model of an 8 MW dual fluidized bed system by means of CPFD," *Particuology*, vol. 36, pp. 70–81, 2017.

[52] D. Martinovic, *Kaltmodellversuche und MSR-Konzept einer Zweibett-Wirbelschicht-Vergasungsanlage.* Master's thesis, Technische Universität Wien, 2013.

[53] H. Liu, R. J. Cattolica, and R. Seiser, "Operating parameter effects on the solids circulation rate in the CFD simulation of a dual fluidized-bed gasification system," *Chemical Engineering Science*, vol. 169, pp. 235–245, 2017.